FEDERAL UNIVERSITY OF SANTA CATARINA (UFSC)

TECHNOLOGICAL CENTER (CTC)

GRADUATE PROGRAM IN MATERIALS SCIENCE AND ENGINEERING (PGMAT)

Marcelo Daniel Barros

Manufacturing and characterization of alumina/alumina-doped laminates: colloidal processing, dopants diffusion, and mechanical behavior

Florianópolis

2021

Marcelo Daniel Barros

Manufacturing and characterization of alumina/alumina-doped laminates: colloidal processing, dopants diffusion, and mechanical behavior

Thesis presented to the Graduate Program in Materials Science and Engineering (PGMAT) of the Federal University of Santa Catarina (UFSC), as a requirement for obtaining the PhD title in Materials Science and Engineering

Advisor: Prof. Dachamir Hotza, Dr. Ing-

Co-advisor: Rolf Janssen, Dr. Ing-

Florianópolis

2021

Ficha de identificação da obra elaborada pelo autor,
através do Programa de Geração Automática da Biblioteca Universitária da UFSC.

Barros, Marcelo Daniel
Manufacturing and characterization of alumina/alumina doped laminates: colloidal processing, dopants diffusion, and mechanical behavior / Marcelo Daniel Barros ; orientador, Dachamir Hotza, coorientador, Rolf Janssen, 2021.
114 p.

Tese (doutorado) - Universidade Federal de Santa Catarina, Centro Tecnológico, Programa de Pós-Graduação em Ciência e Engenharia de Materiais, Florianópolis, 2021.

Inclui referências.

1. Ciência e Engenharia de Materiais. 2. laminados cerâmicos. 3. alumina. 4. comportamento mecânico. 5. processamento coloidal. I. Hotza, Dachamir. II. Janssen, Rolf. III. Universidade Federal de Santa Catarina. Programa de Pós-Graduação em Ciência e Engenharia de Materiais. IV. Título.

Marcelo Daniel Barros

Manufacturing and characterization of alumina/alumina-doped laminates: colloidal processing, dopants diffusion, and mechanical behavior

This thesis was presented to obtain the title of PhD, evaluated and approved by the examination board composed of the following members:

Prof. Nahum Travitzky, Dr.

FAU/Germany

Prof. Pierre-Marie Geffroy, Dr.

UNILIM/France

Prof. Bruno Alexandre Pacheco de Castro Henriques, Dr.

UFSC

We certify that this is the original and final version of the conclusion work that was considered adequate to obtain the title of PhD in Materials Science and Engineering.

Documento assinado digitalmente
Joao Batista Rodrigues Neto
Data: 02/06/2021 18:46:45-0300
CPF: 645.810.989-04
Verifique as assinaturas em https://v.ufsc.br

Prof. João Batista Rodrigues Neto, Dr.

PGMAT/UFSC Coordinator

Documento assinado digitalmente
Dachamir Hotza
Data: 01/06/2021 10:51:42-0300
CPF: 495.235.039-87
Verifique as assinaturas em https://v.ufsc.br

Prof. Dachamir Hotza, Dr.

Advisor

Florianópolis, 2021.

ACKNOWLEDGEMENTS

First of all, I would like to thank God for health, guidance, and faith support during my life journey.

To my wife Letícia and my parents Carlos Roberto and Maria Lucir for all support that only the family can provide.

To my advisors Prof. Dr. Dachamir Hotza and Dr. Rolf Janssen for all the helpful talks, orientations, support, confidence, and opportunities.

To my friends and colleagues at Federal University of Santa Catarina (UFSC), Francesca, Rafael Vidal, Lisandro, Ruben, Douglas, Thaiane, Maria Ester, Vivian, Paula, Rafael Veit, Rafael Matos, Stephanie, Aldemir Luiz, Bernardo, Roberto, Daniela and Gilberto for friendship and partnership.

To my friends from Hamburg, Diego, Fran, Tim, Marcel, and Andreas for all the help, assistance, and friendship. For all Hamburg University of Technology (TUHH) staff that supported me during my stay abroad, especially Hans Jelitto, Kaline Furlan, Anja Borchert, and Manfred Geerken.

To my friends in general for the support and friendship all over these years.

To UFSC and TUHH for the infrastructure and opportunity to develop the research.

To CNPq and CAPES for the funding during this period.

“Judge your success by what you had to give up in order to get it.”

Dalai Lama XIV

ABSTRACT

In this work, alumina-based ceramic laminates were developed via aqueous tape casting, with subsequent lamination and sintering. Optimized colloidal processing through proper adjustment of parameters was achieved to reach particle stabilization, with the aid of a dispersant agent. The thermal analyses revealed the release of residual water and decomposition of short-chain organics at temperatures under 215 °C, long-chain additives over 300 °C, with complete burn out of organics after 525 °C. The addition of 4 wt% of TiO_2+MnO reduced the initial sintering temperature and increased the sinterability of alumina (Al_2O_3). Sintered samples presented α-alumina, rutile, and $MnTiO_3$ as crystalline phases. High concentrations of Mn and Ti were observed at triple points and grain boundaries, as well as within alumina grains. Compared to pure alumina, doped alumina (d-Al_2O_3) presented higher average grain size, hardness, and Young's modulus, which increased with increasing sintering temperature. A diffused zone with dopants was observed through the pure alumina layers, right after the interface with the doped alumina ones. This zone presented a gradual decrease in properties' values, corresponding to a decreasing gradient in the dopants concentration in the Al_2O_3 layer with increasing distance from the interface. The mechanical strength of d-Al_2O_3 samples sintered at 1200 °C was not statistically different from Al_2O_3 samples sintered at 1350 °C. Regarding doped-pure alumina laminates, the strength of laminates with thin weak interlayers (4:1 ratio) did not change compared to references. Nevertheless, as the thickness of these weak interlayers increased (1:1 ratio or higher), a loss of strength was observed. Monolithic references showed constant values of fracture toughness (K_{IC}), ~2 $MPa \cdot m^{1/2}$, and linear crack path. On the other hand, the K_{IC} of laminates was higher when the crack propagates from weak layers to dense layers. This behavior was more evident as the weak layers' thickness increased. Regarding Al_2O_3 laminates with porous interlayers, fracture surfaces presented small deviations when the crack propagates through porous interlayers. However, no significant differences were observed in the strength, work of fracture, and fracture toughness.

Keywords: colloidal processing, alumina laminates, laminate design, mechanical strength, R-curve.

RESUMO

Neste trabalho, laminados cerâmicos à base de alumina foram desenvolvidos por colagem de fitas, seguida de laminação e sinterização. A otimização do processamento coloidal pelo ajuste adequado dos parâmetros atingiu a estabilização das partículas, com auxílio de um agente dispersante. Análises térmicas revelaram a remoção de água residual e aditivos orgânicos de cadeia curta em temperaturas abaixo de 215 °C, de aditivos de cadeia longa acima de 300 °C, e de orgânicos residuais ao se atingir 525 °C. A adição de 4 m% de TiO_2+MnO reduziu a temperatura inicial de sinterização e aumentou a sinterabilidade da alumina. Os sinterizados apresentaram as fases cristalinas alumina alfa, rutilo e $MnTiO_3$. Altas concentrações de Mn e Ti foram observados nos pontos triplos e nos contornos de grão, bem como dentro dos grãos de alumina. A alumina dopada apresentou valores maiores de densidade, tamanho de grão, dureza e módulo de elasticidade comparados à alumina pura, os quais aumentaram com o aumento da temperatura de sinterização. Uma zona de difusão de dopantes foi observada nas camadas de alumina pura, logo após a interface com as camadas alumina dopada. Essa zona apresentou uma diminuição gradual nos valores das propriedades, refletindo em um gradiente decrescente da quantidade de dopantes à medida que se afasta da interface. A resistência mecânica da alumina pura e dopada, sinterizadas à 1350 e 1200 °C respectivamente, foi estatisticamente equivalente. A respeito dos laminados, a resistência dos que possuem finas camadas porosas (razão 4:1) não foi diferente das referências. No entanto, à medida que a espessura dessas camadas aumentou (razão 1:1 e 1:2), uma diminuição na resistência foi observada. As referências apresentaram valores constantes de tenacidade à fratura (K_{IC}), ~2 $MPa \cdot m^{1/2}$, e propagação de trinca linear. Por outro lado, K_{IC} dos laminados aumenta quando a trinca se propaga da camada porosa para a densa. Esse comportamento foi mais evidente com o aumento da espessura das camadas fracas. A superfície de fratura dos laminados com interfaces porosas apresentou pequenos desvios com a propagação da trinca através das intercamadas. Entretanto, não foram observadas diferenças significativas na resistência mecânica, no trabalho e na tenacidade à fratura.

Palavras-chave: processamento coloidal, laminados de alumina, projeto de laminados, resistência mecânica, curva R.

RESUMO EXPANDIDO

PRODUÇÃO E CARACTERIZAÇÃO DE LAMINADOS ALUMINA/ALUMINA DOPADA: PROCESSAMENTO COLOIDAL, DIFUSÃO DE DOPANTES, E COMPORTAMENTO MECÂNICO

Introdução

Materiais alternativos aos metais, como as cerâmicas, começaram a ser utilizados para aumentar a temperatura de serviço em aplicações de engenharia. Entretanto, cerâmicas monolíticas são frágeis e apresentam fratura catastrófica, limitando as suas aplicações como materiais estruturais de engenharia. Cerâmicas são altamente influenciadas pelas suas ligações iônicas e covalentes, em que mecanismos de cisalhamento dos planos cristalinos são escassos e a falha ocorre com baixíssima ou nenhuma deformação plástica. Como a presença de defeitos é praticamente inevitável, diferentes tipos de materiais vêm sendo estudados e desenvolvidos nos últimos anos.

Compósitos de matriz cerâmica se tornaram uma solução para o problema citado com alta aplicabilidade. Esses materiais apresentam uma matriz cerâmica reforçada por partículas, camadas, e pequenas ou longas fibras, podendo apresentar excelente resistência mecânica, tenacidade à fratura, estabilidade termodinâmica e resistência a atmosferas oxidantes. Essas são propriedades importantes para aplicações termoestruturais como aeropropulsão, veículos e estruturas espaciais, além de indústria nuclear e química. Os laminados cerâmicos começaram a ser estudados e produzidos de forma que interfaces ou camadas fossem utilizadas para frear o crescimento de trinca e/ou criar uma resistência limite a qual deveria ser excedida para haver tal crescimento. Alguns exemplos desses materiais são os com camadas densas-rígidas e interfaces fracas; os com camadas fracas devido à presença de porosidade, microtrincas e heterogeneidade; e os com tensões residuais internas.

Muitos desses materiais multicamadas em que se observa um aumento da resistência à fratura possuem um comportamento de curva R, em que a tenacidade à fratura aumenta com o aumento do comprimento de trinca. Esse efeito contribui para o aumento da energia gasta para romper o material (trabalho de fratura). Embora a literatura tenha apresentado diferentes tipos de laminados cerâmicos para aplicação estrutural nos últimos anos, existe ainda uma gama de combinações e possibilidades não exploradas,

além da necessidade de estudos mais aprofundados acerca do processamento, da microestrutura e do comportamento mecânicos destes materiais.

Objetivos

O objetivo deste trabalho é desenvolver por rota coloidal e subsequente sinterização, laminados cerâmicos de alumina e alumina dopada com TiO_2 e MnO com controle de propagação de trinca utilizando intercamadas fracas, caracterizando a microestrutura e comportamento mecânico dos mesmos. Dentro desse escopo, estão a otimização de suspensões cerâmicas para processamento via colagem de fitas, a definição da configuração, laminação e sinterização dos laminados, a investigação da difusão dos dopantes através da interface e a análise do desempenho mecânico e propagação de trinca.

Metodologia

A alumina fina foi dopada com TiO_2 e MnO, moída, misturada e homogeneizada com auxílio de um moinho de alta energia e etanol como meio líquido. Feito isso, a mistura foi deixada para secar em temperatura ambiente e posteriormente peneirada. A morfologia dos pós de alumina fina (A), alumina fina dopada (D) e alumina grosseira (C) foi analisada por microscopia eletrônica de varredura (MEV). A técnica de espalhamento dinâmico de luz foi utilizada para análise do tamanho de partícula e potencial zeta dos pós, sendo que para o último foi realizada autotitulação com soluções de NaOH e HCl para que o pH variasse entre 2 e 12. Em seguida foram produzidas suspensões aquosas cerâmicas com aditivos orgânicos para processamento via colagem de fitas. O comportamento reológico das mesmas foi analisado por viscosímetro com controle da taxa de cisalhamento. As fitas cerâmicas foram processadas sobre um filme coletor em um *tape caster*, e deixadas para secar a temperatura ambiente por 24 h. Ambas as superfícies das fitas foram analisadas por MEV. Para análise das propriedades térmicas, os *tapes* foram submetidos à calorimetria diferencial de varredura/termogravimetria e dilatometria. Espectroscopia de energia dispersiva (EDS) foi realizada juntamente com a MEV. As fases cristalinas dos pós a verde e sinterizados foram identificadas por difração de raios-X.

Processaram-se os laminados cerâmicos com uma camada intermediária de alumina dopada entre camadas de alumina para estudo da difusão dos dopantes através da interface. Os laminados foram termoprensados e posteriormente sinterizados a 1100, 1150, 1200, 1250 °C. A microestrutura foi analisada por MEV, e o método do intercepto

linear usado para medir o tamanho médio de grão. A dureza e o módulo de elasticidade das camadas e da região interfacial de difusão foram medidos usando um nanoindentador com ponta do tipo Berkovich, através do método de medição contínua da rigidez. Além disso, uma análise aprofundada da difusão dos dopantes através da interface foi realizada por nanoindentação e medição do tamanho de grão no laminado sinterizado à 1200 °C.

Quatro tipos de laminados sinterizados foram produzidos. Os três primeiros são compostos por camadas densas de alumina dopada alternadas por camadas fracas de alumina (DA), sinterizados à 1200 °C e com diferentes razões de espessura (camada densa/fraca), 4:1, 1:1 e 1:2. O quarto é um laminado de camadas de alumina com menor tamanho de partícula alternadas com camadas menos espessas de alumina com maior tamanho de partícula (AC), com razão de espessura 4:1, sinterizado à 1350 °C. Como forma de auxiliar na investigação das características e propriedades dos laminados, referências monolíticas de alumina e alumina dopada sinterizadas à 1350 e 1200°C, respectivamente, foram produzidas. A densidade foi medida pelo método de Arquimedes em balança analítica. Dureza e módulo de elasticidade foram medidos por nanoindentação. A microscopia eletrônica de varredura foi usada para investigar a superfície de fratura e a microestrutura, revelada com ataque térmico. O tamanho médio de grão foi medido pelo método do intercepto linear. Testes de flexão em 4 pontos foram realizados para medição da resistência mecânica. A tenacidade à fratura (K_{IC}) e consequente curva R foram medidas pela quebra por flexão de barras entalhada em V (SEVNB) em um equipamento com controle rígido do deslocamento que permite com que a trinca cresça estavelmente através de ciclos de carregamento e descarregamento. Através desses ensaios, também foi possível avaliar o trabalho de fratura. As tensões residuais nas camadas dos laminados foram calculadas por equações específicas em que usa o coeficiente de expansão térmica, o módulo de elasticidade, o coeficiente de Poisson, e a espessura e número de camadas.

Por fim, foram processadas camadas de alumina com 15, 30 e 45 vol% de porosidade monodispersa criada por esferas de poliestireno (PS - agente porogênico) através de colagem direta coloidal e posterior sinterização a 1350°C. A microestrutura, o tamanho médio de grão e tamanho médio de poros foram analisados por MEV. Em seguida, laminados cerâmicos de alumina foram processados com camadas densas e espessas alternadas por finas camadas com 45 vol% de porosidade (A-PS). Por MEV foi analisada a microestrutura e a superfície de fratura, a nanoindentação para medir a dureza e o módulo de elasticidade, e o método de Arquimedes para medir a densidade.

Indentações com ponteira Vickers foram feitas nas camadas densas próximo às camadas porosas para verificar o comportamento da propagação da trinca. A resistência mecânica e a tenacidade à fratura foram medidas, respectivamente, por flexão 4 pontos e SEVNB.

Resultados e discussão

As partículas dos pós, em geral, apresentaram formas irregulares facetadas e distribuição unimodal. O tamanho médio de partícula medido foi de 278 ± 144, 264 ± 160 e 439 ± 190 nm para de A, D e C, respectivamente. As fases cristalinas identificadas foram α-alumina para Al_2O_3, rutilo para TiO_2 e MnO cúbico. A presença do dispersante nas suspensões diminuiu efetivamente o ponto isoelétrico (IEP). A presença dos dopantes MnO e TiO_2 reduziu o IEP da alumina de 6,8 para 5,6. As suspensões cerâmicas para processamento por colagem de fitas apresentaram pH na região estável (módulo do potencial zeta maior que 40 mV) e comportamento reológico pseudoplástico, o que garantiu a eficiência do processamento de fitas cerâmicas sem defeitos visíveis, flexíveis e manuseáveis após a secagem. A espessura final dos tapes a verde variou de 100 a 145 μm, com diferença na morfologia das superfícies em contato com ar (mais porosa) e com o filme coletor (menos porosa). Através das análises térmicas observou-se que a remoção da água residual e dos orgânicos na fita cerâmica a verde ocorre entre 215 e 530°C. Os ensaios dilatométricos mostraram a eficiência dos dopantes em reduzir a temperatura inicial de sinterização e aumentar a taxa de sinterização da alumina, além de evidenciar menor retração devido a tamanhos de partículas maiores (menor área de superfície). Após a sinterização, foram identificadas as fases cristalinas α-alumina para Al_2O_3, e a presença de rutilo e titanato de manganês ($MnTiO_3$) no pó dopado. O EDS mostrou que os dopantes podem se localizar nos pontos triplos, contornos de grão e dentro dos grãos de alumina.

A difusão dos dopantes forma uma região amarronzada, visível oticamente, na camada de alumina logo após a interface, que tem sua espessura aumentada com o aumento da temperatura de sinterização. A alumina dopada apresenta, independente da temperatura de sinterização, tamanho médio de grão maior que a alumina pura. Com isso, a microestrutura da região de difusão também se modificou devido à presença dos dopantes, com grãos maiores que D e menores que A. Ensaios de nanoindentação revelaram valores maiores de dureza (H) e módulo de elasticidade (E) para a alumina dopada. Os valores de H e E na região com a presença de dopantes são intermediários às duas aluminas distintas. Esses valores, em geral, aumentam com a temperatura de sinterização. Uma análise mais detalhada de zona de difusão do laminado sinterizado a

1200°C mostrou que H, E e o tamanho médio de grão decrescem gradativamente à medida que a presença de dopantes diminui na camada de alumina (sentido alumina dopada → alumina).

O uso de dopantes aumentou a densidade da alumina, influenciando diretamente no aumento dos valores de H e E obtidos por nanoindentação. Ensaios de resistência mecânica e tenacidade à fratura evidenciaram a eficiência do uso dos dopantes para reduzir a temperatura de sinterização da alumina sem perdas consideráveis nos valores destas propriedades. Para os laminados DA, quanto maior o volume de alumina, menor é a densidade. A presença de uma camada fina, razão 4:1, não deteriorou a resistência mecânica do laminado DA e AC. Entretanto, os laminados DA com razão 1:1 e 1:2 apresentaram uma redução de 16% e 13% respectivamente em relação à referência. Em geral, uma diminuição no módulo de Weibull está associado ao aumento do volume total de camada porosa nos laminados. A tenacidade à fratura das referências monolíticas apresentou-se quase constante à medida que o tamanho de trinca aumenta, em torno de 2,0 $MPa \cdot m^{1/2}$. Todavia, os laminados DA e AC apresentaram curva R em que K_{IC} aumenta na região de interface até atingir um valor máximo, e depois diminui à medida que a trinca continua a se propagar na camada densa. Esse comportamento se repete toda vez que a trinca se aproxima da interface entre as camadas densas e fracas. Quanto maior a espessura da camada fraca, mais pronunciado é este efeito na K_{IC}, e menor o trabalho de fratura. Contudo, os valores de tenacidade à fratura observados para os compósitos não são significativamente diferentes das referências, variando entre 1,3 e 2,2 $MPa \cdot m^{1/2}$. As superfícies de fratura dos laminados DA e AC se mostraram planas, e não revelaram modificações visíveis no caminho percorrido pela trinca, apresentando uma propagação quase linear.

A espessura dos filmes de alumina porosa produzidos por colagem direta variou entre 2 e 15 μm, com distribuição aleatória de poros modelados. Grãos maiores e menores foram observados, sendo os últimos majoritariamente observados próximos aos poros. O aumento no volume de poros tende a diminuir o tamanho médio dos grãos devido à limitação ao movimento dos contornos de grão, reduzindo o número de grãos vizinhos. Valores menores de diâmetro de poro foram medidos para poros na superfície, comparado aos poros internos, devido ao fato que as esferas de PS se encontram ~3/4 submergidas até a secagem. Laminados foram produzidos com intercamadas porosas com 45 vol%, em que a adição de 10 m% de ligante (referente à quantidade de sólidos) foi necessária para garantir boa adesão entre as camadas. A densidade relativa final do laminado A-PS foi de

90%. A dureza e o módulo de elasticidade das camadas porosas são, aproximadamente, 30% dos valores obtidos para as camadas densas. Indentações Vickers próximas às camadas porosas indicaram que a presença da porosidade pode frear o crescimento da trinca. Os valores de resistência mecânica foram estatisticamente iguais para A-PS comparados a referência monolítica. Entretanto, a distribuição de Weibull indicou um valor menor do módulo, que pode ser atribuído a presença das intercamadas porosas. A tenacidade à fratura apresentou discretas variações na curva de força-deslocamento e na curva R decorrentes da passagem da trinca pelas camadas porosas. O trabalho de fratura não foi significativamente diferente do observado para a referência. Embora macrodesvios não tenham sido observados nas micrografias da fratura, uma certa rugosidade e variação de planaridade da superfície ocorreu nas regiões das intercamadas. Essas regiões, quando analisadas mais próximas, apresentaram pequenos desvios e ramificações da trinca.

Considerações finais

Os resultados obtidos mostraram que foi possível produzir suspensões cerâmicas estáveis para processamento de fitas cerâmicas sem defeitos e flexíveis. Além disso, comprovou-se a eficiência dos dopantes em reduzir a temperatura inicial de sinterização e aumentar a taxa de sinterização da alumina. A difusão de dopantes na camada de alumina através da interface ocorre gradativamente, e aumenta com o aumento da temperatura de sinterização. O tamanho de grão, a dureza e o módulo de elasticidade da região de difusão apresentam valores intermediários às camadas de alumina e alumina dopada. Laminados com razão de espessura 1:1 ou menor apresentam redução de resistência mecânica. A tenacidade à fratura dos laminados apresenta variações de aumento e diminuição à medida que trinca se propaga, sendo estas mais evidentes com o aumento da espessura das camadas fracas. A resistência mecânica dos laminados A-PS apresentou um pequeno aumento. Já a tenacidade à fratura apresentou pequenas variações devido à propagação da trinca nas intercamadas. Pequenos desvios de trinca foram observados nas interfaces porosas.

Palavras-chave: processamento coloidal, laminados de alumina, projeto de laminados, resistência mecânica, curva R.

LIST OF FIGURES

LIST OF TABLES

LIST OF ABBREVIATIONS

4PB	Four-point bending
A1200	Pure fine alumina reference sample sintered at 1200 °C
A1350	Pure fine alumina reference sample sintered at 1350 °C
AGS	Average grain size
AC-17L	Laminate sintered at 1350 °C with 17 layers: 9 of A1350 and 8 of C1350, with the layer thickness ratio of 4:1, respectively
A-PS	Laminate sintered at 1350 °C with 17 layers: 9 of A1350 and 8 of pure porous alumina layer, with porosity created by polystyrene spheres
C1350	Pure coarse alumina reference sample sintered at 1350 °C
CMC	Ceramic matrix composite
CSM	Continuous stiffness measurement
CTE	Coefficient of thermal expansion
D1200	Doped fine alumina reference sample sintered at 1200 °C
DA-17L	Laminate sintered at 1200 °C with 17 layers: 9 of D1200 and 8 of A1200, with the layer thickness ratio of 4:1, respectively
DA-11L	Laminate sintered at 1200 °C with 11 layers: 6 of D1200 and 5 of A1200, with the layer thickness ratio of 1:1, respectively
DA-3L	Laminate sintered at 1200 °C with 3 layers: 2 of D1200 and 1 of A1200, with the layer thickness ratio of 1:2, respectively
DLS	Dynamic light scattering
DSC	Differential scanning calorimetry
EDS	Energy-dispersive X-ray analysis
IEP	Isoelectric point
LIM	Line-intercept method
MCC	Multilayer ceramic composite
OM	Optical microscopy

PS	Polystyrene
PSD	Particle size distribution
RD	Relative density
SEM	Scanning electron microscopy
SEVNB	Single edge V notched beam
STEM	Scanning transmission electron microscopy
TGA	Thermogravimetric analysis
XRD	X-ray diffraction analysis
ZP	Zeta potential

LIST OF SYMBOLS

ζ	Zeta potential
E	Young's modulus
H	Hardness
K_I	Stress intensity factor
K_{IC}	Fracture toughness
$K_{IC\ max}$	Maximum fracture toughness
$K_{IC\ min}$	Minimum fracture toughness
t_c	Thickness of compressive layer
t_t	Thickness of tensile layer
d_{10}	The portion of particles with diameters smaller than this value is 10%
d_{50}	The portions of particles with diameters smaller and larger than this value are 50%. Also known as the median diameter
d_{90}	The portion of particles with diameters below this value is 90%.
σ_f	Average maximum strength
σ_0	Mean characteristic strength
m	Weibull modulus
W_F	Work of fracture

TABLE OF CONTENTS

Chapter 1 – Introduction and objectives

1.1 Introduction

Metallic materials reached the upper limit of their use temperature. Therefore, alternative materials, as ceramics, are necessary to increase this service temperature. However, monolithic ceramics are brittle and present catastrophic failure, limiting their application as structural engineering materials. These materials are highly influenced by their strong ionic and covalent bondings. Shear mechanisms of crystalline planes are scarce and failure occurs with very low or without plastic deformation. As the presence of defects is practically inevitable, different kinds of materials have been studied and developed in the last years[1, 2].

Ceramic matrix composites (CMC) present a ceramic matrix reinforced by particles, whiskers, fibers, or laminates. These materials became an alternative to overcome the reported problems, demonstrating a high application potential. They can present excellent mechanical strength and high fracture toughness, interesting properties for thermostructural applications. Characteristics such as the thermodynamic stability and oxidizing atmospheres resistance enable their use for aero propulsion, aerospace vehicles and structures, and nuclear and chemical industries[3, 4].

Laminated ceramics became to be processed in the 1960s as a need to be support for microelectronic elements. As a consequence of this demand, different methods to obtain materials with controlled thickness have been studied, such as tape casting, dip coating, sequential slip casting, centrifugation, electrophoretic deposition, and other colloidal processing techniques[5, 6]. To optimize properties, laminates started to be produced in such a way that interfaces or layers were used to oppose the beginning of crack growth and/or develop a limit resistance that should be exceeded to have such growth. Some examples are the dense and rigid layer composites with weak interfaces, weak layer composites due to the presence of porosity, oriented microcracks, and heterogeneous layers. Another way of producing high-strength laminates is incorporating residual stresses, based on the different coefficients of thermal expansion (CTE or α) of the materials and their shrinkage after sintering. Also, the laminated composites can promote a synergistic effect between the materials of the layers that have different characteristics.

1.2 Research objectives

This work aims to develop, by colloidal processing and subsequent sintering, alumina-based laminates with control of crack propagation using weak interlayers and to characterize their microstructure and mechanical behavior.

The specific objectives are:

- Produce pure and doped alumina tapes via tape casting, characterizing powders, slurries and tapes (green and sintered);
- To design, laminate, and sinter defect-free laminates: to introduce differences in the elastic mismatch between dense and porous layers created by the use of dopants, different particle sizes, and polystyrene spheres to enhance the fracture behavior. The thickness of porous layers was also variated.
- To investigate the diffusion of dopants at the doped-pure alumina interface;
- Characterize the microstructure, the mechanical performance, and the crack propagation, and correlated them with the laminate designs.

1.3 Thesis structure

This thesis is structured in seven chapters. Chapters 1 and 2 comprise, respectively, the introduction and a literature review of relevant topics related to this work. Research chapters are presented from Chapter 3 to Chapter 6. Each one is divided into sections: introduction, materials and methods, results and discussion, and conclusions. References are merged at the end of the document.

Chapter 3 presents the characterization of ceramic powders, slurries, and green and sintered tapes. Chapter 4 introduces the production of the first sintered laminates composed of pure and doped alumina layers, making use of nanoindentation and visual analyses to evaluate the diffusion of dopants through the pure-doped alumina interface. In Chapter 5, laminates are designed based on the particle size powders, the composition of tapes, and thickness of layers and after characterized according to their microstructure, mechanical, and fracture behavior. Chapter 6 is an extension of the last chapter, in which laminates were produced with thin weak interlayers with porosity created due to the presence of incorporated polystyrene spheres. Finally, in Chapter 7 the general conclusions and an outlook for future works are presented.

Chapter 2 – Literature review

2.1. Aluminum oxide

Aluminum oxide or alumina (Al_2O_3) is a widely used ceramic due to its mix of properties and appreciable cost-benefit compared to other ceramics. It is one of the most used oxide ceramics for structural applications due to its properties such as high strength, wear resistance, hardness, melting point, and chemical stability. It is also suitable for thermal and electrical insulation. Alumina has, for the most part, ionic bonding (Al–O, 56.7% ionic character). The most thermodynamically stable phase of Al_2O_3 is the alpha-alumina (α-Al_2O_3), or corundum, with rhombohedral structure due to a hexagonal arrangement of ions O^{2-} and Al^{3+} cations (Figure 1), where the latter are symmetrically located in 2/3 of octahedral interstitial positions[7, 8]. Table 1 summarizes some of the main properties of α-alumina.

Figure 1 – Crystal structure of α-alumina.

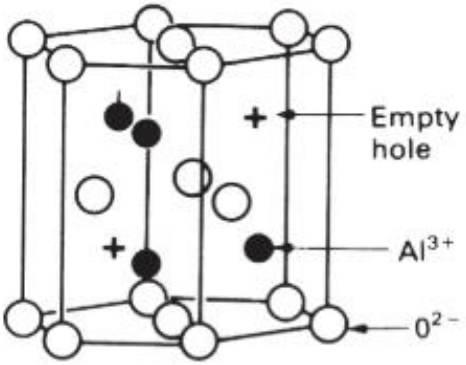

Ref: Ashby & Jones (2011)[9].

Table 1 – Physical, thermal, and mechanical properties of sintered α-alumina.

Properties	Value	Reference
Melting point	2040 °C	Black & Hastings (1998)[10]
Density	3.98 $g \cdot cm^{-3}$	Black & Hastings (1998)[10]
Vickers hardness	18-20 GPa	Acchar & Segadães (2009)[11]
Young's modulus	380 GPa	Lehman (1991)[12]
Poisson ratio	0.27–0.30	Riedel & Chen (2011)[7]
Thermal conductivity	40 $W \cdot m^{-1} \cdot K^{-1}$ at 25 °C 10 $W \cdot m^{-1} \cdot K^{-1}$ at 1000 °C:	Riedel & Chen (2011)[7]
Thermal expansion coefficient	$8.8.10^{-6}$ K^{-1} (=c)* $7.9.10^{-6}$ K^{-1} (+c)*	Riedel & Chen (2011)[7]
Bending strength	250–600 MPa	Riedel & Chen (2011)[7]
Compression strength	3790 MPa	Black & Hastings (1998)[10]
Fracture toughness	2–4 $MPa \cdot m^{½}$	Acchar & Segadães (2009)[11]

* = parallel; + perpendicular to the c axis.

Alumina presents high sintering temperatures, which usually increase with increasing purity, reaching temperatures over 1700 °C in some cases to achieve fully dense materials. High purity alumina produced by chemical methods allowed obtaining dense bodies at 1500 °C[13]. The particle size also plays an important role in sintering temperatures. Sintering driving force is inversely proportional to the particle size, due to the smaller diffusion distances[14, 15]. Rao and co-authors obtained alumina samples sintered at 1300 °C with 98% relative density (RD) due to the high sinter reactivity of the powder (high surface area, particle size 0.22 μm)[16]. Yeh and Sacks obtained >99.5% RD for samples sintered at 1150 °C using ~0.1 μm alumina[17].

2.1.1 Doping of alumina

During sintering, diffusion occurs due to the atomic defects moving through the structure, and grain growth and densification run at the same time as intergranular pores are removed through grain-boundary diffusion[18, 19]. In bulk alumina, the coefficients of diffusion of aluminum and oxygen are equivalent[20]. Additives – such as TiO_2, MnO, MgO, Cu_2O, ZrO_2, Y_2O_3, and Li_2O_3 – have been employed to increase alumina sinterability and achieve full density while controlling grain growth[21, 22]. Sintering aids can enhance sintering due to the formation of lattice defects, solid solutions, or liquid phases. Generally, there is an optimal amount of additives, which varies with the sintering temperature, to achieve higher densification[23, 24]. Table 2 compiles some works that used oxide ceramics as sintering additives for alumina.

Table 2 – Selected works using oxide ceramics as sintering additives to enhance alumina sinterability.

Author, year	Sintering additive	Amount	Sintering temperature/time	RD (%)
Winkler *et al.* (1945)[25]	TiO_2	≤ 1 mol%	1300 °C/2 h	
Cutler *et al.* (1957)[26]	Cu_2O, MnO, TiO_2,	≤ 4 wt.%	1300 °C/1 h	92-96
Jones *et al.* (1958)[27]	Cr_2O_3, FeO, MnO, TiO_2	1 - 8 mol%	1200-1500 °C	
Keski & Cutler (1968)[28]	MnO	0.1-1%	1450-1650 °C	
Bagley *et al.* (1970)[29]	TiO_2	≤ 0.4 at.%	1520-1582 °C	
Bennison & Harmer (1983)[30]	MgO	250 ppm	1600 °C	
Kostić *et al.* (1990)[31]	MnO, TiO_2	5 wt. %	1300 °C/2 h	95
Xue & Chen (1991)[24]	B_2O_3, CuO, MgO, TiO_2	2 mol%	1070 °C/1 h	99.3
Toy *et al.* (1995)[32]	MnO_2	≤ 0.5	1550-1650 °C/1 h	98-99.2
Erkalfa *et al.* (1998)[33]	MnO_2,TiO_2	≤ 6 wt.%	1250 °C/1 h	98.2
Sathiyakumar & Gnanam (2002)[34]	B_2O_3, CuO, MgO, TiO_2	2 mol%	1200-1250 °C/3 h	99.2-99.6

2.1.2 Diffusion mechanisms in alumina

The direct exchange of diffusing neighboring atoms and rotation mechanism involving three or four atoms are not probable to occur in ceramics. The reason for this is the characteristic covalent or ionic bonding of ceramics. Thus, relatively high energy is required to break such bonds. For diffusion to occur in ceramics, the mechanism of diffusion must follow point defects exchange with atoms. These defects, such as vacancies (empty lattice sites) and interstitials (extra atoms at non-lattice sites), are involved in atomic diffusion mechanisms due to the disturbing in lattice periodicity[35, 36]. Lattice or volume diffusion occurs by interstitial or substitutional mechanisms. Ceramics are typical examples of point defects with mixed configurations (Figure 2). Besides, diffusion at grain boundaries can also take place. When there are two distinct materials separated by an interface and a difference in the diffusion coefficients exists, there will be mass flowing through the interface, the so-called interdiffusion (Figure 2). Atoms tend to migrate out of the high concentrations during the process. See the classical example presented by Kirkendall[37].

Figure 2 – On the left side, an illustration of point defects in ceramics (vacancy and interstitial). On the right side, the schematic illustration of the classical work on interdiffusion performed by Kirkendall[37] of a concentration profile of Cu-Ni, (a) before diffusion and (b) the intermixing of the components after diffusion.

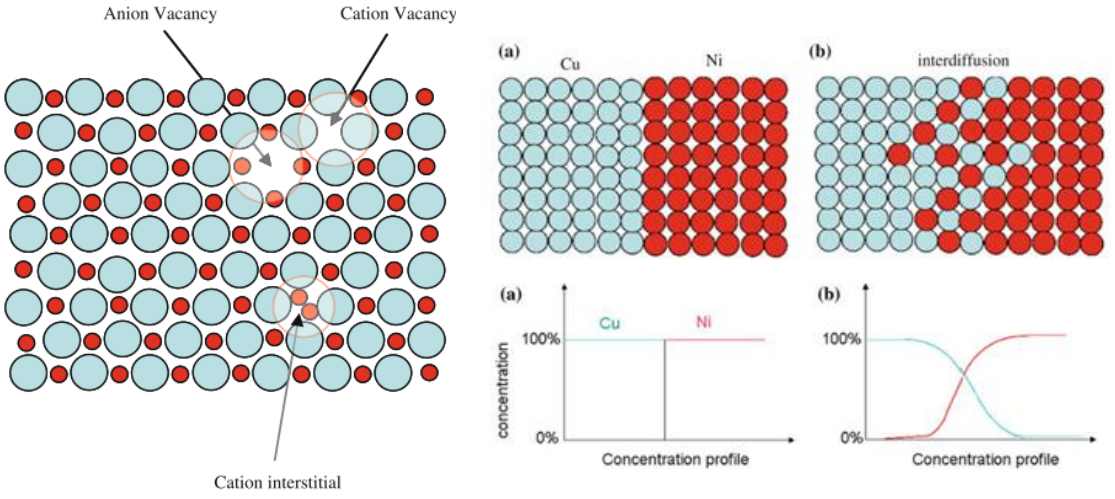

Ref: Pelleg (2016)[35].

The lattice diffusion of Al or O in polycrystalline Al_2O_3 is very small, and fast diffusion will occur along the grain boundaries, at a higher rate than in lattices. The diffusivity of aluminum is considerably higher than the oxygen diffusivity. Besides, Al diffusivity is enhanced when α-Al_2O_3 is doped with Ti due to an increase in the concentration of mobile Al vacancies which enable the transport of aluminum by a

vacancy mechanism[38–40]. The diffusion coefficient increases with the increase of temperature, which reflects directly in the distance of diffusion through the material, as observed in Figure 3 in the work of Paladino and Kingery[39].

Figure 3 – The concentration profile of Al_2O_3 sintered at 1800 (on the left side) and 1905°C (on the right side). C_o is the initial concentration, and C is the concentration at any time.

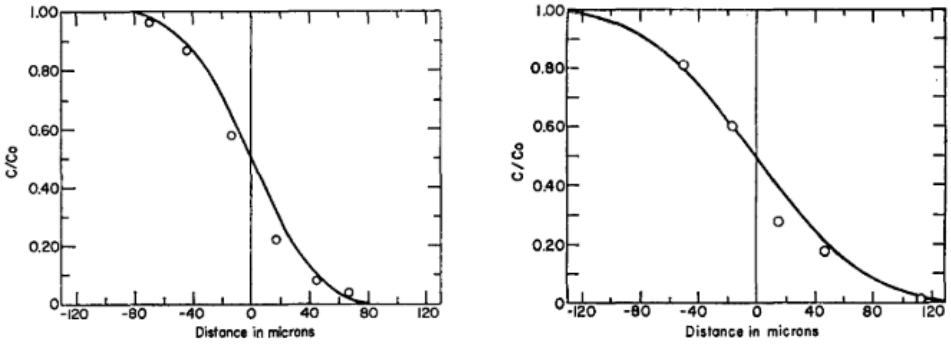

Ref: Paladino and Kingery (1962)[39].

2.2 Tape casting

Tape casting is a processing technique that allows the production of flat, thin (1 to 1000 µm) and high surface area ceramics. It is considered to be an economic process, used to produce substrates and components like capacitors, piezoelectric actuators, sensors, and solid oxide fuel cells (SOFC)[41, 42]. Besides, it is also used to produce laminated ceramics for structural applications that demand high mechanical performance[43, 44]. The first stage of the process is the production of the ceramic slurry, where powder, solvent, and dispersant are put together and milled by shear forces to deagglomerate particles and uniformly distribute the components. Afterward, plasticizers and binders are added and mixed to give the green tape resistance and flexibility. Then, the slurry is sieved to remove any coarse contamination or agglomerated particles. Before casting, the ceramic slurry is normally submitted to a de-airing step, in which vacuum, centrifugation, ultrasonic bath, or simply repose can be used[45, 46].

The slurry characteristics influence the particle arrangement in the green body, consequently affecting the sintering and final properties of sintered components. The order of addition of components is very important to obtain a homogeneous slurry. The dispersant needs to be added first to avoid surface particle competition. The casting of the ready slurry is performed with the help of a tape caster (Figure 4). The suspension is poured inside the tank and dragged by the collector film movement. The control of thickness is done by a leveling device (doctor blade), forming the wet tape. Finally, the

solvent is dried in the drying chamber and the green tape is formed[45, 47]. The tape casting process can be summarized in the scheme of Figure 5.

Figure 4 – Schematic diagram of a tape casting machine.

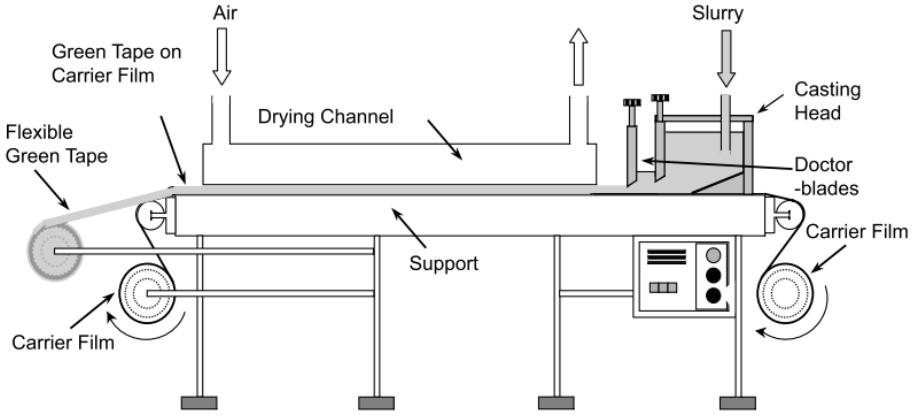

Ref: Riedel & Chen (2011)[46].

Figure 5 – General processing scheme of tape cast products.

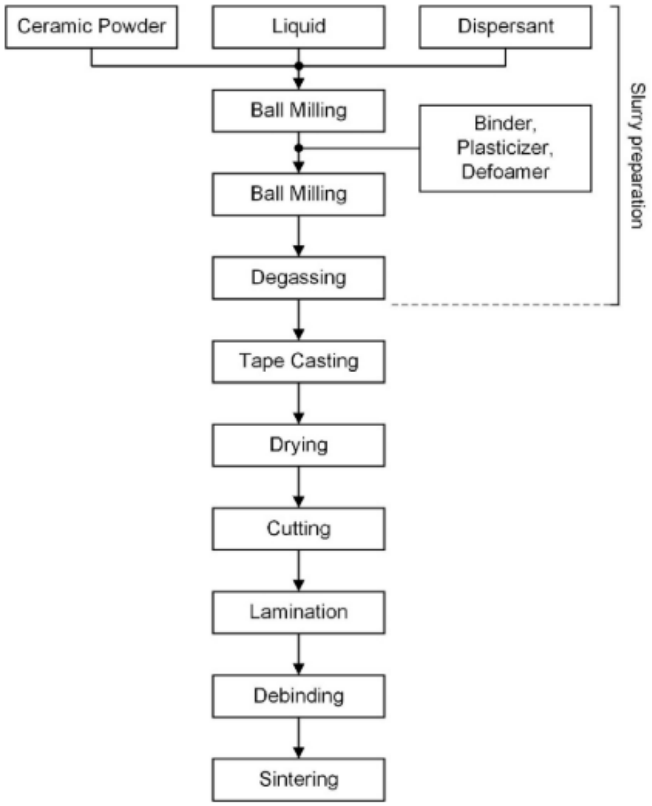

Ref: Nishihora *et al.* (2018)[48].

2.2.1 Slurry stability

Repulsion and attraction forces between ceramic particles determine the stability of the slurry, which is directly related to the physical/chemical properties of particles and the solvent-particle interface. However, attraction forces are considered to be already present due to van der Waals forces and/or other inter particulate forces, i. e. there is already a tendency of particles to stick together. To ensure a well-disperse stable slurry,

the repulsion forces need to be higher than attractions ones and, due to this, dispersants are used. In tape casting processing, the dispersant is the first additive added, which is used to separate and hold the ceramic particles apart. It also permits higher solid loading and decreases the liquid/solvent content of slurries[45, 49].

There are some reasons why a tape casting slurry needs to be well deflocculated. Powders usually tend to form agglomerates, especially powders with high surface area, which will tend to trap air in the interstitial points among particles, and can cause later bad de-airing process, bubbles in the tape, or non-desired porosity after sintering. Well-dispersed particles allow the binder to cover all of them individually, and not in groups of particles. Also, a well-deflocculated slip enhances the packed-bed density of green stacked tapes, reflecting an enhancement of green and fired density of tapes. Lastly, it is easier to obtain a reliable and reproducible final product when there is a homogenous slurry being used in the process[49].

Due to environmental and health issues, the use of water as a dispersion medium and solvent is encouraged. However, this choice faces some challenges as easier powder flocculation and sedimentation (pH instability), the formation of bubbles during the process, and premature polymerization. When pure oxides are dispersed in water, the charge on the hydrated surfaces are determined by H_3O^+ and OH^-. These ions are responsible for changes in the surface charge when the pH of the slurry is modified, adsorbing opposite charges and creating a motionless ion layer, the so-called Stern layer, and another layer with mobile ions (diffuse layer). This model is called the diffuse electrical double-layer model (Figure 6)[8, 50, 51].

Figure 6 – Scheme of the double-layer model with a positive-charged surface.

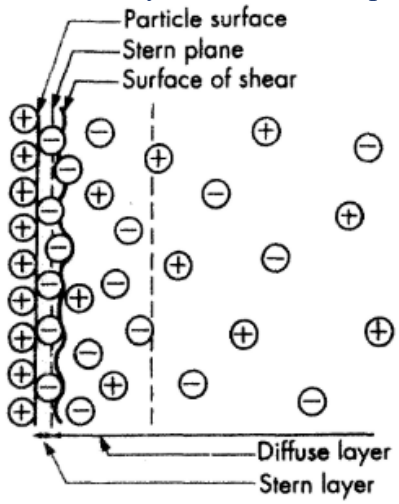

Ref: Shaw (1992)[51].

The difference in charge between the diffuse layer and the electrically neutral layer is called zeta potential (ZP or ζ). The pH where ZP is null (zero) is the isoelectric point (IEP). For example, considering the same two suspensions but with different ZP, the one with the higher value of ZP in modulus will be considered more stable[45]. For tape casting of ceramic oxide powders, the particles can be considered dispersed when ζ is equal to or higher than |40| mV[50].

2.2.2 Rheology of slurries

Rheological properties of ceramic slurries are influenced by physical and chemical properties of the solvent, pH, volume fraction of solids, particle sizes and its form and distribution, besides solvent-particles interaction, and temperature. For tape casting processing, the viscosity of the slip plays an important role in the process. It needs to have a slow viscosity to facilitate casting without sedimentation and high solids content to obtain a high green density and reduces the drying shrinkage. Additives also exert great influence in the rheological properties, such as the binder, that gives to the system a pseudoplastic (shear-thinning) behavior, very welcome in the tape casting process due to the reduction of viscosity when passing through the leveling blade and its quick increase immediately when shearing force ceases[42, 52, 53].

For rheological analysis of tape casting slurries, the Herschel-Bulkley model can be used (Eq. 1):

$$\tau = \tau_0 + K\gamma^n \quad (1)$$

where τ is shear stress, τ_0 is the yield stress, γ is the shear rate, K is the consistency index, and n the flox index (dilatant > 1, Newtonian > pseudoplastic)[45, 53]. Besides, for high-solids content slurries, thixotropy can be observed. This is a time-dependent shear-thinning phenomenon, where the viscosity decreases with time in ascendant shear rates. The viscosity can be recovered during descendant shear rates[54]. Figure 7 shows an example of a thixotropic behavior.

Figure 7 – The flow curve for a typical thixotropic liquid.

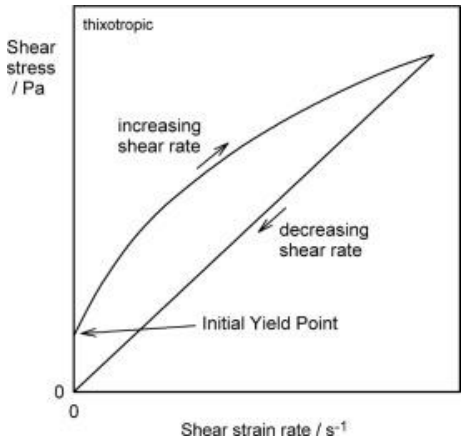

Ref: Ruys (2019)[54].

2.3 The brittleness of ceramics

New materials with better properties and reliability are demanded by the different environments imposed by new technologies. Therefore, ceramics have been proposed and used as a substitute for current materials or as additions to existing ones due to their properties such as excellent hardness, Young's modulus (*E*), mechanical strength, chemical inertness, and thermal stability[55, 56], as seen in Figure 8. Most of these properties are related to the predominant ionic and covalent chemical bonds.

Figure 8 – Young's modulus vs. strength for different materials, including non-technical and technical ceramics (yellow regions).

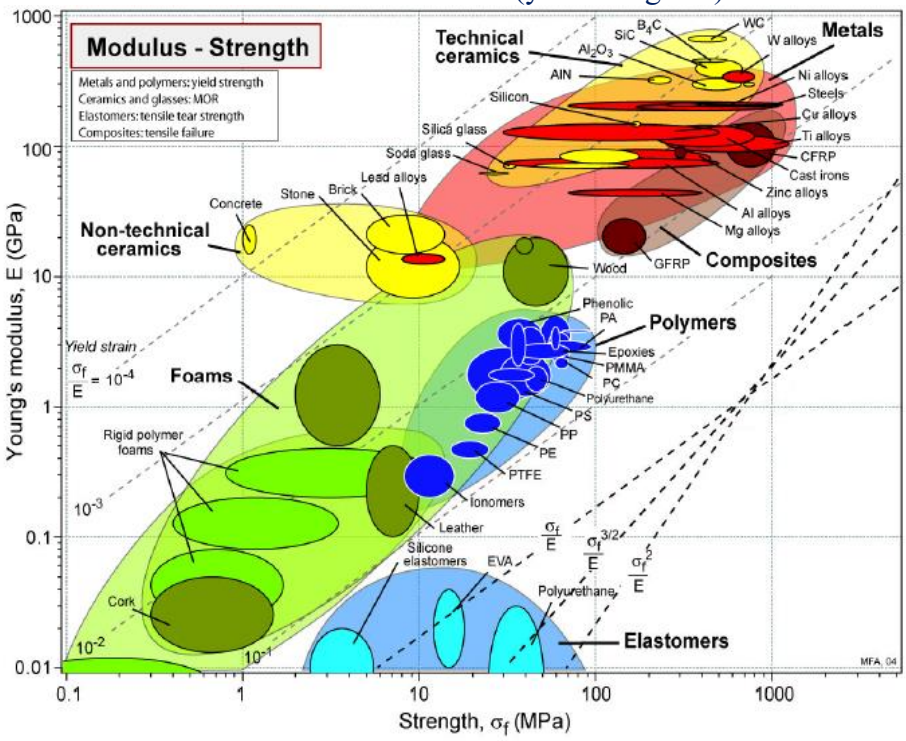

Ref: Ashby (2010)[57].

However, ceramic materials are inherently brittle, which limits their use in components that require reliability and high toughness. The strength of ceramics must be described by statistical parameters (e.g. Weibull analysis[58]) because they contain an unknown variety of cracks and flaws that are introduced during processing and surface machining. Linear elastic behavior and absence of plastic deformation cause the strength of ceramics to be inversely dependent on the size of the critical crack (e.g. Griffith-Irwin theory[59, 60]), which generally cannot be detected except by failure itself. For this reason, a specific ceramic component can exhibit a high probability of failure[61, 62]. When the stress intensity factor (opening fracture, mode I – Figure 9), K_I, reaches its critical value, i. e. when submitted to the maximum stress before failure, then the fracture toughness (K_{IC}) is obtained, following Eq. 2

$$K_{IC} = Y\sigma\sqrt{\pi a} \tag{2}$$

where Y is the geometric scaling factor, σ is the applied stress and a is the crack length. K_{IC} is characterized by "mode I" of stress field applied in the stress concentration, critic for ceramics. Figure 10 presents the fracture toughness of materials, including ceramics, as a function of the elastic limit (strength) and Young's modulus.

Figure 9 – Three rupture modes: opening (I), shearing (II) and tearing (III).

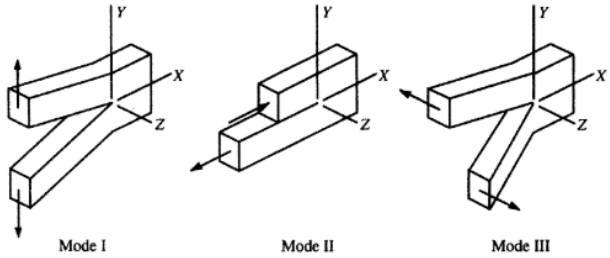

Ref: Barsoum (2003)[63].

Figure 10 – Fracture toughness as a function of strength (on the left side) and Young's modulus (on the right side) for various classes of materials. Ceramics are represented by the yellow regions.

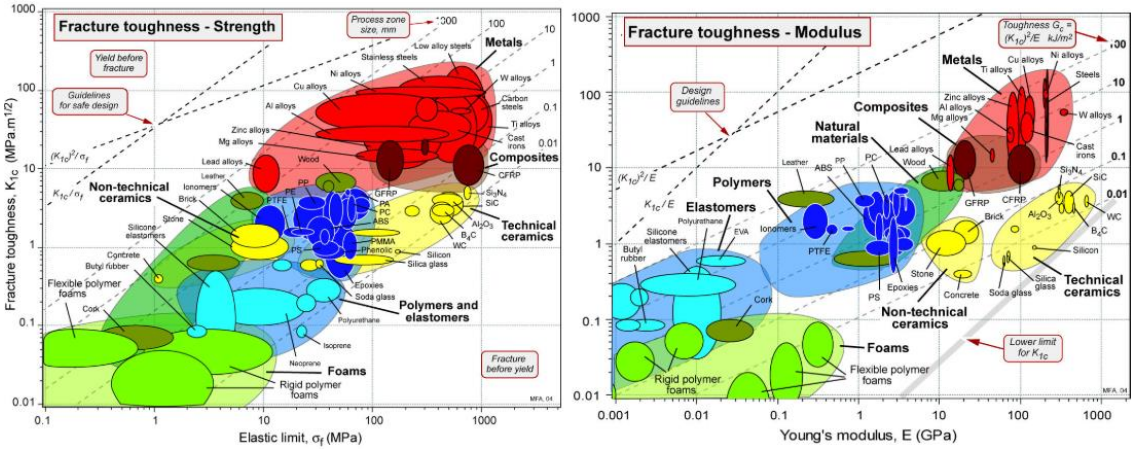

Ref: Ashby (2010)[57].

Thus, many efforts have been made in the last decades to overcome the low toughness and lack of reliability of ceramic components. New materials and processing routes to improve mechanical behavior have been studied. One of the first ideas to enhance the mechanical behavior of ceramics was placed in producing the highest degree of homogeneity in bulk monophasic ceramics, eliminating the flaws that initiate the catastrophic failure or at least reducing their size. However, to achieve something close to a defect-free ceramic, high-cost processes are involved. Another approach was introducing compressive residual stresses at the surface (e.g. strengthening in glass such as Corning® Gorilla Glass®). Nonetheless, significant reduction of strength variability cannot be achieved with these approaches, and new strategies fundamentally different from this have emerged directed to achieve the so-called flaw tolerance. The development of ceramic matrix composites is one of the most promising alternatives[61, 64, 65].

2.4 Ceramic matrix composites

The sensibility of monolithic ceramics to small defects, crack propagation and catastrophic failure resulted in the development of CMC that combines the benefits of monolithic ceramics with high damage tolerance[66]. There are two different classes of ceramic matrix composites: oxide and non-oxide. The non-oxide CMCs present higher creep resistance and typically higher strength than oxide composites. They also present inferior environmental stability if compared with all-oxide composites, limiting their application in oxidative atmospheres at high temperature[1]. The oxide CMCs present the advantage of good alkali corrosion resistance, low dielectric constants, potentially low cost, damage tolerance combined with inherent oxidation resistance, and has good high-temperature mechanical properties in the air. However, a dramatic degradation of mechanical performance of oxide CMCs can be observed at elevated temperatures in steam[67]. In general, CMCs may have particles, short fibers, long fibers, or layers (Figure 11) as a reinforcement phase, which are usually stronger and tougher when compared to the matrix. The presence of the second phase enhances the mechanical properties[64, 68].

Figure 11 – Types of composite based on the form of reinforcement.

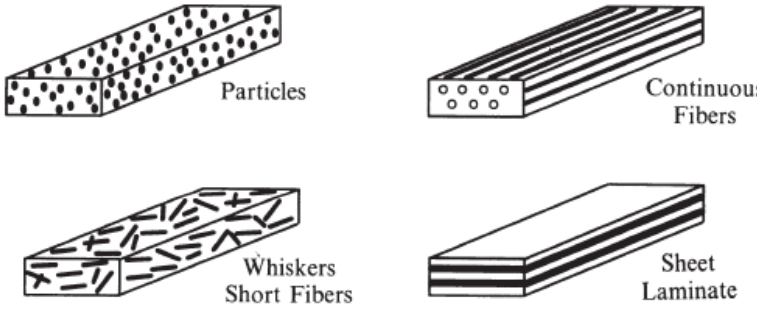

Ref: Chawla (1998)[68].

Continuous fiber-reinforced ceramics exhibit high mechanical and thermomechanical properties. However, the routes available to process the matrix are expensive, and only parts with limited thickness can be obtained. By contrast, short fiber/whiskers or particle-reinforced ceramic composites can be processed following classical routes. The reinforcing phase may be dispersed quasi-isotropically in the matrix, whereas some processing techniques, such as tape casting, allow a preferential orientation of whiskers. Special attention must be focused on laminar composites. These structures provide the advantage for tailoring the properties by stacking layers of different compositions in a suitable sequence[64]. Figure 12 shows stress-strain curves comparing these materials.

Figure 12 – Typical stress-strain behaviors of pure ceramics and different types of reinforced ceramic matrix composites.

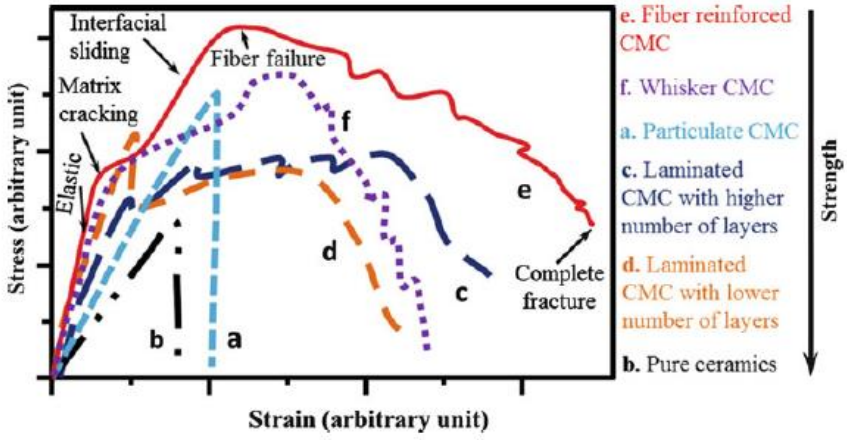

Ref: Kar (2017)[69].

2.5 Laminated composites

In the last decades, new microstructural design concepts have been attempted for improving the fracture toughness of structural ceramics. Among them, doping, fiber and/or particle reinforcement, functional grading, and layered architectural design may be highlighted. Laminar ceramic composites have received a great deal of attention due

to their potential for use in emerging structural applications demanding high mechanical performance. The laminated approach has allowed the fabrication of a new family of composite materials with properties superior to those of monolithic ceramics with microstructures similar to those of the constituent layers. In general, the enhanced mechanical behavior exhibited by these composites cannot be attributed to a simple rule of mixtures of the properties of the constituent materials, but the synergic effect of the laminar structure itself[55].

Multilayer ceramic composites (MCC) consist of two or more ceramic materials that are insoluble in each other and that are sequentially piled symmetrically. Two main approaches regarding the fracture energy of the layer interfaces are particularly useful for dividing MCC into two groups: multilayer composites with weak interfaces or layers and composites with strong interfaces[56, 70].

2.5.1 Weak interfaces or layers

The use of weak interfaces or layers inside ceramic matrix composites is a concept that has been employed for decades in fiber-reinforced composites. The main idea is that weak interfaces or layers cause the delamination and deflection of propagating cracks, similar to what occurs in CMC with long fibers where crack propagates in the direction perpendicular to the fiber alignment utilizing toughening mechanisms (Figure 13)[71]. Once the concept between them is the same, the He and Hutchinson diagram was developed for CMC with fibers can also be used to investigate crack behavior.

Figure 13 – Crack propagation on a ceramic matrix composite reinforced with long fibers under tensile stress.

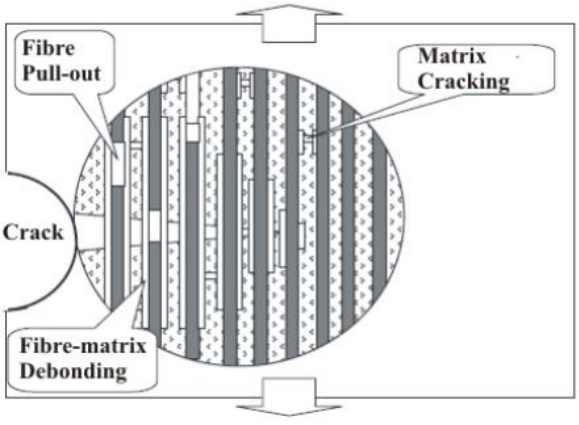

Ref: Adapted from Krenkel (2008)[71].

Since the work by Clegg *et al.* in 1990[72], ceramic-ceramic layered composites have been designed and processed based on weak interfaces between dense and rigid layers to originate crack deflection and their fracture behavior in flexure under loads

perpendicular to the layers has been analyzed in terms of crack propagation and strength. The composite exhibited a fracture toughness that was four times higher and a work of fracture that was up to one-hundred times higher than those of monolithic, indication a non-catastrophic failure (Figure 14) [72, 73].

Figure 14 – Fracture of a SiC multilayered ceramic with weak graphite interfaces tested in a three-point bending test (on the left side), and its respective load-deflection curve (on the right side). Multiple crack deflections were observed, reflecting in a curve with various steps of rising load.

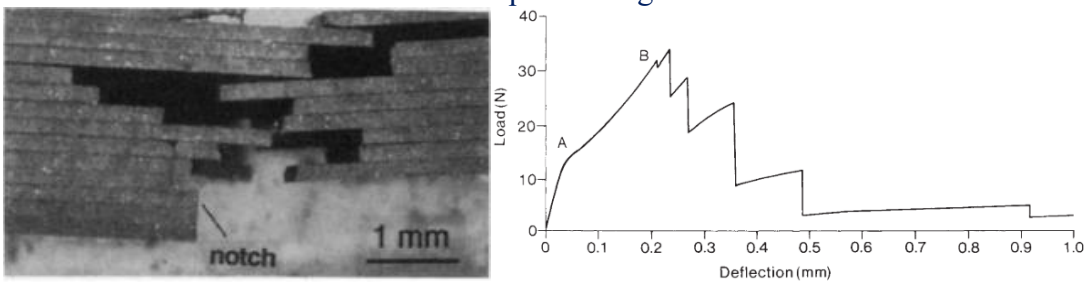

Ref: Clegg *et al.* (1990)[72].

Many studies involving the use of weak interfaces or layers to improve the toughness of ceramics are inspired by natural materials. These biomimetic projects have good potential for improving the toughness, strength, and reliability of the ceramics, which are very important factors for structural purposes. An example is mollusk shells[74], which have a structure that is primarily composed of ceramic material layers intercalated with very thin layers of protein material (Figure 15).

Figure 15 – SEM of the lamellar structure of Strombus gigas shell (a) and a biomimetic material processed by sequential hierarchical engineered layer lamination (b).

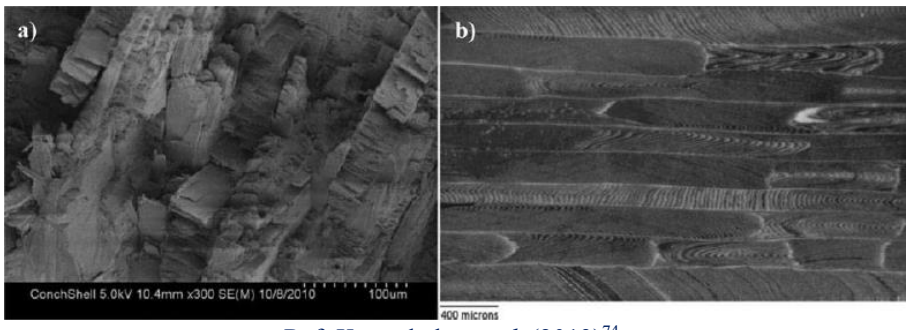

Ref: Karambelas *et al.* (2013)[74].

The selection of the material to compose the weak interface or layer of a multilayer composite is a fundamental step. In general, the matrix layer is responsible for the mechanical strength of the composite, while the weak interfaces determine the toughness and work of fracture. Therefore, to obtain good mechanical strength, toughness, and work of fracture results, the thick layers must have good mechanical strength, while the interface layer must have a low fracture resistance but one that is sufficient for maintaining the integrity of the composite during its utilization. This lower strength of

the interface compared with the matrix layer allows phenomena such as delamination and deflection to occur when a growing crack reaches the interface, which is more evident when the interfacial resistance is low[75, 76]. Some non-oxide materials frequently used as weak interface materials (e. g. graphite, boron nitride, and titanium compounds) usually have much higher fusion temperatures than the material of the matrix layer; thus, during the sintering process, their sintering is incomplete, while the matrix is densified. The incomplete sintering is responsible for the lower strength of the interface compared with the massive part of the composite. In some cases, it is necessary to add a sintering aid to the interfacial layer to prevent the layer from becoming excessively weak, which could significantly affect the strength of the composite[56].

Alternative ways to produce crack deflection are those incorporating different kinds of weak layers such as porous layers[77], layers containing oriented microcracks[78], or heterogeneous layers introduced during the green processing[79] or formed in-situ during sintering[80], as seen in Figure 16. In general, this family of residual stress-free laminates presents graceful fractures together with the strength values of the same order as those of the stiff and dense layers.

Figure 16 – SEM micrographs of different types of crack deflection mechanisms: a - weak interface, b - porous interlayers, c - layers with oriented microcracks, and d - heterogeneous layers.

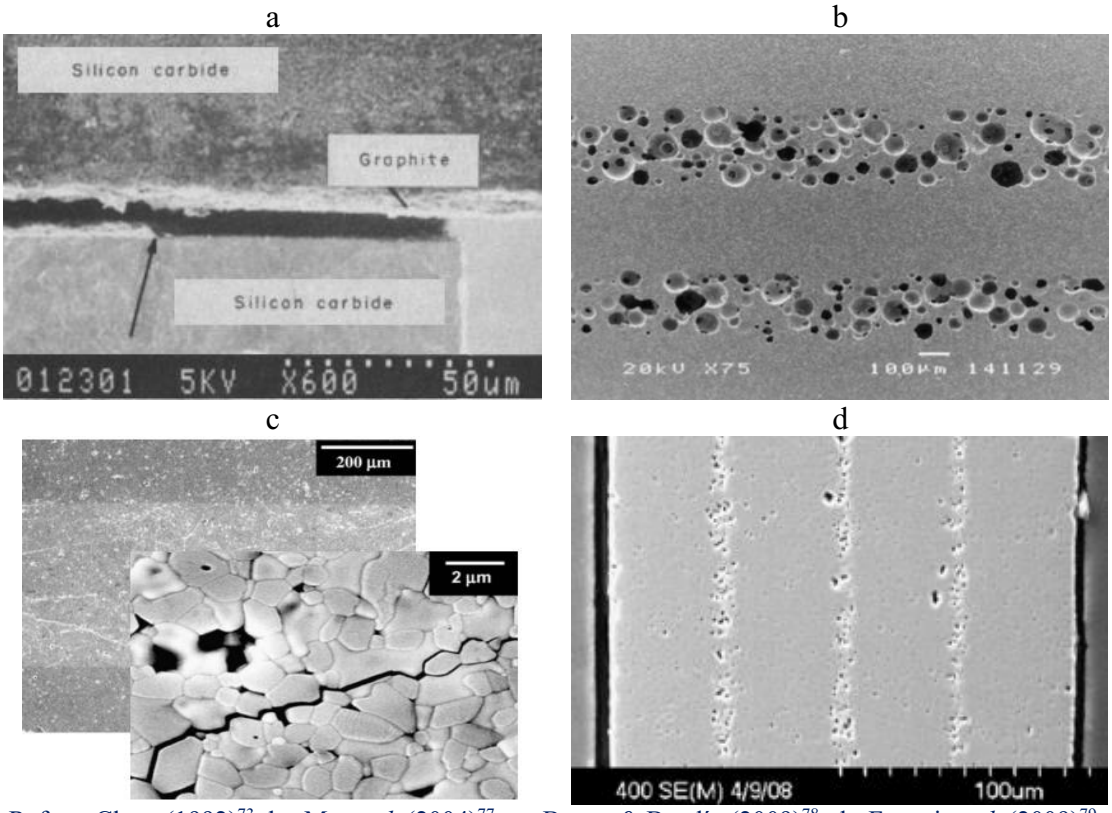

Ref: a - Clegg (1992)[73]; b - Ma *et al.* (2004)[77]; c - Bueno & Baudín (2009)[78]; d - Ferrari *et al.* (2009)[79].

One well-accepted approach regarding the ability of a crack to be deflected in these laminates is to consider the porous interface/layer porous as a bulk material, with its respective fracture and elastic properties. The volume fraction of porosity affects fracture energy. Most of these models consider that crack deflection occurs when the driving force for interfacial crack growth equals the fracture energy of the interface at a lower load than that required for the driving force of the penetrating crack to the fracture energy of the strong phase[81–83]. Interface defects also affect the interfacial properties required for crack deflection[84, 85]. Also, microcracks might grow as the main crack enters the porous layers[86].

These theoretical models predicted that, if there is no elastic mismatch and considering homogeneous porous layers/interfaces with fracture energy of G_p, the crack will be kink out if G_p/G_d<0.57, where G_d is the fracture energy of dense layers. Nevertheless, ensuring that the crack travels in the interface means that the ligament of material between the crack and the pore ahead of it in the interface must fracture, and this relation can be rewritten by changing G_p by the fracture energy of the ligament, G_{lig}. Theoretically, the ligaments in the porous interlayer have the same dense material as that of the dense layers in the laminate. Hence they will have the same fracture energy and the crack should immediately kink out of the porous interface. Nevertheless, practically, it is noted that in the porous interlayers, there exists an interaction effect between the homogeneously distributed pores[87]. Taking the pore interaction effect into account, Davis *et al.*[86] have proposed that G_p can be related to the G_{lig} in the porous interlayer by Eq. 3 and Eq.4.

$$G_p = G_{lig}(1 - V_p) \tag{3}$$

$$\frac{G_p}{G_d(1-V_p)} < 0.57 \tag{4}$$

where V_p is the volume fraction of pores in the porous interlayers. Figure 17 illustrates better the idea of the properties of the above equations.

Figure 17 – Scheme of a crack being deflected in a porous interlayer.

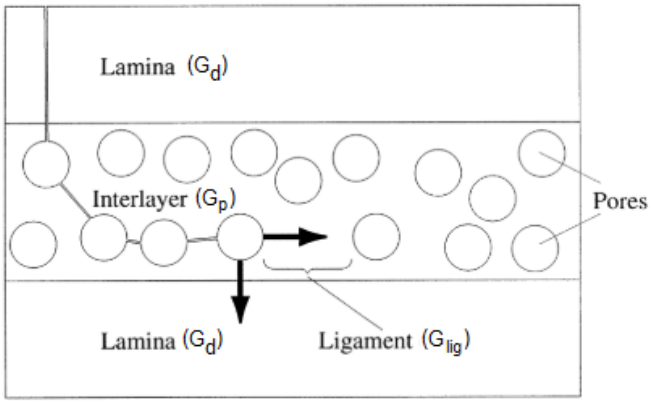

Ref: Adapted from Blanks *et al.* (1998)[83].

Ma *et al.*[77] compared a monolithic specimen with a layered composite of the same material with porous layers. Figure 18 shows the load vs. displacement curve of bending tests, the final energy absorbed as a function of interlayer porosity estimated after considering the effect from crack deflection length and porosity, and an SEM micrograph showing the crack deflection of a layered composite with 57.6 vol% of interlayer porosity.

Figure 18 – Load vs. displacement and fracture work vs. volume fraction of porosity curves, and the SEM micrograph of the fractured layered composite with 57.6 vol% of interlayer porosity.

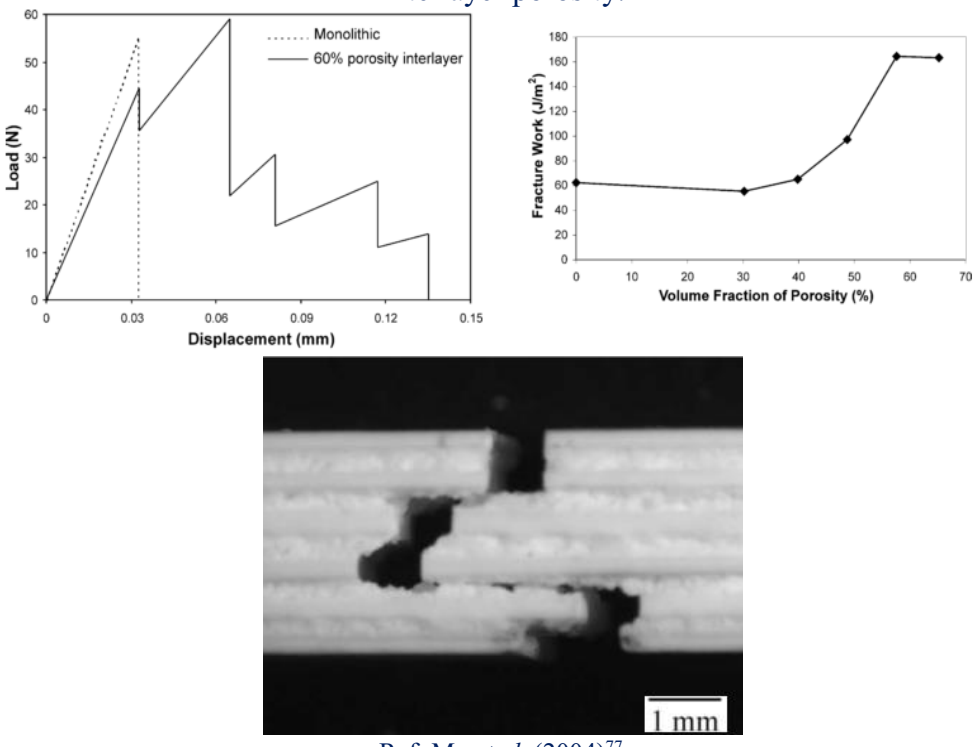

Ref: Ma *et al.* (2004)[77].

In Figure 19, data obtained of samples by Ma *et al.* and Davis *et al.* was set in a R_p/R_d vs. relative density curve, to observed if crack penetrated or deflected as expected

for each case (He and Hutchinson's diagram). The results showed that Eq. 4 provides a good prediction on crack behavior.

Figure 19 – The relationship between relative fracture energy between the dense and porous layers and the porosity in the porous interlayers. Circle symbols represent data from Davis *et al.*[86], and delta symbols are from Ma *et al.*[77]. Filled symbols indicate situations where cracked deflection was observed.

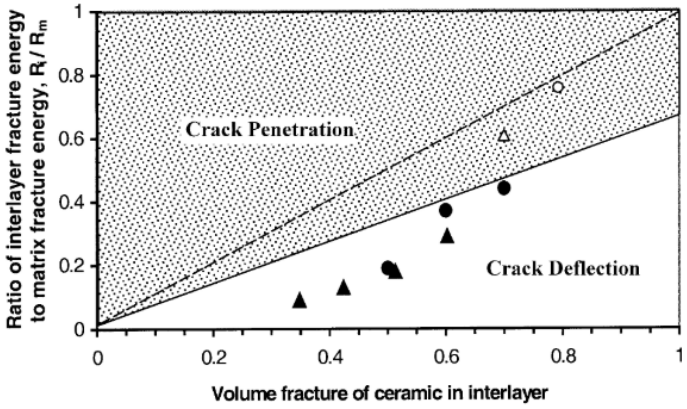

Ref: Ma *et al.* (2004)[77].

2.5.2 Strong interfaces

Studies of multilayer ceramic composites employing strong interfaces between layers can result in considerable improvements in properties such as the work of fracture[88], flexural strength[89], and fracture toughness[88, 90, 91] of the laminate compared with the monolithic base material. In some cases, although there is no significant increase, the flexural strength is maintained and, in general, with more uniform values than for the respective monolithic materials. This can be due to the presence of residual stresses in the layers[92]. The microstructural design (e.g. grain size, layer composition) can also influence the crack growth resistance behavior (R-curve), for example, using two distinct materials with consequently different elastic modulus and use the elastic modulus transfer to enhance mechanical properties[93–95].

The elastic mismatch during sintering between adjacent layers, resulting from the difference in Young's modulus, thermal expansion coefficients, chemical reactions, and/or phase transformations, generates residual stresses throughout the material. These residual stresses can be controlled to improve their mechanical properties. On ceramics and glasses, for instance, the compressive stresses on the surface have proven to be useful for increasing their fracture strength. On the other hand, laminar ceramics designed with compressive stresses in the bulk may present a threshold strength below which catastrophic failure does not occur[91].

The utilization of tailored compressive residual stresses acting as physical barriers to crack propagation has already succeeded in many ceramic systems (e. g. alumina/mullite[96], alumina/zirconia[97], and alumina/silicon carbide[98]) and all different configurations have shown peculiar crack propagation. Residual compressive stresses inside multilayer ceramic composites may significantly alter the propagation behavior of a growing crack and, therefore, increase the energy needed to promote its propagation and the consequent breakage of the specimen[99]. The deflection and bifurcation (Figure 20) of cracks are the main crack propagation mechanisms in multilayer composites with residual internal compressive stresses[100].

Figure 20 – The deflection (a), and bifurcation (b) of growing crack when it reaches layer under compressive stress in alumina-zirconia laminates.

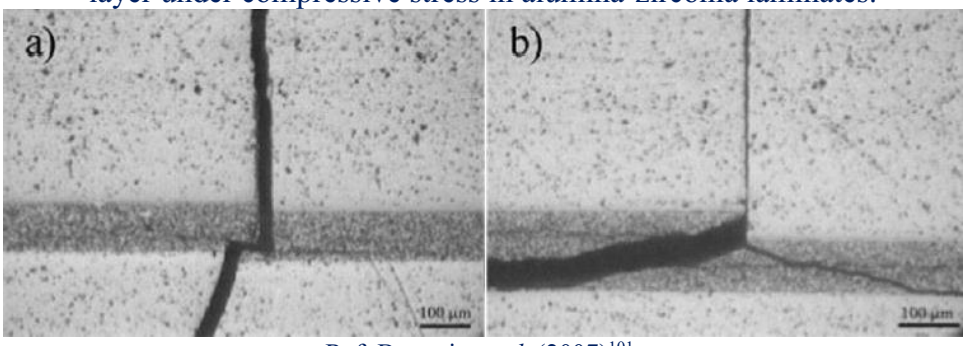

Ref: Bermejo *et al.* (2007)[101].

The tendency generated by the compressive stresses is to laterally deviate the cracks, which propagate with more intensity parallel to the interfaces. In contrast, residual tensile stresses promote the propagation of the crack perpendicular to the interface[102, 103]. However, the existence of compressive stresses in the multilayer composite is not sufficient for the deviation of the path of a growing crack to occur. This behavior depends on several factors, which led to the development of theoretical studies on the subject that use mathematical tools to predict the fracture behavior of these composites, especially regarding the occurrence or absence of the bifurcation of growing cracks[90, 99, 104–107].

The effect of the thickness of the internal compressive layers on the occurrence of deflection or the bifurcation of the crack was also studied[90]. It was observed that a minimum composite thickness is required, which is dependent on the elastic and thermal characteristics of the component materials, the total thickness of the composite, and the number of layers that constitute the composite. Náhlík *et al.*[105] used a mathematical tool to simulate the deviation behavior of crack propagation in multilayer ceramic composites under flexion and obtained optimal values of the thickness and number of layers to improve failure resistance that was consistent with experimental data. Likewise, Rao

et al.[44] observed catastrophic failure of multilayer components with compressive layers that were too thin or with too low residual compressive stresses, demonstrating that is needed a minimum thickness to achieve non-catastrophic failure behavior.

2.6 R-curve behavior

The improvement of fracture resistance through the insertion of reinforcement phases is due to the reduction of the crack propagation drive in its extremity. This behavior is the so-called R-curve behavior, observed in many multilayer composites with strong interfaces[88, 91, 95, 107–111]. The presence of compressive tensions inside multilayer composites results in this controlled fracture behavior, characterized by the R-curve behavior. The cracking toughness of multilayer composites exhibiting this behavior increases as the crack advances layer through the layer, with high toughness peaks in the layers under residual compression. The R-curve behavior is more pronounced for composites with higher residual compressive stresses. All of these effects contribute to the increase in the energy spent in the rupture of the ceramic, which implies an increase in the toughness and the work of fracture compared with a similar monolithic material[88].

Thus, the measured fracture toughness and crack growth resistance behavior (R-curve), which depend on microstructure and residual stress, become functions of position within the composite. The apparent R-curve of a laminate can be calculated considering the equilibrium condition at the crack tip, i.e. crack propagation is possible if the stress intensity at the crack tip (K_{tip}) equals or exceeds the intrinsic material toughness, K_{IC} (Eq. 5). The crack length is a:

$$K_{tip}(a) \geq K_{IC} \qquad \text{being} \qquad K_{tip}(a) = K_{app}(a) + K_{res}(a) \tag{5}$$

where $K_{app}(a)$ is the applied stress intensity and $K_{res}(a)$ is the stress intensity contribution from the residual stress. Solving for $K_{app}(a)$ (Eq. 6) holds:

$$K_{app}(a) \geq K_{IC} - K_{res}(a) = K_R \tag{6}$$

where $K_{app}(a)$ equals the desired effective R-curve, K_R.

In fracture mechanics, both residual and applied stresses are usually included in the crack driving force. However, it is useful to consider the residual stresses as part of the crack resistance. Thus, in laminates with compressive stress at the surface, the higher resistance to failure results from a reduction of the crack driving force rather than from an increase in the intrinsic material resistance to crack extension.

Besides, a fracture mechanics weight function analysis was effectively used to estimate the crack growth resistance behavior (R-curve) as a function of the position of an edge crack within each multilayered system investigated (Eq. 7). The so-called apparent fracture toughness K_R (since it is influenced by the residual stresses) for an arbitrary stress distribution $\sigma_{res}(x)$ normal to the layer plane, may be defined as follows:

$$K_{res}(a) = \int_0^a h(a,x)\,\sigma_{res}(x)dx \qquad (7)$$

where x is the distance along the crack length measured from the surface, a is the crack length, and $h(a,x)$ is a weight function as developed by Fett for an edge crack in a bar[112], commonly employed in the evaluation of R-curve behavior for multilayered systems[44, 110] (Eq. 8):

$$h(a,x) = \sqrt{\frac{2}{\pi a}}\,\frac{1}{\sqrt{1-{}^{x}/_{a}}\left(1-({}^{a}/_{W})\right)^{1.5}} \times \left[\left(1-\frac{a}{W}\right)^{1.5} + \sum A_{\nu\mu}\left(1-\frac{x}{a}\right)^{\nu+1}\left(\frac{a}{W}\right)^{\mu}\right] \qquad (8)$$

the coefficients $A_{\nu\mu}$ and values of the exponents ν and μ are given in literature[113, 114]. W is the total thickness. It is worthy of note that is not dependent on Young's modulus exclusively in the case of a homogeneous material[91, 108].

Moon *et al.*[110] produced a 80Al (80 vol% alumina + 20 vol% tetragonal zirconia)/90Al (90 vol% alumina + 10 vol% tetragonal zirconia) layered composite (Figure 21a). Figure 21b shows the scheme of the stress distribution showing the three independent stress components, bending ($\sigma_{bend}(x)$), residual stress ($\sigma_r(x)$), and bridging ($\sigma_{br}(x,a)$).

Figure 21 – The laminate produced by Moon and co-authors with thick 80Al alternated with 90Al thin layers: optical micrograph of the post cracked SEVNB sample showing the layer stacking concerning the V-notch (a), and the schematic of the stress distribution (b).

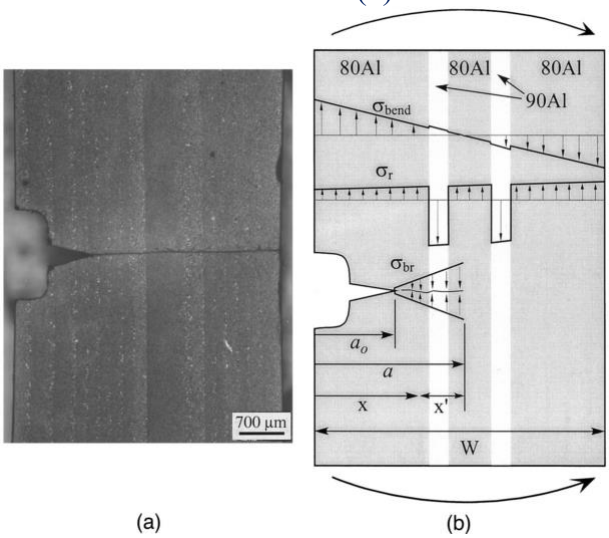

Ref: Moon *et al.* (2002)[110].

To compare with the layered composite R-curve, a monolithic sample of 80Al was produced and tested (Figure 22). As mentioned before, the value of fracture toughness increases with the increase of crack size, once the energy necessary to crack propagation is increased as the flaw increases (until a threshold).

Figure 22 – The R-curve of the 80Al monolithic reference sample: The ♦ points were measured experimentally with the calculated K_R and K_0^{80Al} profiles. The ■ point is K_i for crack initiation from the V-notch tip.

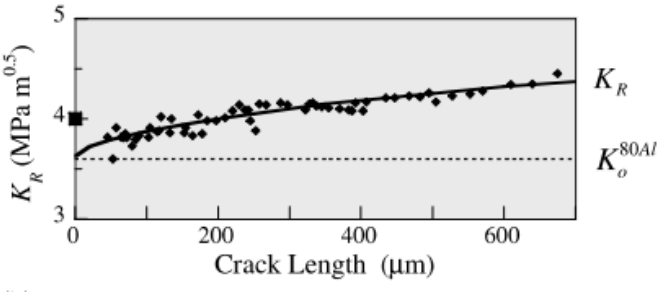

Ref: Moon *et al.* (2002)[110].

When the authors produced a laminated ceramic, R-curve presents a peculiar behavior. The value of K_R decreases slightly due to tensile stresses in this layer. However, when toughness starts to be measured in the compressive layer is possible to see a sharp increase in R-curve. The residual stresses showed a direct influence on the values of K_R. The thickness also influences R-curve behavior. As tensile layers are thicker, their stresses have a slower modulus compared to compressive stresses. That is why the variation in angular coefficient R-curve is more pronounced in the compressive layer than in the tensile layer (Figure 23).

Figure 23 – The R-curve measured for 80Al/90Al layered sample: The ♦ points were experimentally measured with K_R profiles. The straight line is the K_R profile calculated with ΔT = 1225 °C. The dashed line represents the influence of a ± 100 °C variation of the ΔT. The ■ point is K_i for crack initiation from the V-notch tip.

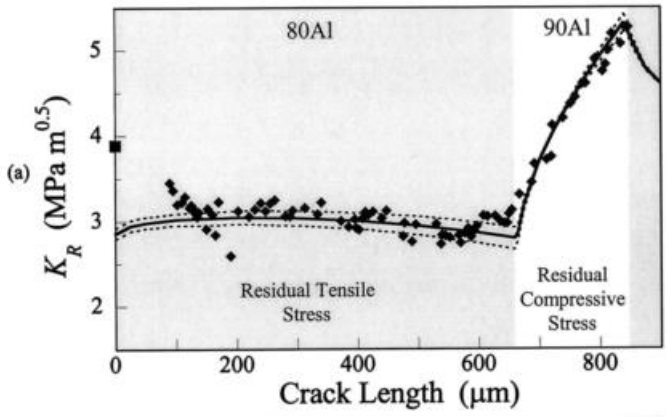

Ref: Moon *et al.* (2002)[110].

Lube *et al.*[108] demonstrated the influence of layer thickness in the R-curve behavior of alumina-zirconia composites (Figure 24). When tensile layers are thicker than

compressive layers, $t_t >> t_c$, toughness decreases slightly in the first ones and increases quickly in the last ones. Changing the layout for $t_c >> t_t$ the opposite happens, toughness increases slightly in compressive layers and decreases quickly in tensile layers.

Figure 24 – Two different layouts of thickness ratio with the same layer composition resulting in different fracture processes.

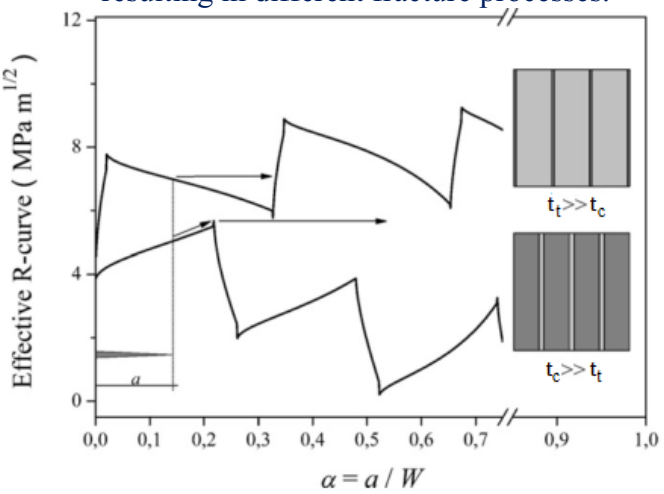

Ref: Adapted from Lube *et al.* (2007)[108].

Recent technologies regarding fracture toughness measurements allow building an R-curve with controlled crack propagation automatically with one single sample, as the device presented ana growth along the whole R-curve is achieved automatically by loading and unloading the sample via computer control. The control is realized by continuously evaluating the slope of the force-displacement curve during the measurement, detecting all kinds of energy release in the sample even without visible crack propagation. After each unloading, the compliance is measured automatically based on the modulation technique (displacement modulation), which allows in a second step to calculate (automatically) the crack length using a formula or a meaasured calibration function. The R-curve measurements are easily performed since the operator does not need to control the crack growth by himself[115]. Figure 25 and Figure 26 present R-curve measurements, and the comparison between data obtained manually and automatically.

Figure 25 – Comparison between force-displacement curves for metal infiltrated alumina measured manually (optically, a) and automatically (b).

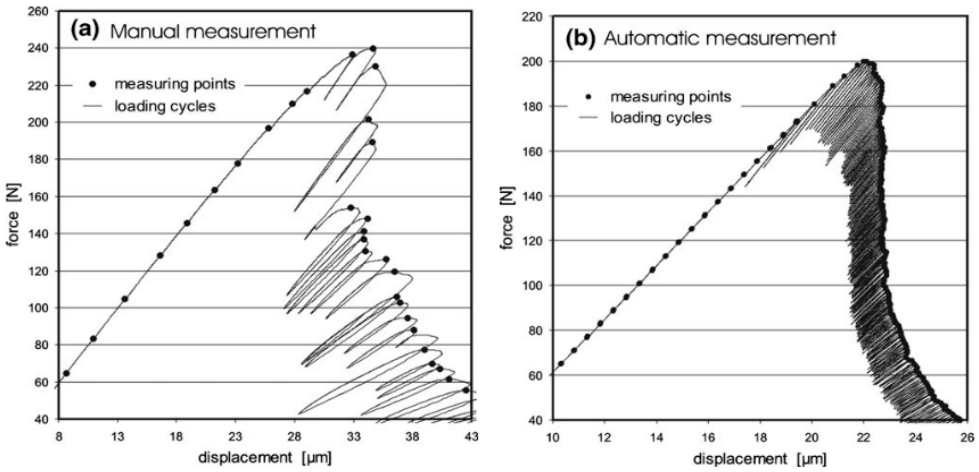

Ref: Jelitto *et al.* (2013)[115].

Figure 26 – Example of two R-curves measured in a zirconate titanate sample, one manually and the other automatically.

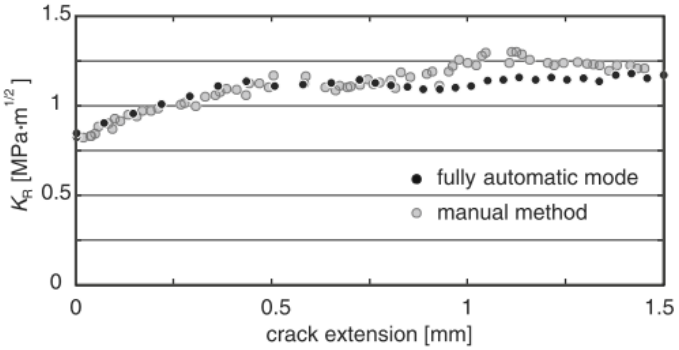

Ref: Jelitto *et al.* 2013[115].

Chapter 3 – Colloidal processing and characterization of TiO_2-MnO-doped alumina/alumina slurries and tapes[1]

3.1 Introduction

Tape casting is a wet-shaping process for producing flat and thin ceramics sheets with thicknesses in the range of 1 to 1000 μm. This technique is applied to produce electronic substrates, multilayered capacitors, piezoceramics, solid oxide fuel cells' components, functionally graded materials, and porous membranes or substrates[49, 121]. Tape casting slurries are typically composed of ceramic powder, solvent (water or organic), and additives such as dispersants, binders, plasticizers, and antifoams[19, 122]. These components are put together in the milling and mixing steps, in the correct order to ensure the slurry homogeneity and a typical pseudoplastic rheological behavior[45]. The processing of tapes consists of casting a ceramic slurry through a leveling blade with a preset gap over a collector film, forming the continuous tape[46]. Several non-oxide and oxide ceramic tapes, particularly alumina, have been developed and produced [41, 48, 123–127].

The slurry optimization is a critical step in this processing, i.e., defining the amount of each component, choosing additives, and consolidating the preparation procedure. Taking into account environmental and safety issues, the importance of using water as a solvent to produce tapes is increasing. Some advantages of the aqueous route are non-inflammability, non-toxicity, and relatively low cost[47, 128–130]. However, the optimization of the rheological and drying parameters to achieve a suitable water-based slurry faces some challenges[123]. The surface charge of powders is an important property for processing colloidal routes, which is characterized by the zeta potential[50]. Thereby, the isoelectric point corresponds to a pH value or range denoting a tendency for agglomeration when the zeta potential approaches zero[53]. When different oxides are mixed in a suspension, even in low amounts, a so-called heterocoagulation occurs when, at a certain pH, the particle surfaces are positively and negatively charged, and attract each other.

An aqueous slurry is a complex multiphase system with low tolerance to changes in drying conditions, casting composition, and film thickness. Crack-free uniform green tapes are possible only when all variables are well controlled[42, 131]. Good quality tapes are

[1]Published in the *Int J Ceramic Eng Sci.* https://doi.org/10.1002/ces2.10087.

characterized by the absence of defects during drying, handling, homogeneity and lamination, debinding, and sintering high capabilities. Green tapes are normally submitted to the burn-out of organics, which is another important step to be controlled. It is usually carried out at low temperatures (<500 °C) at a very low heating rate. Heating up needs to be designed in a way that the component's evaporation rate does not surpass the diffusion rate. Otherwise, the vapor formed inside the green material can lead to the formation of cracks and/or defects[45, 47].

In this chapter, the selected powders and the respective suspension and tapes will be characterized before firing. MnO and TiO_2 are added to Al_2O_3 to work as sintering aids. Both ceramic oxides were already reported in the literature as effective dopants to enhance densification and sintering rate[28, 34, 132], with improved results when they are combined[26]. The stabilization of a colloidal suspension and, as a consequence, a homogeneous distribution of dopants inside the alumina matrix during sintering is the challenge. Since the diffusion of nanocomponents is intrinsically related to homogeneously distributed dopants in the matrix, a key point is to guarantee that titanium dioxide and manganese oxide particles are well dispersed right from the beginning within the aqueous suspension. An optimization of colloidal processing features to avoid particle agglomeration is mandatory. Therefore, the focus of the present chapter is to produce defect-free ceramic tapes to be shaped as laminates and submitted to thermal treatments.

3.2 Materials and methods

3.2.1 Oxide powders

To produce ceramic tapes, two types of alumina and two sintering aids were used as starting powders (Table 3). The alumina powders were a high purity submicrometric alumina powder (Taimicron TM-DAR, Taimei Chemicals Co., LTD., Japan), and coarser alumina (CT 3000 SG, Almatis GmbH, Germany). Home-made alumina doped with titanium dioxide and manganese oxide was produced using high-energy ball milling (Netzsch PE075, Netzsch Group, Germany), named as D. In this case, the Taimicron TM-DAR was used as the main powder, together with 1.68 wt% of titanium dioxide (RD3, Kemira Oyj, Finland) and 2.32 wt% of manganese oxide (Manganese (II) oxide, Sigma-Aldrich Corporation, Germany). A 500 cm^3 alumina crucible, 1400 g of 3 mm diameter zirconia balls (YTZ®, Nikkato Corporation, Japan), and 200 ml of ethanol 99% were used as grinding and liquid media, respectively. Attrition milling was performed on 160 g powder batches at 600 RPM for 2 h. After milling, the mixture was dried in air at room

temperature and sieved with a 200 µm open sieve in a vibratory sieve shaker (AS 200 Digit cA, Retsch GmbH, Germany).

Table 3 – Oxide powders used for the production of ceramic tapes by tape casting.

Name	Composition	Brand name	d_{50} (µm)	ρ (g/cm^3)	Function
A	α-Al_2O_3	Taimei Chemicals Co., LTD.	0.10	3.96	Matrix
C	α-Al_2O_3	Almatis GmbH	0.40	3.90	Matrix
M	MnO	Sigma-Aldrich Corporation	8.00	5.45	Dopant
T	TiO_2 (rutile)	Kemira Oyj	0.08	4.00	Dopant

To characterize the raw powders, scanning electron microscopy (TM 3030, Hitachi, Japan) was performed with 15 kV. Particle size distribution (PSD) was measured by dynamic light scattering (DLS, Zetasizer Nano ZS, Malvern Panalytical, UK) in aqueous suspensions with 0.01 wt% of powder. Zeta potential (ZP) was measured (Zetasizer Nano ZS, Malvern Panalytical, UK) with automatic titration using NaOH and HCl solutions for pH from 2 to 12. In both PSD and ZP analyses, 1 wt% (referred to solids) of ammonium polymethacrylate solution (Darvan C-N, Vanderbilt, USA) was used as a dispersant agent, and samples were ball milled for 4 h. X-ray diffraction (XRD) was performed at room temperature in a diffractometer (Miniflex, Rigaku Corporation, Japan) in the 2θ angle range varying from 5° to 90°, and crystalline phases were characterized using a database (PDF-2, ICDD, USA). The doped alumina powder quantification of crystalline phases was measured using the Rietveld refinement method with powder pattern analysis software (X'Pert HighScore Plus, Malvern Panalytical, UK).

3.2.2 Characterization of slurries and tapes

Optimization of solids content and preparation of slurries were previously set[133]: 21 vol% of solids for undoped and doped fine alumina, 25 vol% of solids for coarse, pure alumina. For calculating the powder quantities, the density of 3.96 g/cm^3 for A and C, and 4.00 g/cm^3 for D were used. In the first step, the powder was deagglomerated in deionized water with the addition of 2 wt% of dispersing agent (Darvan C-N) using ball milling for 4 h. Then, a binder (Mowilith LDM 6138.BR liq, Archroma, Switzerland), a non-ionic surfactant (Ninol PK-80 BR, Stepan, USA), and an antifoamer (Antifoam Y-30, Sigma-Aldrich, Germany) were added with 30 wt%, 1.5 wt%, and 1 wt% respectively, and ball milled for more 30 min. The amount of additives (in wt%) were added referred to the solids content. Slurries were placed in an ultrasonic bath (Q1.8L, Eco-Sonics, Brazil) for 5 min and left to rest for 1 h to ensure all bubble removal.

The rheological behavior of slurries was analyzed with a shear-controlled rotation viscometer (550 Haake™ Viscotester™, Thermo Fischer, USA) with concentric cylinders (SV2P), coupled with a temperature controller (DC-10, Thermo Fischer, USA). Tests were performed at 25 °C, at shear rates varying from 0.02 to 500 s^{-1}. Between the ramps of increasing and decreasing shear rate, a plateau of 60 s was set at 500 s^{-1}. Fitting was carried out according to Herschel-Bulkley's model using dedicated software (Haake™ RheoWin™, Thermo Fischer Scientific, USA).

The slurries were cast on a silicone-coated Mylar® band at a casting speed of 6 cm/min using a tape casting machine (CC-1200, Tape Casting Warehouse, Inc., USA). Tapes were then dried in air at room temperature for 24 h. The upper and bottom surfaces of tapes were characterized using scanning electron microscopy (TM 3030, Hitachi, Japan) at a voltage of 15 kV on gold-coated surfaces. Differential scanning calorimetry analyses (DSC) were performed together with thermogravimetry (TGA) in a simultaneous thermal analyzer (TGA/DSC 1, Mettler-Toledo GmbH, Germany). As a reference, the fine alumina tape was used, since the organics constituents are the same for all tapes. The test was carried out in synthetic air (20% oxygen + 80% nitrogen) from room temperature up to 550 °C, at a heating rate of 1 °C/min. After a dwell of 1 h, the sample was heated to 800 °C with a heating rate of 5 °C/min.

The linear shrinkage behavior of each type of tape was measured by dilatometry (DIL 402 PC, Netzsch Group, Germany) in air. Tapes were heated until 600 °C at a heating rate of 1 °C/min. After a dwell of 1 h, the samples were heated again up to 1200 °C for the fine alumina undoped and doped samples up to 1350 °C for the coarse alumina. These temperatures were chosen according to the sintering temperatures that should be used to consolidate the final composites as discussed elsewhere[20]. Then, after a holding time of 2 h, the samples were cooled down to room temperature at 10 °C/min. The energy-dispersive X-ray spectroscopy (EDS, AZtecLive, Oxford Instruments, UK) was performed with the help of a scanning transmission electron microscope (STEM, Helios NanoLab G3, FEI™, USA) to investigate dopants diffusion in doped alumina. XRD was performed as cited in the section before.

3.3 Results and discussion

3.3.1 Powders structure and composition

Figure 27 shows the micrographs of oxide powders used to produce the tapes. Alumina powders presented faceted irregular shapes, while doped alumina powder showed larger particles due to the mixing and drying processes which caused agglomeration.

Figure 27 – Micrographs of raw oxide powders used to produce the ceramic tapes. Samples A and C are as received, while sample D is the alumina doped powder after milling and sieving.

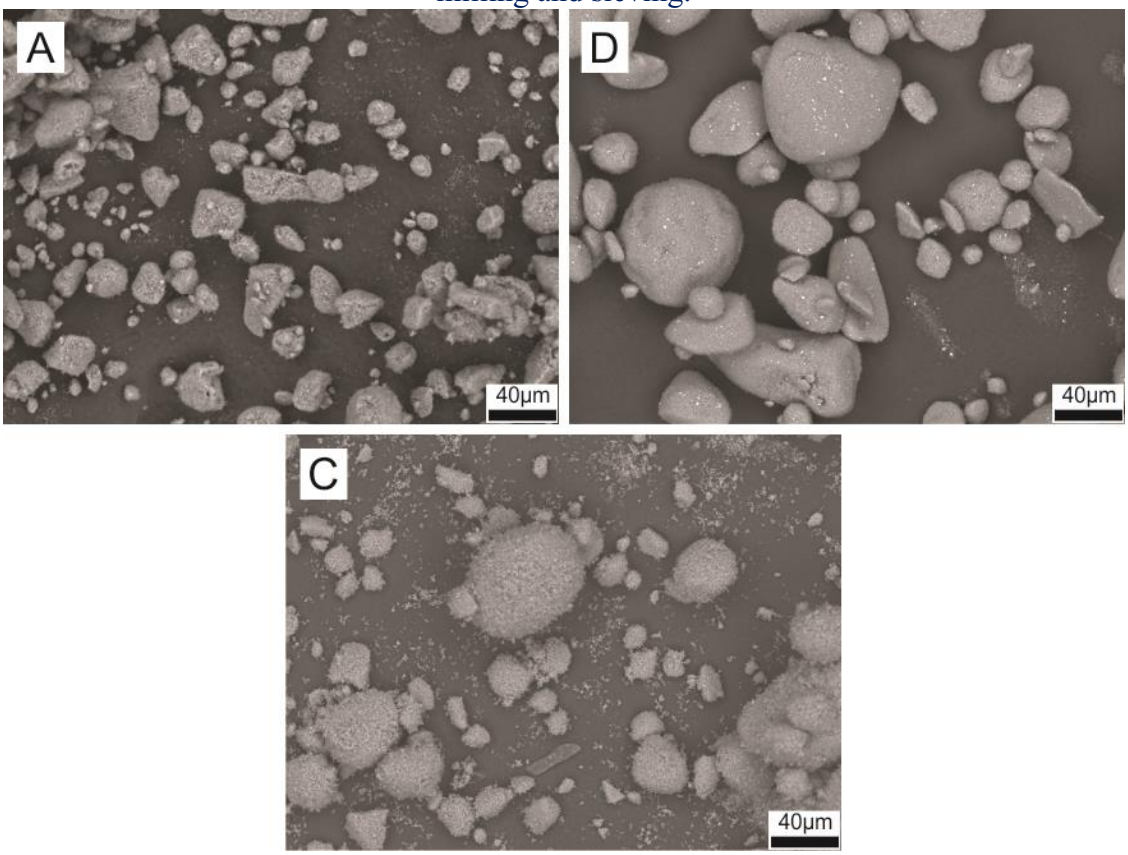

Figure 28 presents the particle size distribution for the raw powders and Table 4 summarizes the values of d_{10}, d_{50}, and d_{90}. Particle size analyses showed that particle size distributions are unimodal. However, only the average particle size value provided by the manufacturer for the coarse alumina (C) is comparable to the ones obtained by analyses. The d_{50} value of finer alumina is higher than that specified by the manufacturer, and the reason might be connected to the formation of small agglomerates due to the high surface area of this powder, even using a dispersant. The undoped (A) and doped (D) fine alumina powder presented a similar value of d_{50}, corroborating the previous measurements and indicating the well-succeeded milling/mixing of added dopants, MnO, and TiO_2, with no changes in the final particle size.

Figure 28 – Particle size distribution of oxide powders. Volume, in percent, is plotted as non-cumulative and cumulative on the left and right Y-axis respectively. A – fine alumina, C – coarse alumina, D – doped fine alumina.

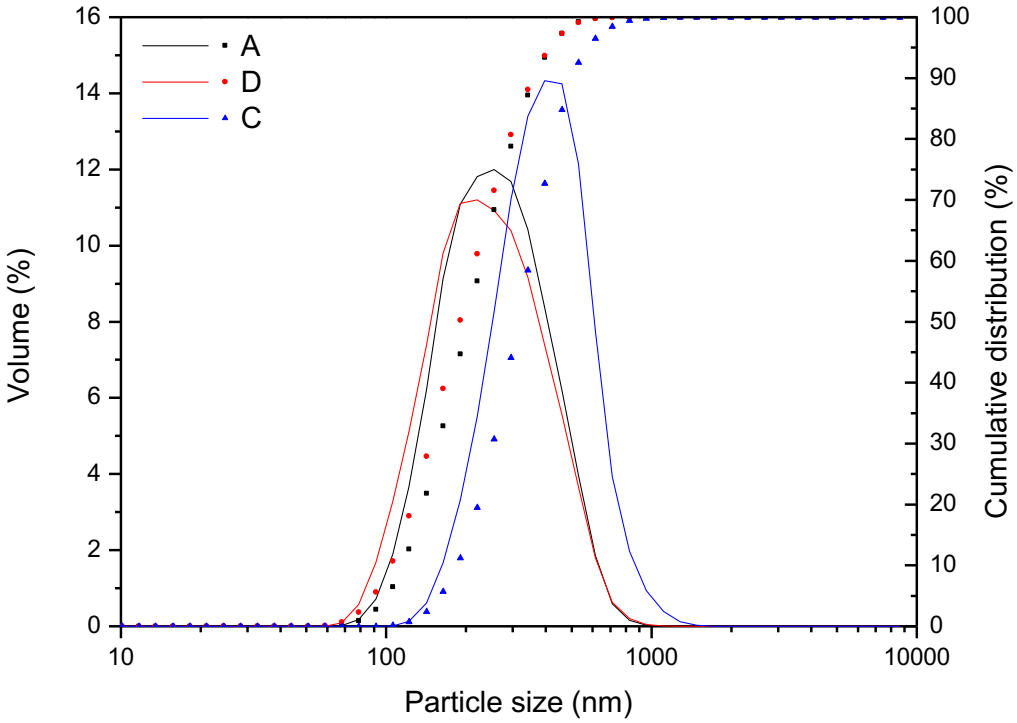

Table 4 – Values of d_{10}, d_{50}, and d_{90} analyzed by DLS for the oxide powders.

	Average particle size (nm)		
Powder samples	**d_{10}**	**d_{50}**	**d_{90}**
A	158	278	494
D	121	264	493
C	202	439	753

Figure 29 shows the X-ray diffraction patterns of oxide powders, for 2θ ranging from 20° to 80°. The Al_2O_3 samples presented α-alumina phase (PDF 01-071-1125), while titanium dioxide and manganese oxide presented rutile (PDF 01-076-0325) and cubic MnO (PDF 01-077-2363), respectively. The doped alumina system presented the three previously mentioned crystalline phases, and the Rietveld refinement quantified 95.8% for α-alumina, 1.9% for rutile, and 2.3% for cubic MnO. Is important to cite that, the attrition milling used in the processing of powder D can produce a small amount of residual zirconia, however, its peaks were not detected in XRD analyses and the presence of zirconia in the total composition is negligible.

Figure 29 – X-ray spectra of manganese oxide, titanium dioxide, undoped (A - fine, C - coarse), and doped (D) alumina raw powders. Crystallographic identification according to PDF-2 ICDD database.

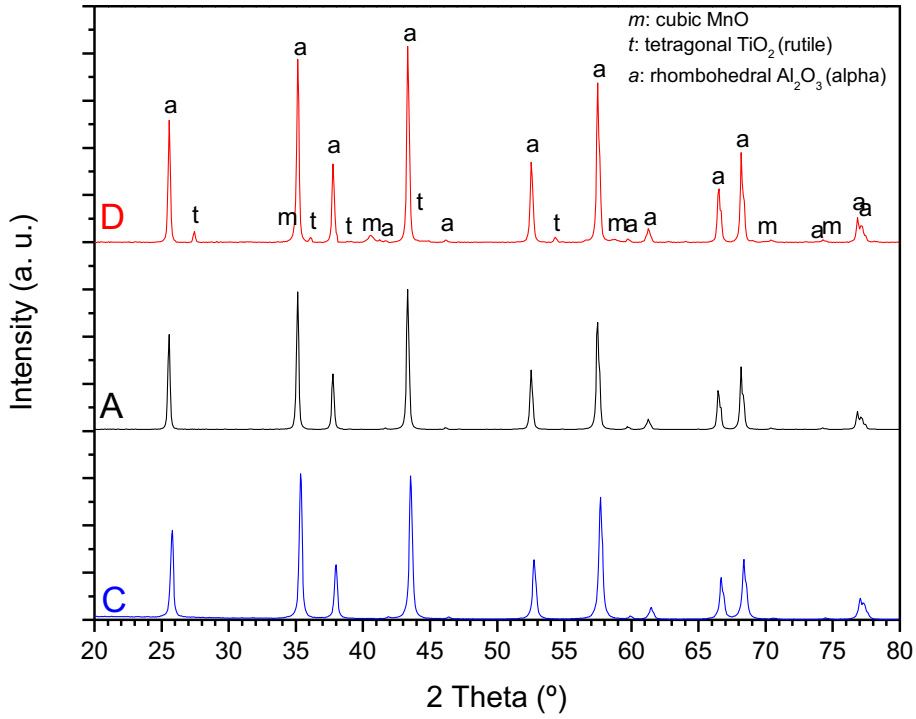

3.3.2 Slurries stabilization and rheology

Figure 30 presents the zeta potential variation as the function of pH for each powder, in suspensions with and without 1 wt% (referred to solids) of dispersant. Samples without dispersant presented isoelectric point 6.8 for A and 5.6 for D, indicating that the addition of MnO and TiO_2 as dopants slightly reduces the IEP of fine alumina suspension. The coarse alumina (C) presented IEP equal to 7.9. Therefore, the dispersant ensured the stability of the slurries since its addition shifted the alumina IEP to the pH range of 2 for A and D, and 4.3 for C. The addition of MnO and TiO_2 as dopants produced no significant difference in the zeta potential curve of the fine alumina suspension containing the dispersant. As reported in the literature, the IEP of pure alumina ranges from 8 to 9.3, and that of manganese and titanium oxide, from 5.4 to 5.9, depending on particle synthesis and purity[134]. Thus, in the present case, the IEP of Al_2O_3 was moved to the acidic range, such as those of MnO and TiO_2. The reason for this is linked to the good adsorption of the polyelectrolyte dispersant (ammonium polymethacrylate) on ceramic particles that avoids particles contact, modifying the double electric layer and ensuring their repulsion[135]. In this way, at neutral and basic pH values (7 and over), all oxides are negatively charged at the surface with zeta potential values lower than -40 mV, so that the particles remain dispersed[50, 136]. The final tape casting slurries have been adjusted to

pH values of 9.1, 9.1, and 8.9, for A, D, and C slurries, respectively. Thus, all of them were in the range of stability.

Figure 30 – Zeta potential vs. pH of oxide powders in aqueous suspensions without (dashed) and with (straight) the addition of 1 wt% dispersant referred to powder content. Suspensions containing dispersant are marked with (d) in the graphic's legend. A – fine alumina, C – coarse alumina, D – doped fine alumina.

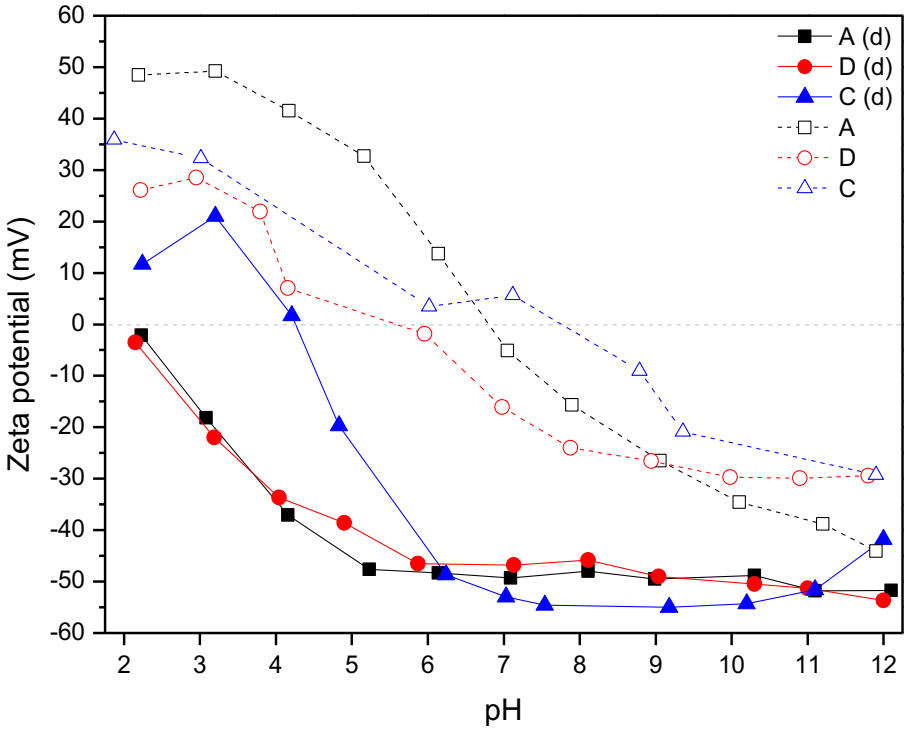

Figure 31 presents the rheological behavior of the ceramic slurries fitted by Herschel-Bulkley's model. Samples presented a shear-thinning behavior, as expected and required for tape casting slurries. The higher thixotropy corresponding to the hysteresis loop in the shear stress versus shear rate graph is most likely a consequence of the higher amount of organics. The organic additives at rest state increase considerably the viscosity. When the shear stress increases, the organic structure is destroyed, the entrapped liquid within is released, and the viscosity is reduced[53]. For all samples, at the same shear rate, shear stress is higher when the rate is increasing, compared to the decreasing rate curve. However, viscosity is lower when increasing the shear rate curve. At a shear rate of 100 s^{-1}, the mean values of viscosity are 1.89, 2.43, and 1.41 Pa·s for A, D, and C, respectively. Even using the same solid content (21 vol%) D's viscosity is higher than A ones, due to its higher density. The coarse alumina even added with 25 vol%, presented the lower values of viscosity, due to its higher average particle size compared to A and D.

Figure 31 – Rheological behavior of slurries used for processing tapes at varying shear rates. Arrows indicate the direction of curves, according to shear rate variation. A – fine alumina, C – coarse alumina, D – doped fine alumina.

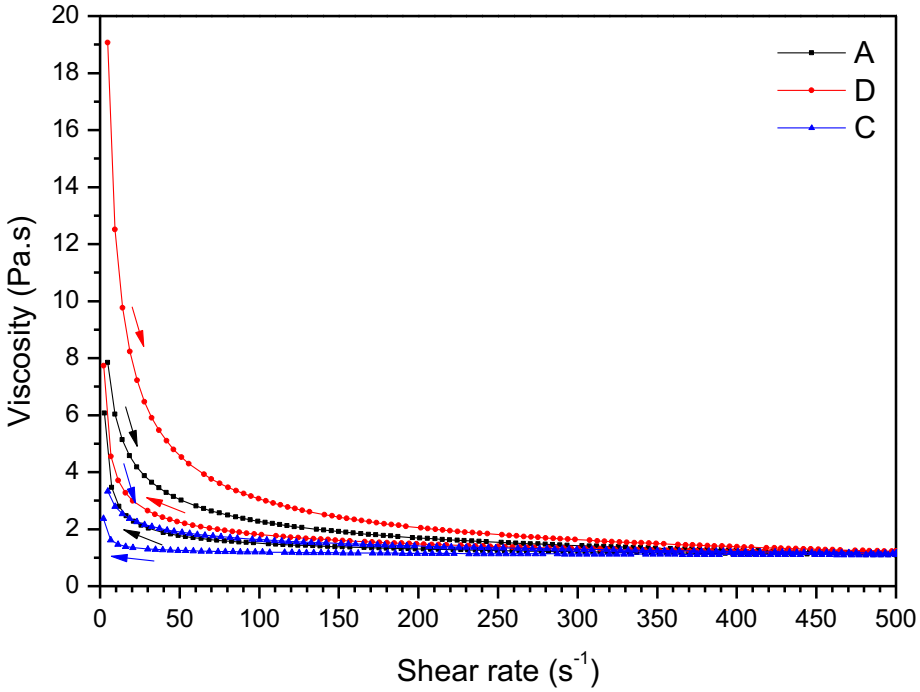

3.3.3 Characterization of green tapes and sintering behavior

Green cast tapes presented flexibility and easy handling after drying, with no visible defects like cracks and bubbles (Figure 32). The thickness varied in the range of 100 to 145 µm. Figure 33 shows the surface micrographs of A, C, and D tapes, as analyzed by scanning electron microscopy (SEM). Pores can be observed at both top and bottom surfaces. However, the bottom surfaces (smooth), which were in contact with the carrier, seem to be visually less porous than their respective top surfaces (rough). This gradient is caused by the evaporation of water and its elimination through the surface in contact with air. Furthermore, the binder takes more time to consolidate by coalescence and, due to this, clusters of the binder are formed. They migrate in the same direction of the water (from the bottom to the top) during drying and form groups on the top surface[137]. As a result, a porous structure is formed.

Figure 32 – Picture of processed green tapes. A – fine alumina, C – coarse alumina, D – doped fine alumina.

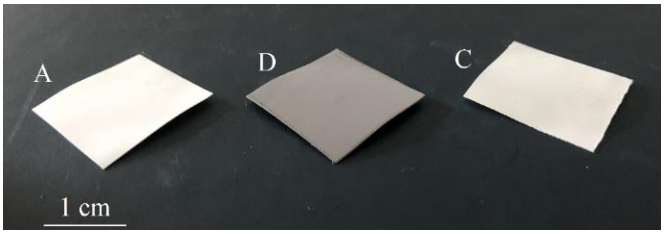

Figure 33 – SEM micrographs of top and bottom Surface of green, dried tapes. A – fine alumina, C – coarse alumina, D – doped fine alumina.

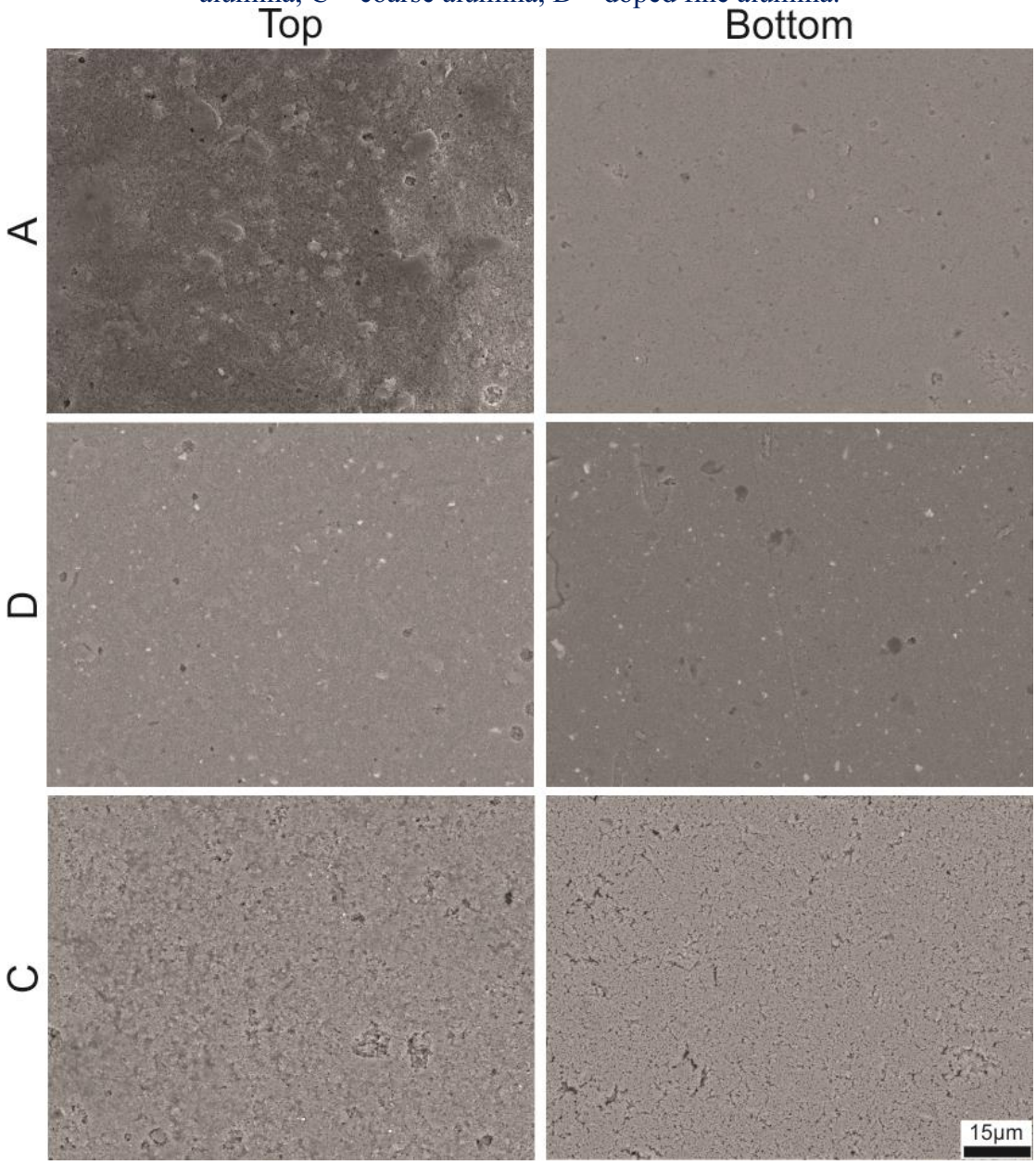

Figure 34 shows the thermal analyses (TG/DSC) of a fine alumina tape, which allows understanding the burnout of organics and optimize the sintering curves. Mass starts to decrease at ~215 °C and stays constant at ~530 °C, due to the elimination of

residual water and after to the burn out of volatile organics. The sample presented a final mass loss of ~15%. Exothermic peaks are observed at 267.6, 357.2, and 500.5 °C, due to the combustion of organic additives with increasing molecular chain length.

Figure 34 – TG/DSC thermal analyses of a single fine alumina tape (A).

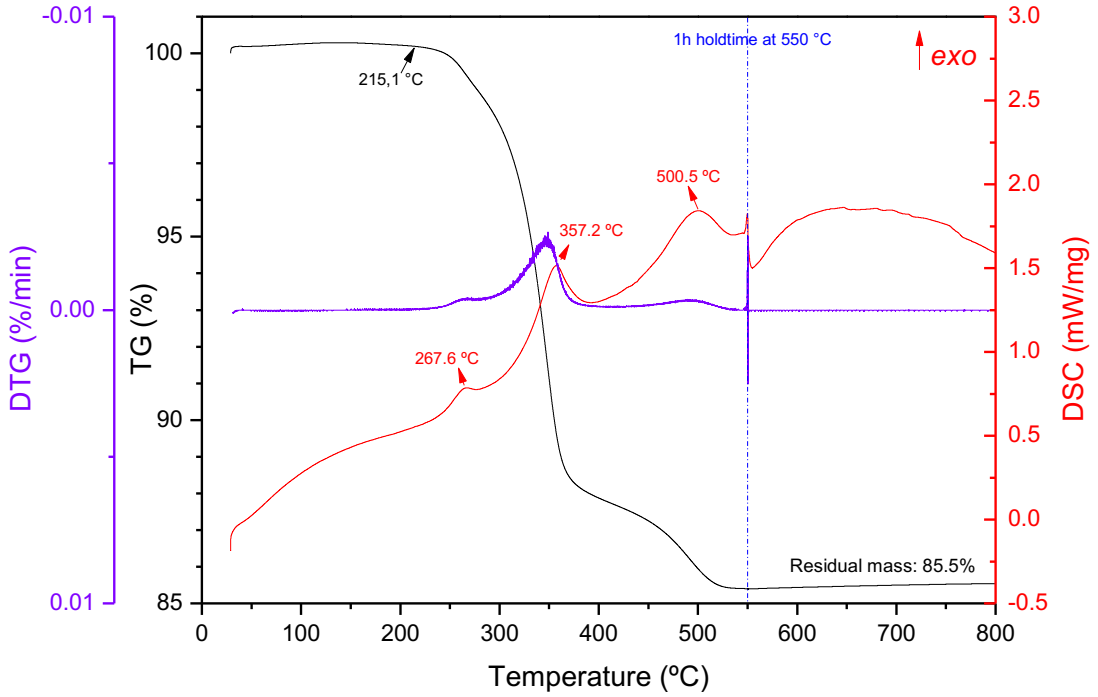

Figure 35 shows the linear shrinkage of tapes evaluated by dilatometry. From room temperature up to 385 °C, the samples presented a little shrinkage due to the removal of residual water, being almost constant after that. Before sintering, a slight expansion is observed until the starting of sintering as a result of organics removal. Samples present different temperatures to start sintering, with A starting to densify at 1000 °C, sample D at 910 °C and sample C at 1130 °C. As expected, the use of dopants increased sinterability and reduced the start-sintering temperature of pure alumina, a fact attributed to grain boundaries and volume diffusions, and the presence of anion and cation vacancies[21]. As also expected, the coarser powder, CT 3000 SG, presented the lowest sintering and shrinkage rate due to the lower surface area and driving force compared to finer powders[14, 15]. These two cited topics will be better approached and explained in the next chapters. The calculated coefficients of thermal expansion, in the range 200 to 1000 °C, of samples sintered at 1200 °C are 11.8×10^{-6}/K for A and 11.4×10^{-6}/K for D. The CTE for samples sintered at 1350 °C are 12.3×10^{-6}/K for A and 12.7×10^{-6}/K for C.

Figure 35 – Dilatometry performed in tapes submitted to sintering. Tapes of undoped and doped fine alumina (A and D) sintered at 1200 °C, as a cyan dashed line. Tapes of fine and coarse alumina (A, and C) sintered at 1350 °C, as a green dashed line.

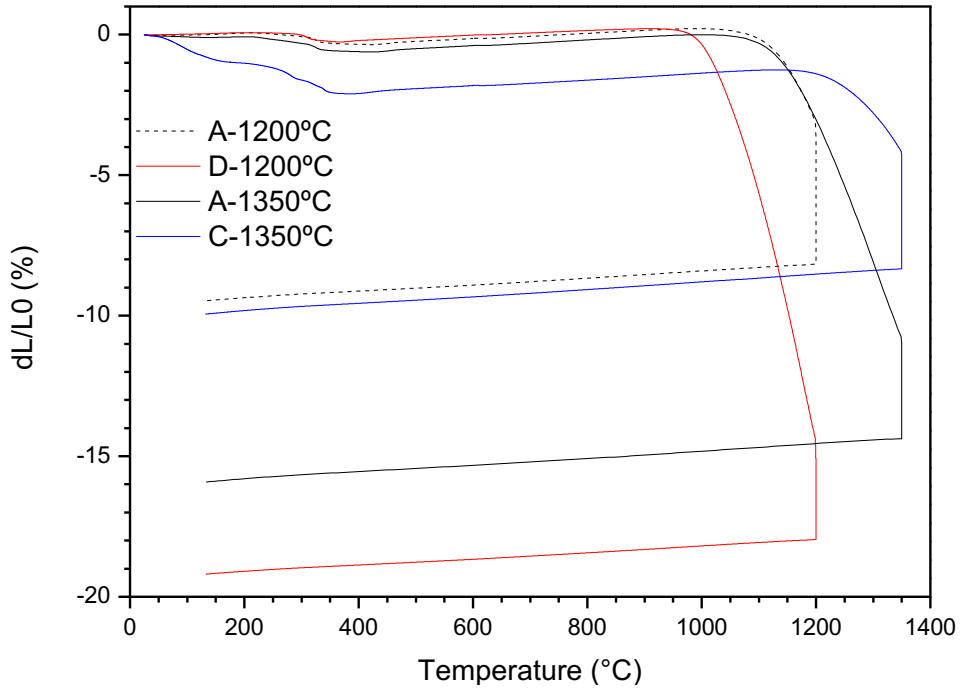

Figure 36 shows the X-ray diffraction spectra of sintered tapes. In all samples, alumina is presented as the rhombohedral crystalline structure, α-alumina. In the doped alumina sample, there is evidence of the presence of titanium dioxide (rutile) and the formation of manganese titanate. $MnTiO_3$ is reported to occur in the MnO-TiO_2 phase diagram for the mole ratio from 0.33 to 0.5 up to ~1385 °C[138]. For D, this value is 0.39. The presence of MnTiO3 is in agreement with the EDS-STEM mapping analysis (Figure 37). The micrograph shows the presence of closed intergranular pores (black points) located in the triple points of alumina grains (dark gray). The dopants (light gray) settled mainly in the triple points and grain boundaries of alumina grains, indicating that the dopant level exceeds essentially the amount of dopants, which form a grain boundary film. Additionally, dopants are also located as intragranular inclusions within alumina grains. EDS mapping evidenced the high concentration of Mn and Ti in these regions (light gray points). This behavior indicates that these segregations did not pin the grain boundaries during grain coarsening.

Figure 36 – X-ray diffraction spectra of sintered samples. A – fine alumina, C – coarse alumina, D – doped fine alumina. Crystallographic identification according to PDF-2 ICDD database.

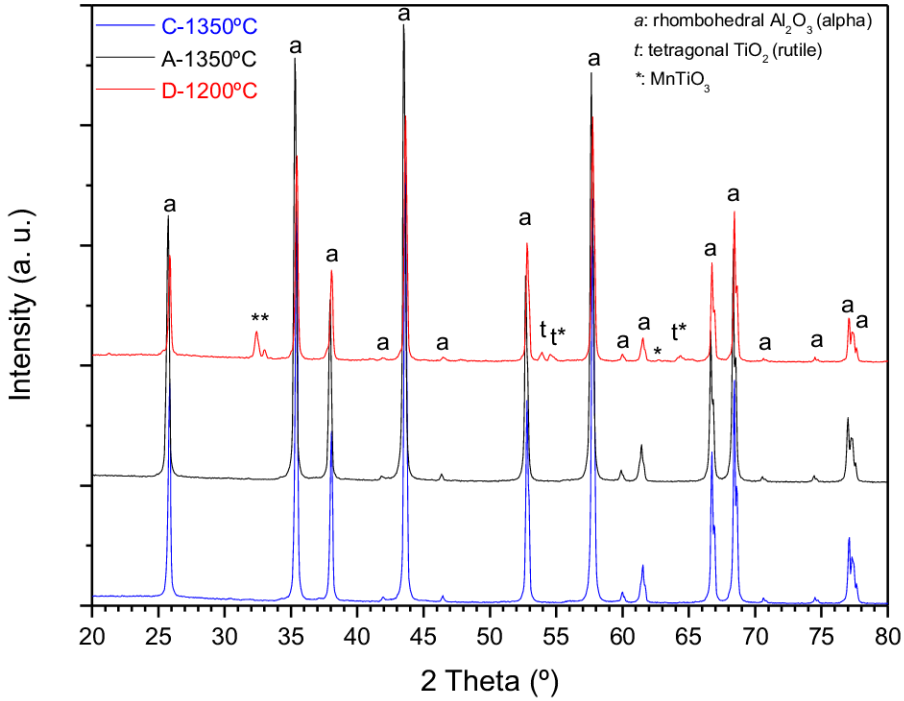

Figure 37 – STEM micrograph of doped alumina layer sintered at 1200 °C. Alumina grains are in gray, dopants are in light gray and are pores in black. Below is the EDS mapping analysis of the blue square region of the micrograph. The colors blue, red, yellow, and purple refer to aluminum, oxygen, manganese, and titanium, respectively.

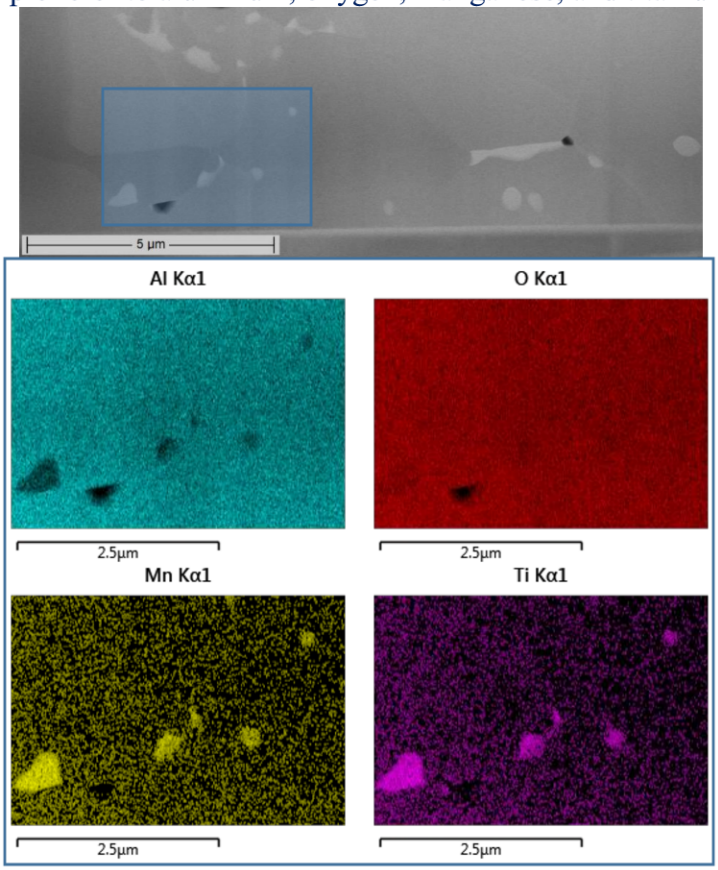

3.4 Conclusions

Thin ceramic samples were successfully shaped by tape casting with undoped and doped alumina powders. Raw powders presented unimodal distributions, with irregular faceted shapes for alumina powders. XRD analyses of raw powders presented α-alumina, titania as rutile, and MnO. The use of dispersant assisted the stabilization of particles and decreased the pH value at the isoelectric point. Rheological analyses showed shear-thinning and thixotropic behavior for slurries. Tapes presented different morphologies on top and bottom surfaces, with higher regularity in the last ones. Thermogravimetric and dilatometric analyses showed a first weight loss and shrinkage starting at ~215 °C due to the removal of residual water and small-chain organic additives. A larger weight loss and a small expansion were observed in the range of 300 to 525 °C due to the burnout of long-chain organics. Doping fine alumina with MnO and TiO_2 reduced the starting sintering temperature to 910 °C when compared to undoped fine (1000 °C) or coarse alumina (1130 °C). XRD analyses detected α-alumina in both layers, as well as titania as rutile, and evidence of $MnTiO_3$ formation in d-Al_2O_3. Also, EDS/STEM showed the presence of intergranular closed pores and dopants settled in intergranular and intragranular positions, corroborating with the fact of Ti and Mn to be diffused through the alumina.

Chapter 4 – Dopant diffusion at the interface of doped alumina-alumina layers in sintered laminates [2]

4.1 Introduction

Alumina is a ceramic oxide with excellent properties, such as high strength, hardness, corrosion, chemical stability, and wear resistance[7, 8, 108]. High purity alumina bodies usually require high sintering temperatures – usually over 1400 °C – to reach relative densities close to 100%[16]. Additives – such as TiO_2, MnO, MgO, Cu_2O, ZrO_2, Y_2O_3, and Li_2O_3 – have been employed to increase alumina sinterability and achieve full density while controlling grain growth[21, 22]. Sintering aids can enhance sintering due to the formation of lattice defects, solid solutions, or liquid phases. Generally, there is an optimal amount of additives, which varies with the sintering temperature to achieve higher densification[23, 24].

TiO_2 is a crystal growth promoter and sintering aid in alumina, where small additions (e.g. 0.2 mol%) can enhance effectiveness diffusion[25]. Cutler *et al.*[26] verified that MnO together with TiO_2 is more effective in lowering alumina sintering temperature than using these additives alone. They also reported the evidence of a liquid phase formation which accelerates the densification. However, this theory was further invalidated the following year by Jones and co-authors, where they proved that the sintering process occurs due to the production of anion and cation vacancies in the alumina lattice which increase the rate of diffusion and sintering.

McKee Jr. and Aleshin[139] also verified the effectiveness of titanium dioxide to enhance densification and concluded that the action occurs at grain boundaries. Keski and Cutler[28] used only MnO as an additive to increase the sintering rate. With the addition of 0.3% of MnO sintering occurs by the volume-diffusion mechanism. When MnO was added less than this amount, a tendency of grain-boundary kinetics is observed.

Bagley and co-authors related the mechanisms of sintering to alumina particle size. For particle sizes of less than 1 μm was observed a gradual change from grain-boundary to volume diffusion with increased titania content. For particle sizes between 1 to 2 μm, sintering occurred by a combination of both mechanisms. For coarser alumina, higher than 2 μm, the sintering mechanism observed was grain-boundaries regardless of titania content. The diffusion changes constantly with the addition of TiO_2 until a

[2]Published in the *Int J Ceramic Eng Sci.* https://doi.org/10.1002/ces2.10090.

maximum rate and tends to decrease after. The author linked this less effective diffusion to a formation of a second phase which is expected to inhibit sintering. Toy *et al.*[32] verified for alumina doped with MnO no secondary phase formation and deduced that a solid solution with Al_2O_3 is formed.

In this chapter, the diffusion of dopants, TiO_2 and MnO, in the interface of the laminate doped alumina-alumina sintered at different temperatures was investigated in detail.

4.2 Material and methods

Aqueous slurries of high purity alumina Taimicron TM-DAR (d_{50} = 150 nm, Taimei Chemicals, Japan) and a mixed powder with a final average particle size of 220 nm of the same alumina doped with 1.68 wt% of titanium dioxide (Kemira, Finland) and 2.32 wt% of manganese oxide (Sigma-Aldrich, Germany) were produced with 21 vol% of solids via ball milling mixing. Additionally, 30 wt% of binder Mowilith LDM 6138 (Celanese, USA), 2 wt% of Darvan C-N (Vanderbilt Minerals, USA), 1.5 wt% of non-ionic surfactant NINOL PK-80 BR (Stepan, USA), and 1 wt% of antifoamer Antifoam Y-30 (Sigma-Aldrich, Germany) referred to solids content were added. Slurries were cast in a tape caster machine CC-1200 (Tape Casting Warehouse, USA) and left to dry for 24 h at room temperature.

Ceramic laminates (15×15 mm²) composed of outer pure alumina layers (Al_2O_3) and an intermediate layer of doped alumina (d-Al_2O_3) were produced by uniaxial pressing at 10 kN and 65 °C for 5 min and. Samples were first debinded at 600 °C for 1 h with a heating rate of 0.3 °C/min. They were later sintered in air at 1100, 1150, 1200, and 1250 °C for 2 h, with heating and cooling rates of 5 and 10 °C/min respectively. Samples were embedded with an acrylic resin (Scandiquick, Scan-Dia, Germany), ground with silicon carbide papers, and polished with diamond suspensions (Struers, USA) with the last grains size of 0.25 µm. After nanoindentation tests, the samples were removed from the resin and submitted to thermal etching at 90% of the sintering temperature for 30 min to reveal the grains. The microstructure was analyzed by optical (OM, BX51, Olympus, Germany) and scanning electron (Supra VP 55, Zeiss, Germany) microscopy. The line-intercept method (LIM) was applied to measure grain size (at least 200 grains per sample) using software for image analysis (Lince 2.4.2e, Ceramics Group, TU Darmstadt, Germany).

Hardness and Young's modulus were measured at pure and doped layers, and the diffusion region between them using a nanoindenter (G200, Agilent Technologies, USA) equipped with a Berkovich tip. Before tests performing, samples were embedded in acrylic resin, ground with silicon carbide grinding papers, and polished with diamond suspensions until 1 μm roughness. The continuous stiffness measurement method (CSM) was used, with a constant strain target of 0.05 s^{-1}, a harmonic displacement target of 2 nm, and a harmonic frequency of 45 Hz. The maximum depth was set to 2000 nm, with a holding time of 10 s before unloading. At least 10 measurements were done for each region in each sample.

To deeply investigate the region of diffusion of dopants, six batches of 19 indentations were done in the 1200 °C sintered sample along with the interface, coming from doped alumina layer to pure alumina layer, to investigate E and H profile along the diffusion region. Tests were done with an advance of 7.5 μm and lateral displacement of 60 μm related to the last indentation. Additionally, the grain size profile was also measured in the same region, starting from the doped alumina layer to the pure alumina layer. Measurements were done with an advance of 5 μm from the last point, in a total of 18 points. For each point, a straight line was drawn parallel to the interface and at least 30 grains per line were measured. The procedure was repeated two times.

4.3 Results and discussion

Figure 38 presents OM and SEM images for sintered samples exhibiting a light brownish region in the Al_2O_3 layer close to the d-Al_2O_3 layer. The higher the sintering temperature, the more accentuated is this effect and thicker is the region. This color change is the first hint for the diffusion of the dopants. Thereby, the degree of diffusion of dopants depends on the temperature of sintering. Dopants have a threshold distance from the interface to diffuse, resulting in a diffusion region with regular thickness. The optically estimated thickness for each sample was 17 ± 2 μm for 1100 °C, 25 ± 3 μm for 1150 °C, 51 ± 7 μm for 1200 °C and 62 ± 10 μm for 1250 °C.

Figure 38 – Micrographs of sintered samples. OM images (on the left column) present the Al_2O_3 layer in white-yellowish and d-Al_2O_3 layer in brown-reddish. In SEM images (on the right column), Al_2O_3 layers are dark grey, while d-Al_2O_3 layers are light gray. Yellow lines indicate the position of the interfaces in each sample. In the OM images, the light blue line indicates the optically estimated distance of diffused dopants.

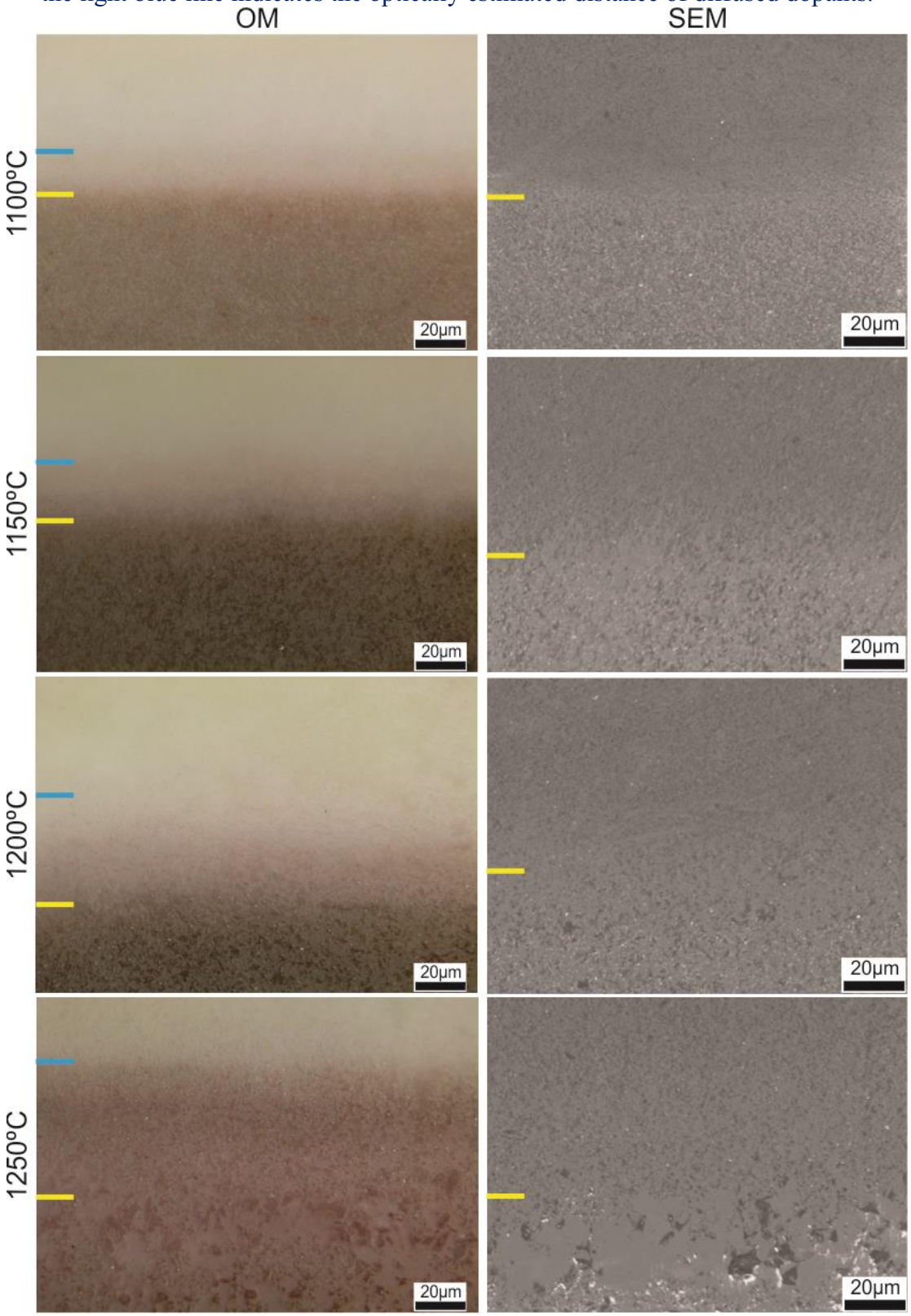

Figure 39 presents the average grain size (AGS) for each layer at the different sintering temperatures. The SEM images show that the diffusion of dopants modifies the microstructure of the pure alumina layer, e.g. larger grains in the diffusion zone. Doped alumina presented larger grains with increasing sintering temperature. Significant grain coarsening is observed at 1250 °C for the doped alumina layer. On the other hand, pure alumina presents smaller grains when compared to doped alumina, with no significant variation of the average grain size at the respective sintering temperatures. It is useful at this point to mention what is known about bulk and grain-boundary diffusion in alumina. The literature on this subject was reviewed recently by Heuer[140]. A clear trend is observed in an Arrhenius representation showing the bulk diffusivity data for oxygen and aluminum diffusion in Al_2O_3 in a temperature range of 1200 to 1800 °C. Obviously, the higher the temperature the higher the bulk diffusion, but remarkable diffusion data were observed in the range of 1200-1400 °C[40, 141].

Figure 39 – Average grain size measured in pure and doped alumina layers at the different sintering temperatures.

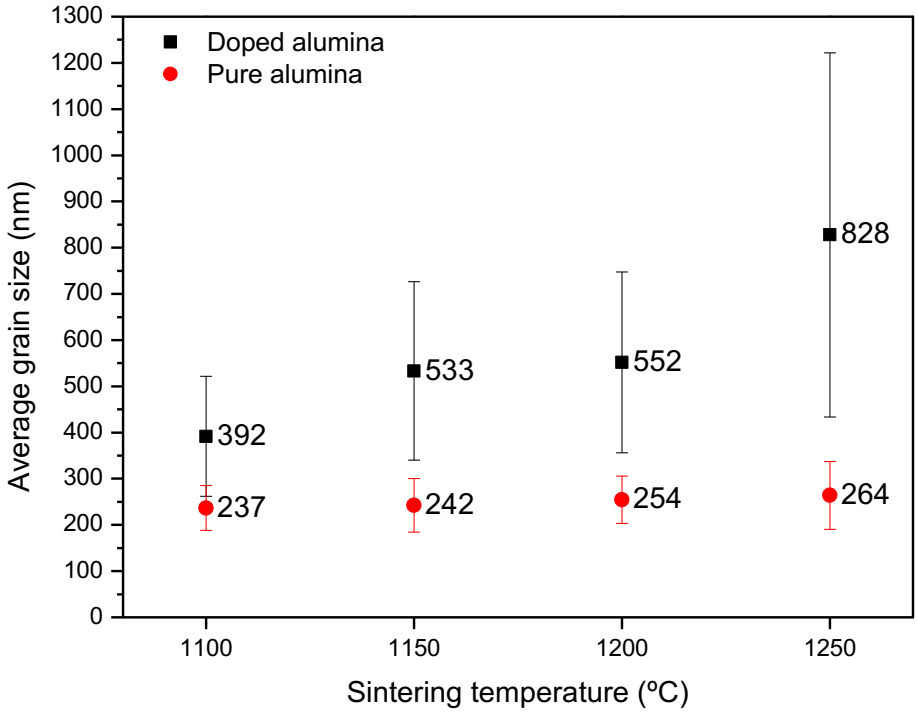

Figure 40 shows the typical load-displacement nanoindentation curves obtained for each sample in the three tested regions. Table 5 complements the figure and presents the average maximum loads achieved during tests. It is observed that the higher maximum loads for each sintering temperature are attributed to d-Al_2O_3 layers, while the lower ones are for Al_2O_3 only. Interfaces always show a maximum load between values of pure and doped alumina. In most cases, the load reached the preset maximum value, 2000 mN.

Therefore, a plateau is observed after curves reach the maximum load, indicating that displacement still occurs during the holding period, which is most likely caused by creeping deformation[142]. In general, maximum loads are supposed to increase with increasing sintering temperatures, which is related to the densification of layers. Still, the maximum load value at 1200 and 1250 °C, respectively, for doped alumina layers exhibit little gain.

Figure 40 – Typical load-displacement curves of each sample. Black, red and blue curves represent pure alumina, interface, and doped alumina, respectively.

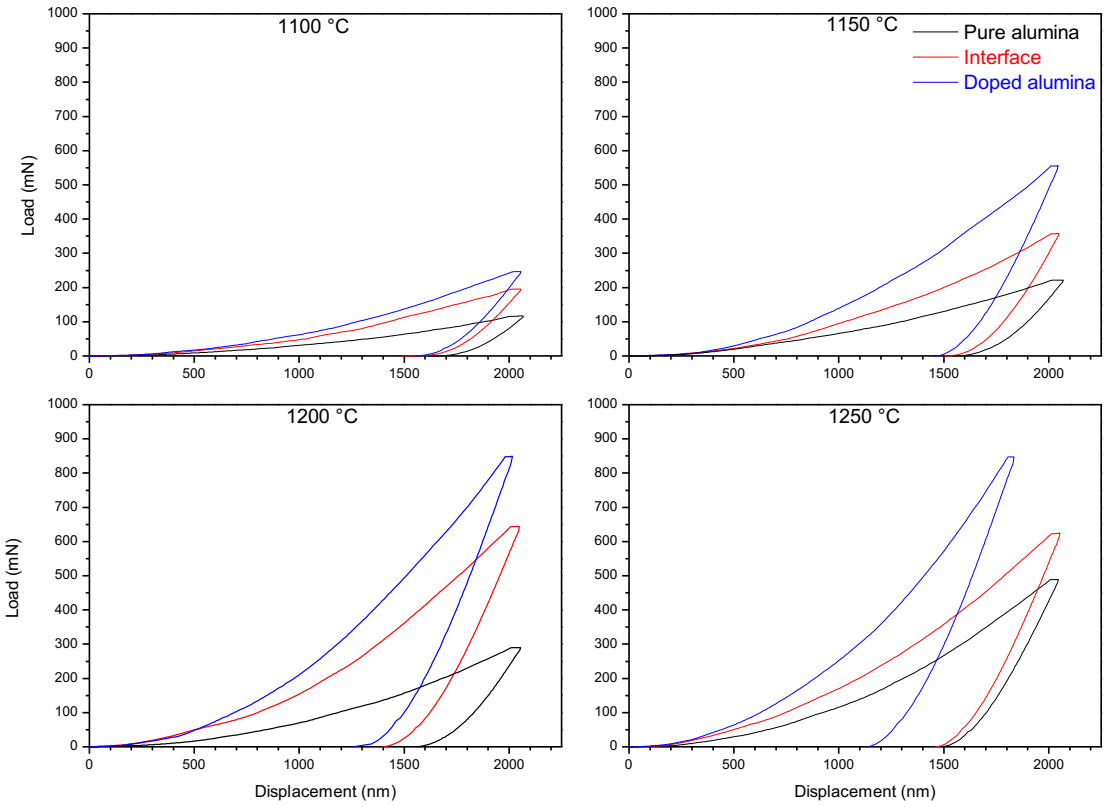

Table 5 – Average maximum loads for pure and doped alumina, and interface regions at different sintering temperatures.

Sintering temperature (°C)	Load (mN)		
	Al_2O_3	Interface	d-Al_2O_3
1100	120.3 ± 7	202 ± 6	253 ± 10
1150	214.1 ± 15	361 ± 53	542 ± 33
1200	335.2 ± 28	639 ± 34	835 ± 21
1250	521.8 ± 29	576 ± 31	848 ± 1

Figure 41 and Table 6 presents the average Young's modulus (E) and hardness (H) obtained for each region at the different sintering temperatures. Again, an increase of these properties is observed with increasing sintering temperatures, which is related to

the higher degree of densification of samples. The interface of the sample sintered at 1200 and 1250 °C presented no significant changes in *E* and *H*.

Table 6 – Young's modulus and hardness for pure alumina, interface, and doped alumina regions, according to the sintering temperature.

Sintering temperature (°C)	Young's modulus (GPa)			Hardness (GPa)		
	Al_2O_3	Interface	d-Al_2O_3	Al_2O_3	Interface	d-Al_2O_3
1100	57 ± 3	83 ± 2	99 ± 4	1.5 ± 0.1	2.4 ± 0.1	3.2 ± 0.3
1150	83 ± 4	130 ± 1	171 ± 9	2.7 ± 0.3	4.6 ± 1.0	7.5 ± 0.7
1200	116 ± 7	195 ± 11	235 ± 12	4.5 ± 0.6	9.1 ± 0.9	12.7 ± 1.1
1250	159 ± 7	193 ± 8	283 ± 14	7.1 ± 0.6	9.2 ± 0.6	15.6 ± 1.9

Figure 41 – Young's modulus (on the left side, straight lines with filled points) and hardness (on the right side, dashed lines with open points) of Al_2O_3 layer, interface, and d-Al_2O_3 layer.

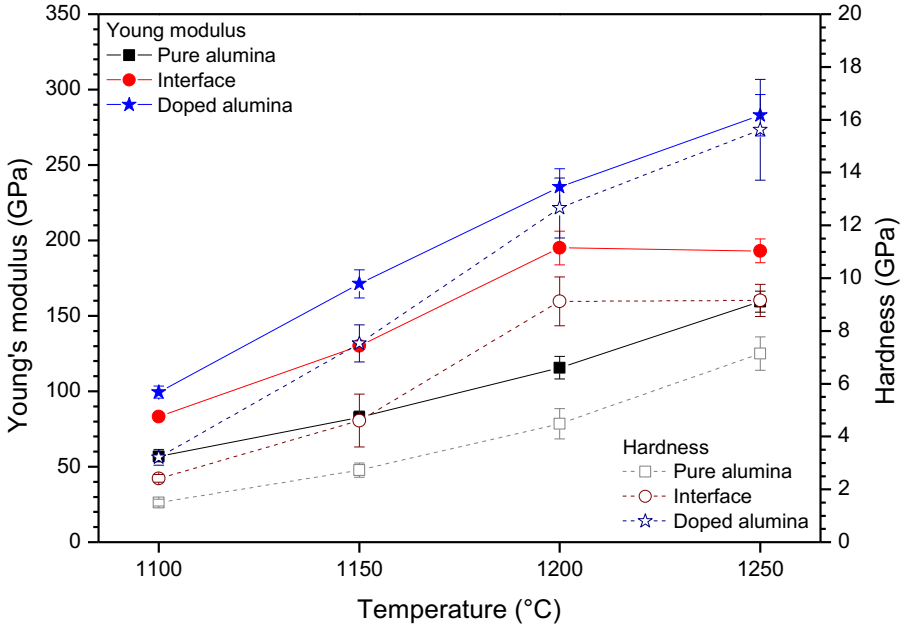

Figure 42 presents the nanoindentation results along the diffusion profile carried out for the sample sintered at 1200 °C. Along the region of diffusion, a gradual transition of Young's modulus and hardness values is observed. In the pure layer close to the interface, the concentration of diffused dopants in the alumina layer is highest and decreases further away from the interface resulting in respective gradients of the sintering potential. As well known, the porosity gradient caused thereby has a deleterious influence on Young's modulus and hardness. As the distance from the interface increases, the amount of dopants decreases until no diffusion occurs. Higher sintering temperatures provide more energy to the system. The higher the temperature, the further the distance the dopants travel, and consequently, the higher the thickness of the diffusion region. This also explains the intermediate values of *E* and *H* obtained for the interface in all sintering

temperatures, compared to the Al_2O_3 and d-Al_2O_3 layers. Moreover, there is also a gradual decrease in grain size from the interface towards the pure alumina (Figure 43). Since the dopants act as a sintering aid and crystal growth promoter, the higher amounts of dopants result in larger grain sizes, as observed in Figure 44.

Figure 42 – Young's modulus and hardness profile in the 1200 °C-sintered sample. The gray line and light gray zone represent, respectively, the average values and standard deviation for doped alumina reference. The pink line and light pink zone represent, respectively, the average values and standard deviation for pure alumina reference. The X-axis indicates the distance from the first point (point zero), which starts in the doped alumina layer and advances in the direction of the pure alumina layer.

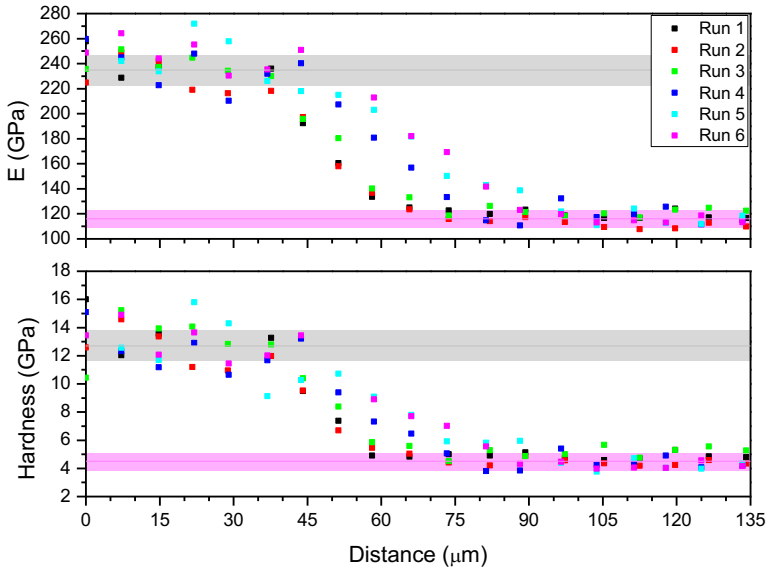

Figure 43 – Grain size profile in the sample sintered at 1200 °C. The gray line and light gray zone represent, respectively, the average values and standard deviation for doped alumina reference. The pink line and light pink zone represent, respectively, the average values and standard deviation for pure alumina reference. The X-axis indicates the distance from the first point (point zero), which starts in the doped alumina layer and advances in the direction of the pure alumina layer.

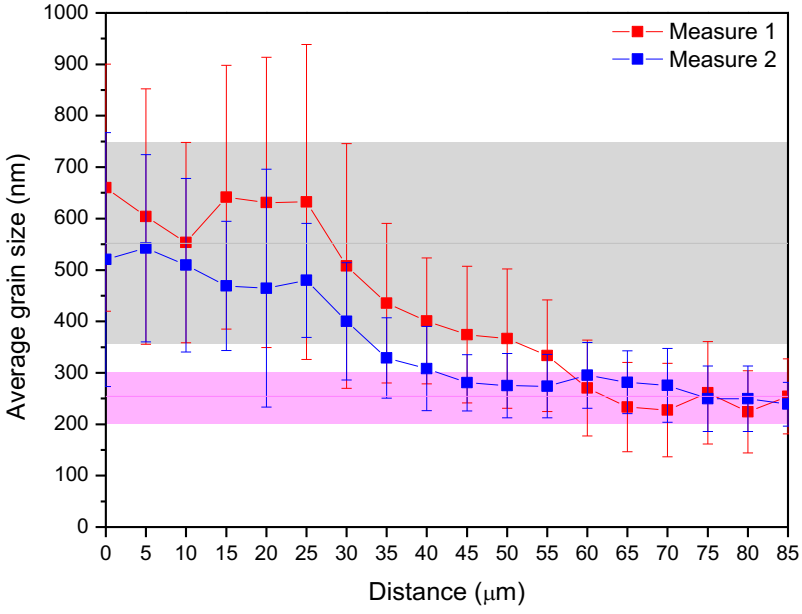

Figure 44 – SEM micrographs show the interface between doped and pure alumina for the sample sintered at 1200 °C (I), the yellow line indicates the interface position. Micrographs (II) and (III) show, in close, the middle of doped and pure alumina layers respectively.

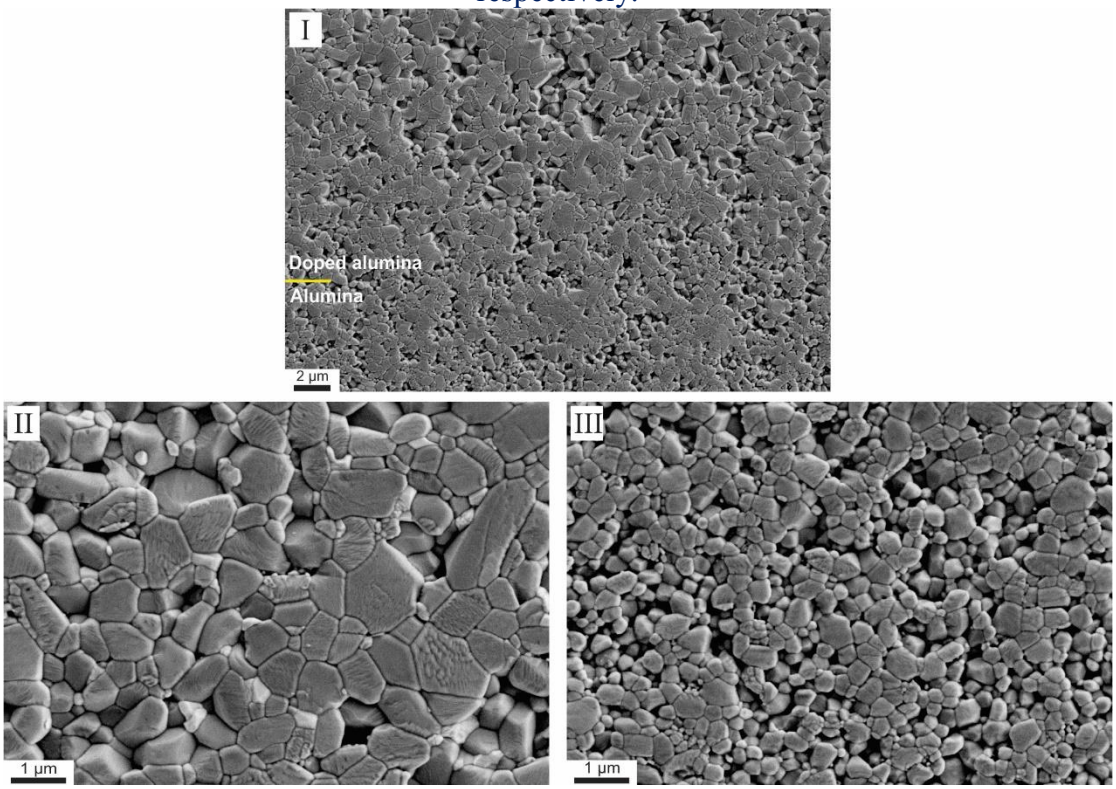

4.4 Conclusions

The diffusion of dopants in TiO_2-MnO-doped Al_2O_3/Al_2O_3 laminates was investigated using scanning electron microscopy, optical microscopy, EDS, and nanoindentation. Optical micrographs showed the presence of a light brownish region in pure alumina layers due to the presence of dopants that migrate from doped alumina layers. The diffusion region could be optically estimated and increased with increasing temperatures. The SEM images showed modifications on the microstructure of pure alumina due to the presence of dopants. The average grain size of d-Al_2O_3 is higher than those of Al_2O_3 at all sintering temperatures, with accentuated grain coarsening of the first after 1250 °C.

Higher values of maximum load, hardness, and Young's modulus were observed for d-Al_2O_3 layers, compared to Al_2O_3 layers. The dopants diffusion zone presented intermediate values to that observed for doped and pure alumina layers due to modifications in the microstructure caused by Ti and Mn. Furthermore, the values of *H* and *E* for these three different regions increase with the increase of sintering temperature.

According to the accurate analysis of the 1200 °C-sample diffusion zone, the highest concentration of dopants in the pure alumina layer is right after the interface and decreases gradually for longer distances until no significant dopant effects are detectable.

Chapter 5 – Microstructure and mechanical behavior of TiO_2-MnO doped alumina/alumina laminates[3]

5.1 Introduction

Since Clegg *et al.*[72] were successful in producing weak interfaces in laminated ceramic composites to obtain a non-catastrophic failure, several studies were done presenting ceramics with laminar structures as an effective alternative to overcome the typical brittleness of monolithic ceramics, to avoid catastrophic failure, to modify the crack path and to increase fracture toughness. One approach widely used for ceramic laminates is to generate compressive residual stresses in layers due to different coefficients of thermal expansion, considering interfaces with strong adhesion. The idea is to achieve high levels of compressive stresses in these layers to control or oppose crack propagation, activating toughening mechanisms as crack arresting, crack bifurcation, and microcracking. Thus, it is possible for laminates to enhance fracture toughness and to absorb more energy during failure, compared to reference monolithic ceramics[55, 70, 78, 108, 133, 143–147].

Another way to enhance toughness in laminates is to produce weak interfaces or layers to cause crack deflection. This behavior strongly depends on the fracture energy and Young's modulus of weak and strong layers of the composite. The volume fraction of pores and the pore interaction have an important contribution to ensure that crack continues propagating in the weak layer or interface. The porosity in these materials is normally produced by introducing fugitive pore former agents, such as starch, graphite, or polymers[73, 77, 83, 86, 148–150]. On the other hand, tailoring the sinterability of a ceramic laminate in both strong and weak layers is possible by using starting powders with different particle sizes or dopants to reduce sintering temperatures[151]. The sintering driving force is inversely proportional to the particle size. The finer the particles, the faster the sintering rate. Thus, sintering for smaller particles occurs at lower temperatures, due to the smaller diffusion distances. There is also a relationship with melting temperature, once it decreases with the lower particle sizes[14, 15].

The use of sintering aids as titanium and manganese oxides has been proved effective to lower alumina sintering temperature and promoting crystal growth. Winkler

[3]Published in *J Am Ceram Soc*. https://doi.org/10.1111/jace.17490

et al.[25] have used TiO_2 as a sintering aid and grain growth promoter for alumina. Jones, Cutler, and co-authors[26, 27] added a total of 4 wt% manganese and titanium oxides or copper and titanium oxides, and the result was an effective reduction in the sintering temperature to the range of 1300 °C to 1400 °C. Kostić *et al.*[31] achieved ~95% of RD after sintering alumina at 1300 °C with 5 wt% of a TiO_2/MnO mix, contrasting with 58% of RD obtained for pure alumina submitted to the same heat treatment. Xue and Chen[24] used a colloidal process for alumina with 0.9 mol% CuO + 0.9 mol% TiO_2 + 0.1 mol% MgO + 0.1 mol% B_2O_3. As a result, they sintered alumina at 1070 °C in 1 h and obtained 99.3% of RD. Sathiyakumar and Gnanam[34] also used colloidal processing with MnO and TiO_2 as sintering additives. The authors reduced the sintering temperature from 1550 °C to 1200-1250 °C, obtaining 99.2-99.6% of RD.

One of the most used methods to obtain reliable results of fracture toughness as a function of crack length in ceramics composites is the SEVNB technique[111, 152]. A device developed by Jelitto *et al.* [115] uses the SEVNB method in a very stiff apparatus that allows a stable crack growth. Performing several loading-unloading cycles, many values of fracture toughness at different crack lengths can be obtained with one single specimen[115, 118, 119, 146].

In this chapter, alumina-based laminates were produced alternating dense and weak layers design based on the different degrees of densification. Non-doped alumina and coarse alumina are supposed to produce weaker layers compared to TiO_2-MnO doped and fine alumina dense layers, respectively, enhancing fracture toughness and creating a particular R-curve behavior. Microstructure, mechanical behavior, and crack propagation were characterized and correlated with the laminate configurations.

5.2 Materials and methods

The lamination of samples was performed in a homemade warm press at 10 kN and 65 °C for 5 min. Green laminates of monolithic pure alumina and doped alumina have been manufactured as reference materials, and four different configurations of composites were produced (see Figure 45 and Table 7). The first group of the composites is composed of D dense layers alternated with A weak layers sintered in air at 1200 °C, with three different layer thickness ratios (D:A), 4:1, 1:1, and 1:2. The objective is to analyze the use of dopants to obtain different sintering degrees, together with the influence of weak

layer thickness in the composites. Following the idea, the fourth type of composite was produced with dense A and weak C layers but based on different starting particle sizes instead of using dopants. This material was sintered in air at 1350 °C, with a layer thickness ratio (A:C) of 4:1. It is assumed that an elastic mismatch between the layers should be created due to the different densities (originated by two cited different approaches, doping and particle size) and positively modify the fracture behavior of materials, which would be also influenced by the thickness of layers. Green tapes were laminated to achieve the approximate dimensions of 3.5×15×50 mm³ after sintering.

Figure 45 – Illustration of the samples produced: A1200/1350; C1350; D1200; DA-17L; DA-11L; DA-3L and AC-17L. White is pure fine alumina, brown is doped alumina and gray is pure coarse alumina.

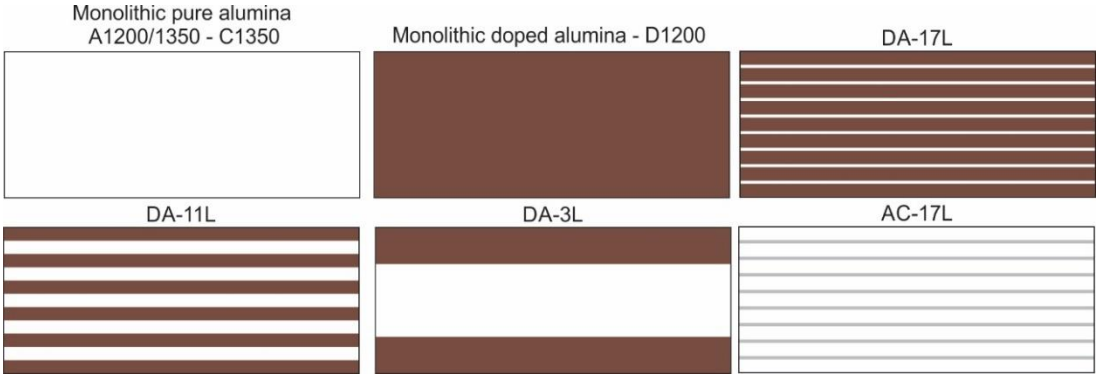

Table 7 – Characteristics of monolithic reference and composites materials.

Sample name	Material	Nº of tapes (per layer)	Nº of layers	Layer thickness ratio (dense:porous)	Sintering temperature (°C)
A1200	Monolithic pure alumina	A: 44	-	-	1200
A1350	Monolithic pure alumina	A: 44	-	-	1350
D1200	Monolithic doped alumina	D: 44	-	-	1200
C1350	Monolithic pure alumina	C: 44	-	-	1350
DA-17L	Doped and fine pure alumina layers	D: 4 A: 1	D: 9 A: 8	4:1	1200
DA-11L	Doped and fine pure alumina layers	D: 4 A: 4	D: 6 A: 5	1:1	1200
DA-3L	Doped and fine pure alumina layers	D: 11 A: 22	D: 2 A: 1	1:2	1200
AC-17L	Fine and coarse pure alumina layers	A: 4 C: 1	A: 9 C: 8	4:1	1350

Sintering curves (Figure 46) were adjusted based on the thermal analyses conducted in Chapter 3. The burn out of organics was performed in muffle (M110, Heraeus Holding GmbH, Germany) with a heating rate of 0.3 °C/min until 550 °C and a holding time of 1 h. The temperature was then elevated with 5 °C/min to 800 °C for pre-

sintering and ensure furnace change safety of samples. Samples were moved to a high-temperature furnace (HT 04, Nabertherm GmbH, Germany) for sintering. Samples of A1200, D1200, DA-17L, DA-11L, and DA-3L were sintered in air at 1200 °C, while A1350 and AC-17L were sintered in air as well at 1350 °C. In both heat treatments, a heating rate of 5 °C/min and a holding time of 2 h was used. The cooling rate was set to 10 °C/min.

Figure 46 – Two heat treatments used to sinter the samples of this work. The green curve refers to the debinding step, applied previously to the samples' sintering. Blue and red curves refer to the 1200 °C and 1350 °C sintering, respectively.

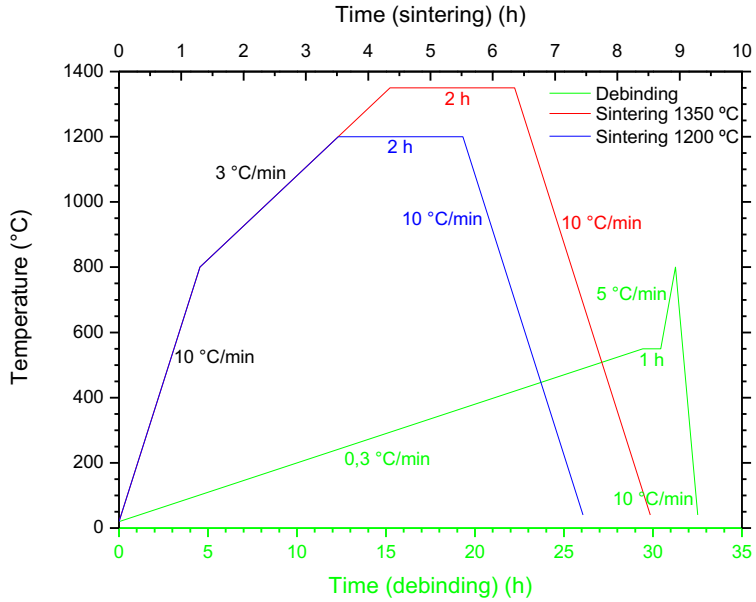

The density of sintered monolithic references was measured with the Archimedes method, 5 samples per batch, in an analytical balance (ABT 100-5NM, Kern, Germany). A nanoindenter (G200, Agilent Technologies, USA) equipped with a Berkovich tip was used to measure the elastic modulus and hardness of monolithic sintered samples. At least 25 indentations were performed for each measurement by using the CSM technique[153]. Microstructure and fracture analyses were conducted using an optical microscope (BX51, Olympus, Germany) and a scanning electron microscope (Supra VP 55, Zeiss, Germany). The microstructure was revealed using thermal etching at 90% of the sintering temperature for 30 min. The grain size was measured using the line-intercept method with the help of image analysis software (Lince 2.4.2e, Ceramics Group, TU Darmstadt, Germany) using 300 grains measures per sample.

Four-point bending tests were performed using as-sintered prismatic bars (3.5×2.5×25 mm³) cut from the laminates using a universal test machine (Series 1605B, ATS, USA). Outer and inner spans had a distance of 20 mm and 10 mm, respectively. A loading speed of 1 mm/min was applied. At least 10 samples of each material were tested.

Weibull's statistical analysis was applied to the results to compare the samples among themselves.

For the R-Curve tests, prismatic bars (3.5×2.5×50 mm³) were notched with a diamond disc saw with a thickness of 0.15 mm until achieving 45-50% of the initial height. The notches were sharpened using an automated razor blade device and diamond paste to avoid a finite notch radius effect during the test[118]. R-curve tests were performed according to SEVNB stable crack growth configuration in a very stiff displacement controlled house-made device[116]. In this apparatus, samples were set in a very rig metal frame, and force is measured by a high sensitive quartz sensor and a thin piezo actuator to determine the mechanical compliance of the sample. The mechanical setup is described in detail by Jelitto *et al.*[154]. The distances between the outer (s_1) and inner (s_2) rollers were 40 and 20 mm, respectively. A loading speed of 0.0012 mm/min was applied. Thereby, stable crack growth was achieved by partial unloading and reloading cycles. As soon as the crack started to propagate, the sample was partially unloaded by an automatic computer-controlled process based on the continuous evaluation of the slope in the load-displacement-diagram. The crack length was determined with the compliance method. Two-position encoders (displacement sensor WI/2mm-T, HBM, Hannover, Germany) were used, one placed at the center of the sample and the other one, 15 mm aside. By considering the difference of both displacement signals during partial unloading, the pure bending compliance could be calculated without the necessary correction due to the machine compliance. The equations are used based on beam theory, as described in detail by Fett and Diegele[155], exactly for the geometry of the given load cell. Thus, force and crack length were recorded at each cycle to determine fracture toughness (K_{IC}). For SEVNB 4-point-bending tests, Eqs. 9 and 10 were used[156]:

$$K_{IC} = \frac{3F \cdot \Delta s \cdot \sqrt{l} \cdot \Gamma(\alpha)}{2bh^{3/2}(1-\alpha)^{3/2}} \tag{9}$$

with

$$\Gamma(\alpha) = 1.1215\sqrt{\pi}\left[\frac{5}{8} - \frac{5}{12}\alpha + \frac{1}{8}\alpha^2 + 5\alpha^2(1-\alpha)^6 + \frac{3}{8}\, e^{\left(-6.1342\frac{\alpha}{(1-\alpha)}\right)}\right],$$

$$\alpha = \frac{l}{h} \text{ and } \Delta s = s_2 - s_1 \tag{10}$$

where F is the applied force on the specimen in each loading cycle; l, the crack length; b and h, the width and height of the specimen respectively; α, the relative crack length,

and $\Gamma(\alpha)$, a geometric factor. The work of fracture (W_F) was calculated by dividing the area under the load-displacement curves by twice the area of the unnotched parts of samples.

Residual stresses were measured according to Eq. 11 from Chartier *et al.*[64] for two dissimilar materials, X and Y,

$$\sigma_X = \Delta\varepsilon \cdot {E'}_X \cdot \left(1 + \frac{t_X \cdot {E'}_X \cdot n_X}{t_Y \cdot {E'}_Y \cdot n_Y}\right)^{-1}, \ \sigma_Y = \Delta\varepsilon \cdot {E'}_Y \cdot \left(1 + \frac{t_Y \cdot {E'}_Y \cdot n_Y}{t_X \cdot {E'}_X \cdot n_X}\right)^{-1} \quad (11)$$

where $\Delta\varepsilon$ is the difference in thermal strain between adjacent layers; $E' = \frac{E}{1-\nu}$ being E the elastic modulus and ν, the Poisson's ratio; t, the mean thickness of layers; and n, the number of layers. A Poisson's ratio of 0.22 for doped and both pure alumina materials. The other parameters were experimentally measured.

5.3 Results and discussion

Table 8 presents the relative density and average grain size of the monolithic reference samples after sintering. As expected, A1200 presents higher porosity and lower average grain size and dispersion of sizes compared to A1350. The use of dopants (D1200) presents higher densification and enhanced grain growth compared to both pure fine alumina samples, e.g. sintered at 1200 and 1350 °C. Enhancement in sintering is related to grain boundaries and volume diffusions and the presence of anion and cation vacancies[21, 27, 29, 132]. A low degree of densification was observed for C1350, similar to that obtained for A1200, with the smallest grain size. A previous work[133] with the coarse alumina sintered for 2 h at 1550 °C presented an RD of 98.6%. Therefore, the low degree of densification observed for C1350 is already expected. Furthermore, even with a higher average particle size compared to A samples, C1350 presented a final average grain size lower them A1200 and A1350.

Table 8 – Relative density and average grain size of monolithic reference samples.

Sample	RD (%)	AGS (nm)
A1200	72.9 ± 1.5	301 ± 126
A1350	90.3 ± 1.3	323 ± 154
D1200	97.8 ± 0.4	448 ± 230
C1350	74.2 ± 0.5	277 ± 157

Figure 47 shows the microstructure of the monolithic reference samples, next to grain size histograms. According to micrographs, is visible the higher degree porosity of A1200 compared to A1350 and D1200. The same for C1350 compared to A1350. Similar

histogram curves were obtained for pure alumina samples A and C, i.e. they present uniform grain size with resembling deviation. D1200 shows a higher deviation of values (flatter curve), with big and small grains together. It is interesting to observe that, unlike A and D materials, the coarse alumina (C) presents an average grain size smaller than the initial particle size (439 nm), and this may be related to the formation of agglomerates. Also, it is necessary to take into account that different characterization techniques were used, SEM for grain size and DLS for particle size.

Figure 47 – Microstructure of monolithic reference samples after sintering (on the left side) and histograms (on the right side) of grain size distribution.

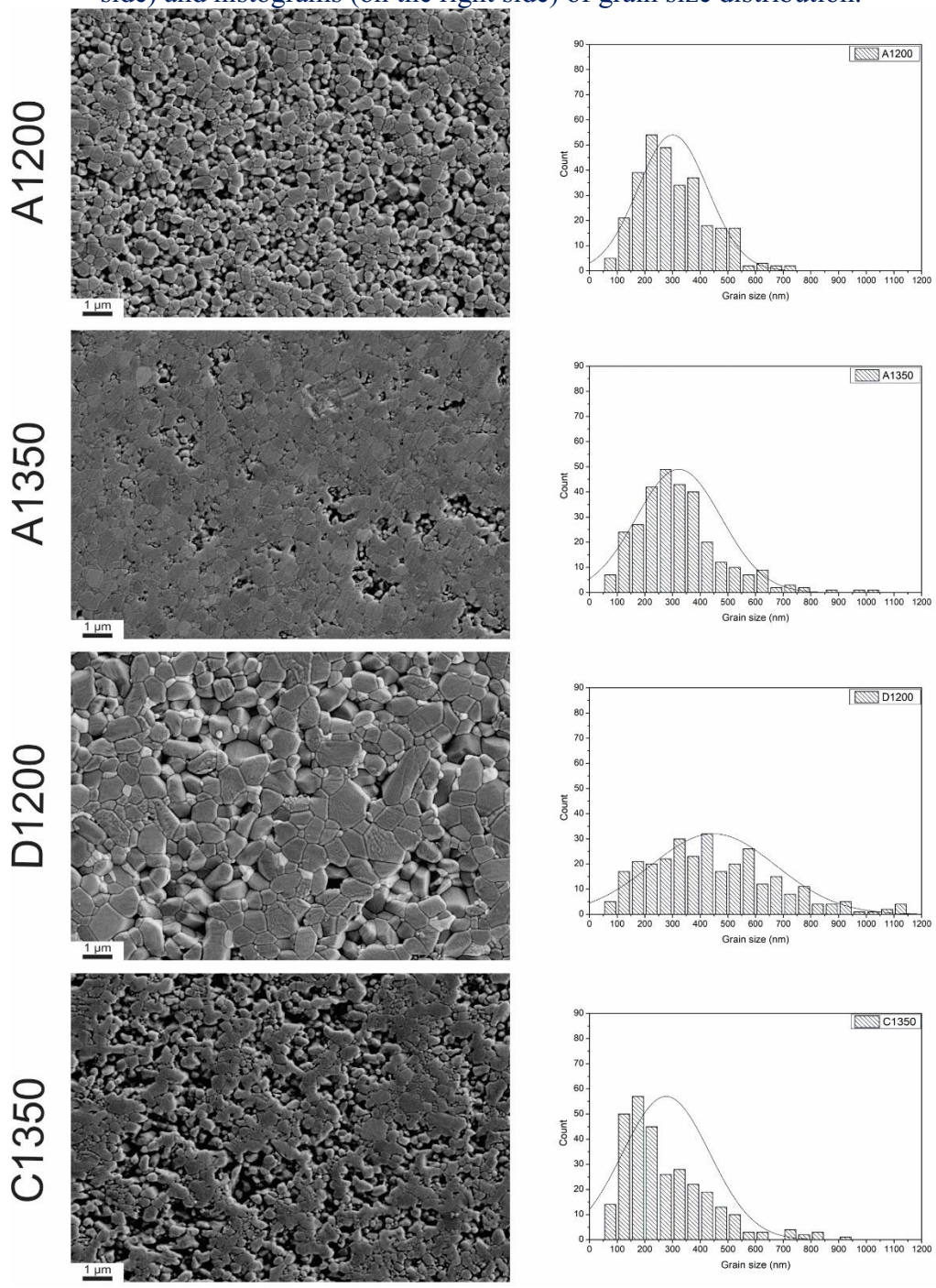

The Young´s modulus and hardness measured using nanoindentation are presented in Table 9. Both properties exhibited the well-known dependency on porosity, e.g. higher values for the denser samples[121]. An increase in hardness and modulus was observed in A with increasing sintering temperature. Doped alumina presented these properties higher than pure fine alumina, even for the one sintered at 1350 °C. The lowest hardness and E were observed for coarse alumina.

Table 9 – Values of Berkovich hardness and elastic modulus of monolithic samples measured by nanoindentation.

Sample	H (GPa)	E (GPa)
A1200	11 ± 1	236 ± 7
A1350	17 ± 2	303 ± 21
D1200	18 ± 2	352 ± 29
C1350	6 ± 1	146 ± 11

Table 10 presents the final average thickness of each layer in the sintered composites, the ratios between them and the estimated relative densities of composites were measured using monolithic reference densities and average layers thickness. It was observed that the values of the final ratio were not in accordance with the ones established in methodology, and this is directly linked to the processing of samples (e.g. differences in tapes' thickness and lamination process). However, different final ratios for each type of composite were achieved as intended. Compared to the reference materials, the relative density of composites reduces with the increasing volume of weak layers.

Table 10 – Estimated relative density, the average layer thickness of pure and doped alumina in each composite, and the layer thickness ratio obtained after sintering.

Sample	Thick layer (µm)	Thin layer (µm)	Final ratio (dense:porous)	RD (%)
DA-17L	353 ± 31	49 ± 11	7.1 : 1	95.1
DA-11L	400 ± 48	253 ± 91	1.6 : 1	89.2
DA-3L	910 ± 86	1640 ± 301	1 : 1.8	86.0
AC-17L	350 ± 59	121 ± 23	2.9 : 1	86.5

Figure 48 presents the produced composites on top, and the two different interfaces present in them, D with A and A with C. Samples were well-sintered with no macrodefects and warping, which would make them invalid for use in testing. Interfaces are well-bonded, with no delamination. Differences between the different layers are seen, e.g. differences in the grain size for D/A interface and the porosity for A/C interface.

Figure 48 – On the top, tested samples of DA-17L, DA-11L, DA-3L, and AC-17L. Below, the SEM micrographs of the interfaces D/A and A/C. The horizontal yellow lines help to identify the interface position.

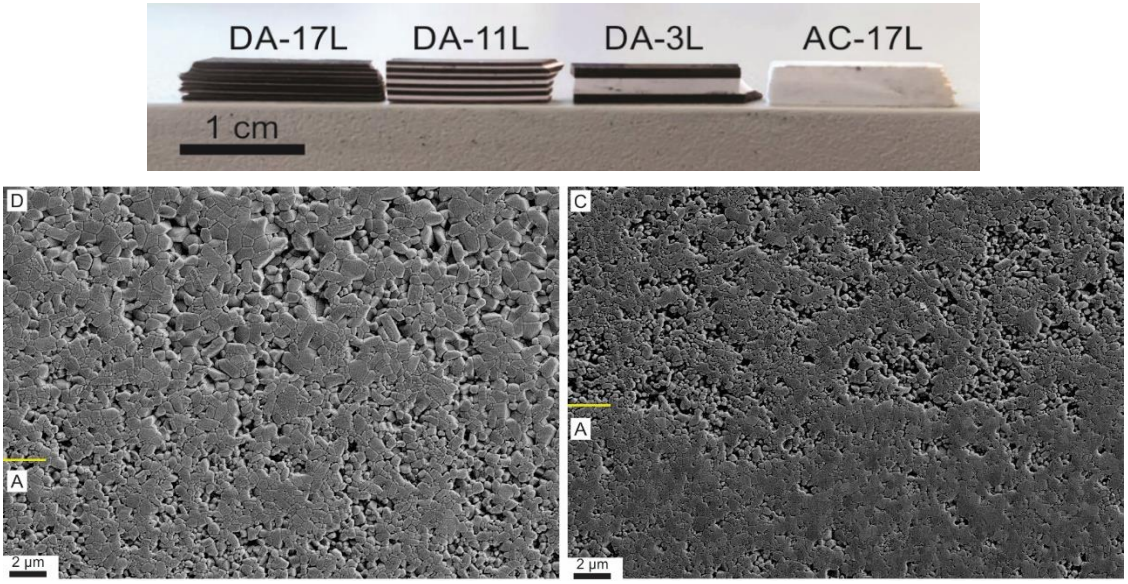

Figure 49 presents 4-point bending results, in the form of the Weibull analysis. To complement the results, Table 11 lists the number of tested samples, the average maximum strength (σ_f), the mean characteristic strength (σ_0) and the Weibull modulus (m) of each batch. Two-tailed *t*-tests with a 95% confidence interval, with a significance level (p-value) lower than 0.05, were applied for the comparison between bending strength. First, monolithic references A1350 and D1200 were compared, and it was proven the efficiency of using dopants to reduce the sintering temperature and enhance the sinterability of alumina, where no significant difference in mechanical strength was observed. Doped alumina samples presented larger grains, but also higher density, thereby compensating their effect on mechanical strength[157]. Still, the lower Weibull modulus of D1200 could be related to the presence of a large number of closed pores or the abnormal grain growth, once the grain size does not influence the *m* value[32, 158].

When the addition of alumina layers in the doped alumina matrix was analyzed, (D1200 with DA composites) strength significantly reduces when the ratio between layers' thickness is 1 (DA-11L) or lower (DA-3L), 16% and 13% respectively, indicating a slight weakening of samples with increasing weak layers thickness. However, no loss in the mechanical strength is observed for samples with the thinnest pure alumina layer, DA-17L. Regarding the reliability of laminates, the higher the thickness of Al_2O_3 layers is, the lower is the Weibull modulus. Residual stresses are considered not to be high enough to influence mechanical strength. For example, DA-17L, which has the highest

tensile and lowest compressive stresses of DA composites and presented no different strength compared to the reference. Comparing A1350 (reference) with AC-17L, no significant differences in maximum and mean characteristic strength are observed. Again, the ratio 4:1 between strong and weak layers made no difference in mechanical strength. A slight decrease of Weibull modulus is observed, which may be linked to the presence of porous layers. Also, the low residual stresses did not influence the strength.

Figure 49 – Flexural results (Weibull plot) of reference and composite materials.

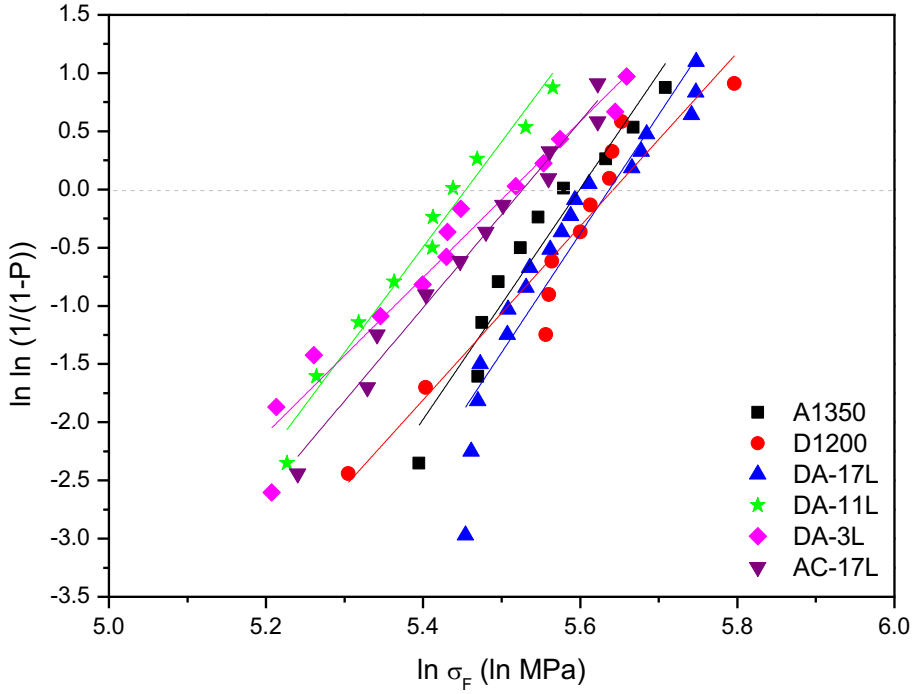

Table 11 – Average maximum strength (σ_f), mean characteristic strength (σ_0) and Weibull modulus (m) of tested samples in 4-point bending.

Sample	*Samples tested*	σ_f *(MPa)*	σ_0 *(MPa)*	*m*
A1350	10	258 ± 26	270	9.9
D1200	11	266 ± 33	282	7.5
DA-17L	19	268 ± 27	281	10.2
DA-11L	10	223 ± 24	234	9.1
DA-3L	13	232 ± 35	248	6.7
AC-17L	11	238 ± 29	251	8.0

Figure 50 shows the representative load-displacement curves obtained during R-curve measurements, corrected as done before in other works with the same device[115, 159]. This procedure was adopted because due to the dead weight of the machine's upper support the force did not start at zero. Even avoided during sample preparation, still, a small effect of the finite notch root radius[115] was observed in some cases (e.g. D1200 in Figure 50). Each dot represents the maximum force of each cycle.

Curves start with linear elastic behavior, as expected, until reaching the maximum force. After this, the crack starts to propagate and different force-displacement curve behavior are observed for reference materials and composites. Monolithic samples presented the typical behavior of materials that have a nearly constant K_{IC}. In these materials, cycle by cycle, displacement increases slightly as force decreases, according to the reduction of the sample cross-section (disregarding statistical scattering).

Composites exhibit different behavior compared to monolithic references. In DA composites, the force increases until the crack starts to propagate, then it goes down with a constant toughness regime. As the crack propagates in the porous region, it comes closer to the interface (which has residual stress fields) and approaches the next doped alumina dense region. Then, an increase in the force is necessary to drive the crack due to the mismatch of fracture energy. After entering the dense layer, the maximum forces at each cycle drop again until the next interfacial zone. The thicker the alumina layers, the higher the reinforcement effects. This is not likely caused by a size effect on reinforcement efficiency, e.g. the reinforcement effects should be large if both compressive and tensile layers have similar or the same added layer thicknesses, like DA-11L and DA-3L. Otherwise, the thick layers would dominate and the thin layers have less influence, which reduces the effect.

AC-17L sample follows the same fracture behavior observed for DA-17L composites. Their toughness reinforcement principle is the same, however in this case the different degrees of densification are caused by the different average particle sizes of starting powders.

Figure 50 – Load-displacement curves of R-curve measurements done in samples. On the left side are the curves for alumina and doped alumina, and on the right side for DA and AC composites.

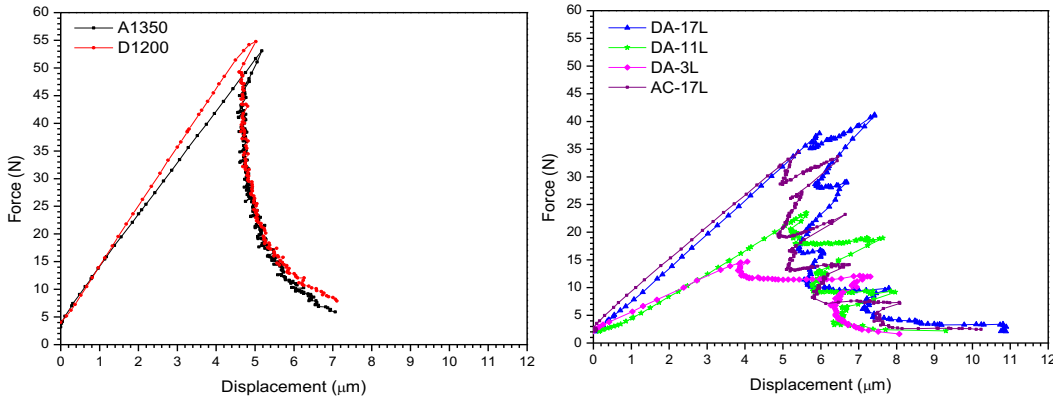

Figure 51 shows the results of fracture toughness as a function of the crack extension (measured right after the initial notch length). Mean fracture toughness and

work of fracture obtained were, respectively, 2.0 ± 0.1 $MPa \cdot m^{1/2}$ and 7.3 ± 0.7 Jm^{-2} for A1350, and 1.9 ± 0.2 $MPa \cdot m^{1/2}$ and 8.4 ± 1.4 Jm^{-2} for D1200. Both K_{IC} values are not significantly different, however higher work of fracture is observed for D1200 due to higher densification and the influence of large grains, which results in a larger crack surface[151]. A nearly constant R-curve behavior is observed for monolithic samples that presented a plateau-like behavior and did not exhibit a macroscopic toughening mechanism that could result in the R-curve effect. R-curve behavior of alumina tends to decrease with the decrease of grain size[160–162], once the increase in fracture toughness is related to crack branching, bridging grains, grain-boundary microcracking. It also must be taken into account that fracture is mainly intergranular in these materials.

Different R-curve behavior is observed for composites. Analyzing DA samples, an increase of crack resistance was observed when the crack reaches the interface zone, following the behavior observed in force-displacement curves. When the rising-plateau steps of force occur, fracture toughness increases until reaching a maximum. After that, the force decreases due to propagation in dense layers, and fracture resistance decreases together with it until reaching a minimum. This cycle repeats every time the crack approaches the weak pure-dense doped alumina interface. The thinner the pure alumina layers are, the slighter is the increase in K_{IC}.

The R-curves of the samples DA-17L exhibit four local maxima when the crack passes through the corresponding four interfaces to the next doped alumina layer. The R-curves of the DA-3L beams have only one maximum because the crack starts in the middle of the sample and reaches only one interface. Due to the computer-controlled stable crack advance, the data points are relatively close together with low statistical scattering. Again, as observed in the force-displacement curves, the R-curves of AC-17L samples are very similar to the ones obtained for DA-17L, once they have the same layers' thickness ratio.

Figure 51 – R-curve of A1350, D1200, and DA and AC composites.

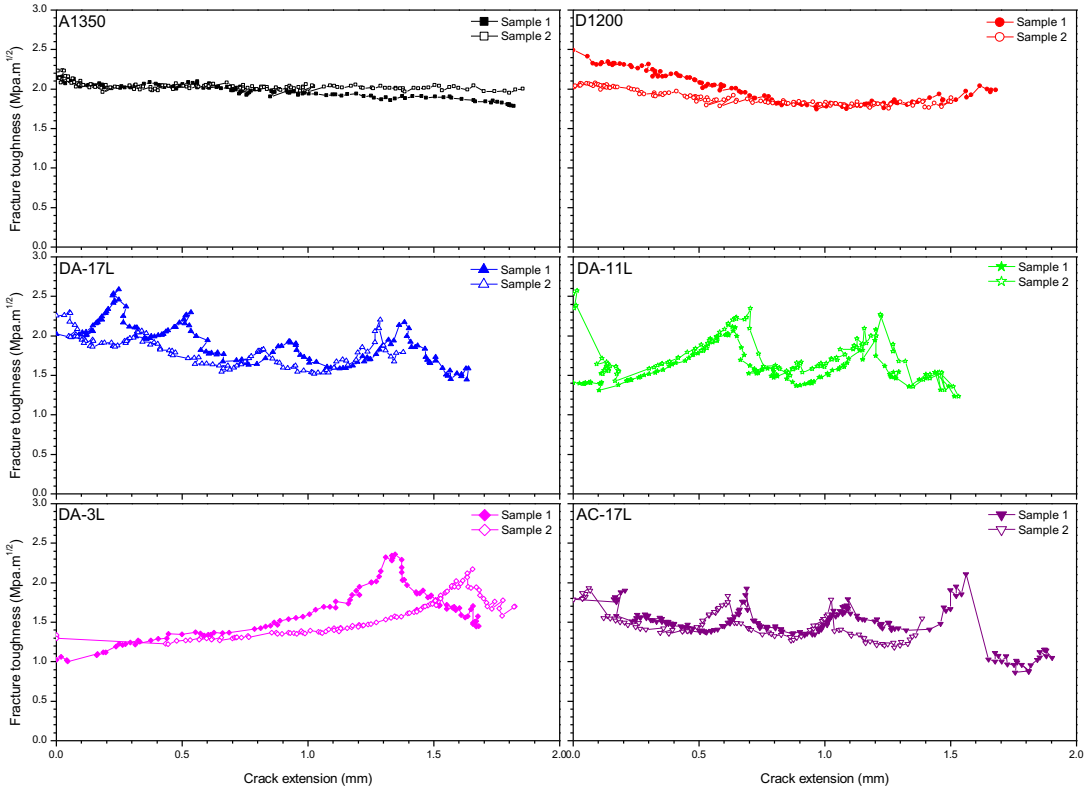

Table 12 shows the work of fracture, the average maximum and minimum values of fracture toughness for each composite (2 samples), $K_{IC\ max}$ and $K_{IC\ min}$ respectively, and the average difference between them for each sample in each type of composite. By comparing these values with those obtained for monolithic samples, it is observed that the minimum K_{IC} of composites is lower, but the maximum K_{IC} is higher. Furthermore, the thicker the pure alumina layers in DA composites, the higher the difference in the minimum and maximum values of fracture toughness. Thus, the alterations of fracture resistance during crack propagation can be tailored by the ratio between dense and porous layers. The R-curve behavior of AC-17L has a similar shape to that of DA-17L. The difference between $K_{IC\ max}$ and $K_{IC\ min}$ is similar to DA-17L, indicating that the ratio thickness of both gives the same response in fracture toughness. However, values of K_{IC} maximum and minimum are lower than those for DA-17L, due to de higher porosity and lower elastic modulus involved in AC-17L. The work of fracture reduces with the introduction of weak layers, inversely proportional to the thickness of porous layers. The lower the composite relative density, the lower the W_F. Over again, E and RD of the AC-17L system resulted in the lowest work of fracture observed.

Table 12 – Values of average K_{IC} maximum and minimum, and the average difference between them, and the work of fracture.

Sample	$K_{IC\ min}$ (MPa·m$^{1/2}$)	$K_{IC\ max}$ (MPa·m$^{1/2}$)	$K_{IC\ max} - K_{IC\ min}$ (MPa·m$^{1/2}$)	W_F (Jm^{-2})
DA-17L	1.7 ± 0.2	2.1 ± 0.2	0.4 ± 0.1	7.5 ± 0.3
DA-11L	1.3 ± 0.1	2.2 ± 0.2	0.8 ± 0.1	6.5 ± 0.6
DA-3L	1.3 ± 0.2	2.2 ± 0.1	1.3 ± 0.1	5.1 ± 0.7
AC-17L	1.3 ± 0.2	1.9 ± 0.2	0.5 ± 0.1	3.3 ± 0.5

To better understand the effect of the interface in composites with different layer porosity, two more samples of DA-3L were made with a smaller notch, where the tip stays before the first interface, still in the doped alumina dense layer. One of the samples was notched close to the interface, and the other far from the interface, around 30% and 15% of samples' height, respectively. R-curve results are shown in Figure 52, together with a DA-3L reference sample (DA-3L in Figure 50 and Figure 51 - sample 1) where the crack starts to propagate in the middle of the weak pure alumina layer.

Figure 52 – Load-displacement (on the left side) and R-curve (on the right side) for samples of DA-3L tested with different notch lengths, so that crack tip was in different positions: in the middle of the weak pure alumina layer and the first doped alumina layer (far and next to the interface).

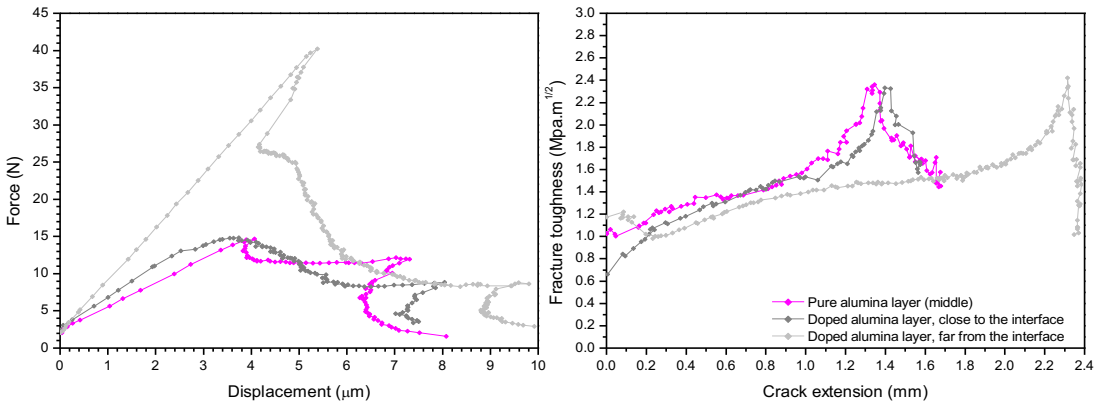

The sharp (tilted) maximum of the light gray curve (left diagram) stems from an overload, necessary to start the crack from the short notch (far from the interface). The maxima at 7, 8, and 9 μm displacement correspond to the maxima at 1.4 and 2.3 mm crack extension in the right diagram. As crack starts to propagate in the doped dense layer, the required force to drive the crack goes down as the remaining layer cross-section gets smaller. Also, in this region, the crack moves into the porous layer, which is favored as confirmed considering the ratio of fracture energy and elastic mismatch outlined by He and Hutchinson plot (reduction of maximum force), useful to predict if a crack could be deflected or not at the interface between dissimilar elastic materials[163]. Then, the crack comes closer to the interface, from a porous to dense layer, where there is a small stress

field. Directly at the interface, the advancing of the crack is hindered by the change of fracture energy, resulting in the observed rising plateau of force and an increase in fracture toughness. After entering the next layer, the crack is again in a dense region and propagates stably until complete failure, similarly to the monolithic references.

Cooling after sintering developed different degrees of residual stresses, which play a role in fracture toughness and crack behavior of composites. The difference between calculated CTE (Chapter 3) implies different residual stresses in the layers of each type of composite (see Table 13). Compressive stresses help to improve fracture toughness, on the other hand, tensile stresses depreciate crack resistance. Notwithstanding, the magnitude of them is not sufficiently high to modify the crack path (e. g. by crack arresting or bifurcation) in compressive layers or to induce unstable crack growth in tensile layers in DA composites and AC-17L.

Table 13 – Values of residual stresses calculated by Eqs. 1 and 2 in layers of composites DA-17L, DA-11L, DA-3L and AC-17L. The negative signal is referred to as compressive stress, while the positive signal is tensile stress.

Sample	**Residual stresses (MPa)**	
DA-17L	D layers	-20
	A layers	163
DA-11L	D layers	-68
	A layers	129
DA-3L	D layers	-97
	A layers	108
AC-17L	A layers	-39
	C layers	127

Figure 53 presents the fracture surfaces of tested R-curve samples. Investigations of the fractured surfaces of composites DA and AC-17L did not reveal visible modifications (e.g. crack arrest or deflection) in the crack path. As occurred with the monolithic samples, the crack propagates nearly linearly through the sample, with flat crack faces. Differences in the densification/porosity between layers do not have any influence on the crack path.

Figure 53 – Micrographs of fractured samples, OM on the left side, and SEM on the right side. SEM was carried out with an angled sample holder that allows the sample to be at 45° regarding the electron beam.

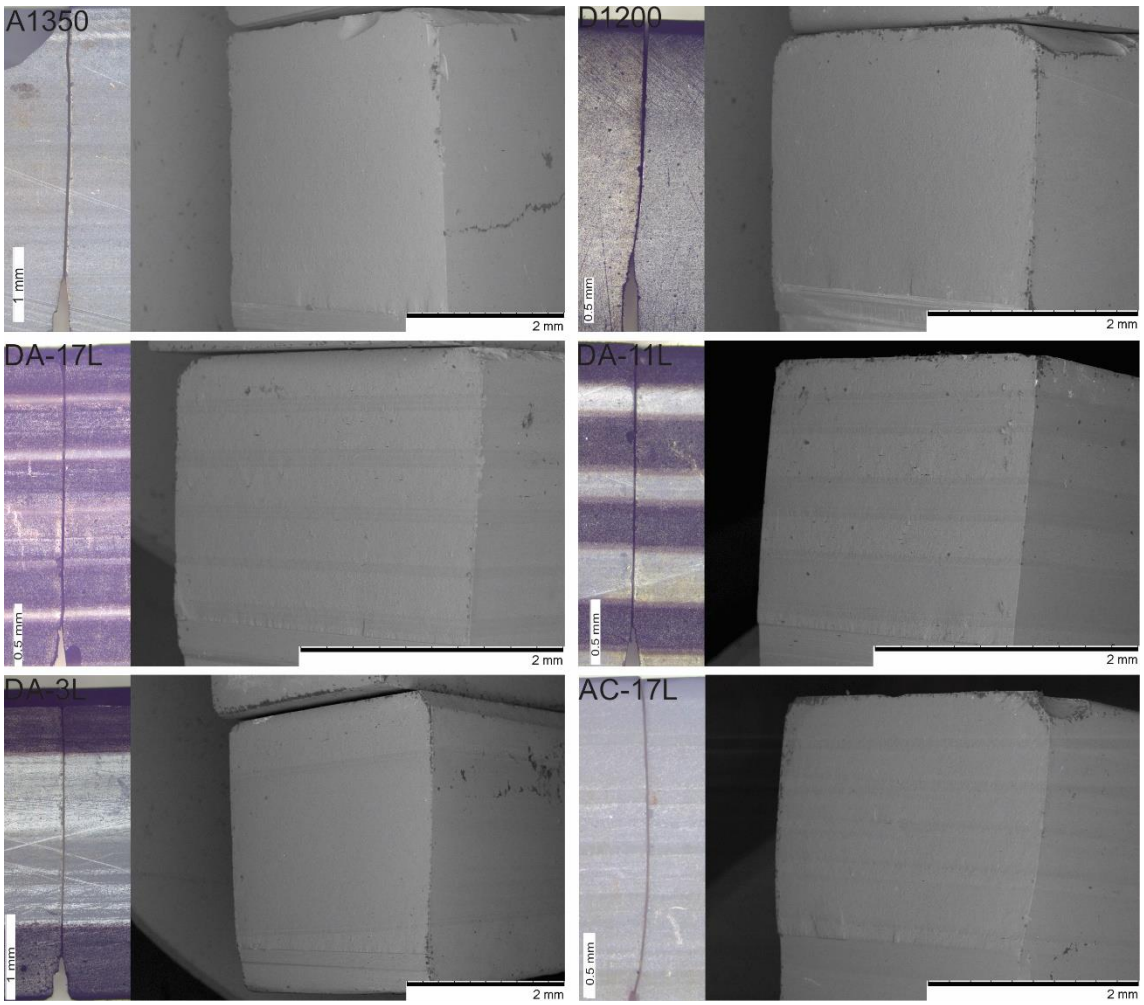

5.4 Conclusions

Samples presented the well-known dependence of densification and grain growth according to the sintering temperature. The presence of dopants enhanced alumina densification. Young's modulus and hardness are directly proportional to the density and porosity of the material.

Four-point bending tests showed that the mechanical strength of alumina sintered at 1350 °C is statistically in the same range as doped alumina sintered at 1200 °C, confirming the effectiveness of dopants in reducing the sintering temperature of alumina without substantial changes of mechanical properties. In layered composites with weak layers, it was observed that samples with thin weak layers (DA-17L and AC-17L) did not lose strength when compared to the references, unlike samples DA-11L and DA-3L with thicker weak layers that presented a slight decrease in strength. Thus, for thin weak layers,

their effect on the strength is negligible. As this thickness increases, a loss in strength must be taken into account.

Monolithic samples presented nearly constant resistance during crack propagation. However, laminates presented an alternation behavior: K_{IC} increases when the crack propagates through the interfacial zones, from weak layers to dense layers. This reinforcement effect is more evidenced (differences between K_{IC} minimum and maximum are higher) for increased thickness of porous layers. The work of fracture of samples is inversely proportional to the thickness and, consequently, to the volume of the porous layer. It was assumed that residual stresses have no effects on the strength and no influence on crack propagation. However, even in low values, their influence on fracture toughness and R-curve behavior should be considered.

Chapter 6 – Using polystyrene spheres to produce thin porous interlayers in alumina laminates[4]

6.1 Introduction

The use of weak interfaces or layers inside ceramic matrix composites is an idea first employed in fiber-reinforced composites[71]. Ceramic-ceramic layered composites have been designed and processed based on weak interfaces between dense and rigid layers to originate crack deflection and their fracture behavior in flexure under loads perpendicular to the layers has been analyzed in terms of crack propagation and strength. Compared to monolithic references, these materials can substantially reach higher values of fracture toughness and work of fracture, and non-catastrophic failure[72, 73].

The selection of the material to compose the weak interfaces/layers is a key step in laminates design. In general, the matrix layer must have good mechanical strength, while the weak parts rule the fracture toughness and work of fracture. Thus, the interface must have a low fracture resistance, but sufficiently enough to maintain the integrity of the material during use. That way, toughening phenomena such as delamination and deflection can occur when the crack reaches the interface, deviating its propagation path[75, 76]. Usually, the mechanical strength of these materials is similar to that of dense layers[55]. The use of pyrolysable pore formers (e. g. starch, graphite, and polymers) is a widely used approach to form porous layers, yielding stable pores after the debinding process. The use of pore formers has good control over the features of the porosity and final mechanical properties of the material, considering that their amount, particle size, shape, and thermal properties (decomposition/oxidation) can be well controlled[164].

Using the same material in both layers results in good chemical compatibility and no/very low residual stresses due to cooling after sintering. The volume fraction of pores required for crack deflection and the pore interaction play an important role to ensure crack propagation in the weak parts of the material[165]. Besides, there is less material to be broken by the advancing crack in the porous layers and so, is considered to have lower fracture energies than the dense parts[149]. For dense-porous laminate composed of the same materials, a crack will deflect when the ratio between the fracture energy of the ligament and the next pore (G_{lig}), and the fracture energy of the strong dense layer (G_d) is lower than 0.57[81, 83]. Considering the effect of interaction between pores, it is assumed that the

[4]Submitted for publication.

fracture energy of the ligament is related to that of the porous layer (G_p) by the relation $G_{lig} = \frac{G_p}{(1-\mathrm{P})}$, where P is the volume fraction of porosity, being the expression finally expressed by $\frac{G_p}{G_d} < 0.57\ (1-P)$[86].

In this chapter, alumina porous interlayers with monodisperse porosity created by polystyrene (PS) spheres were developed, and after laminated between alumina tapes to create a laminate with thick dense layers and thin weak interlayers. In the first part of the work, grain and pore size were analyzed as a function of the volume of added PS spheres, and the processing of laminates is established. Finally, laminates were produced and their microstructure and mechanical properties were investigated.

6.2 Materials and methods

6.2.1 Development and characterization of porous layers

An alumina (Taimicron TM-DAR, d_{50} = 150 nm, Taimei Chemicals, Japan) suspension with 45 vol% of solids was produced with deionized water and 1 wt% (referred to solid content) of dispersant Dolapix CE 64 (Zchimmer & Schwarz, Germany). The powder was dispersed with a sonotrode UP100H (Hielscher Ultrasonics, Germany) for 30 min with an amplitude of 50% and a pulse time of 0.5 s. A monodisperse aqueous suspension of polystyrene spheres (microParticles, Germany) with a diameter of 0.76 ± 0.02 μm and solids content of 5 wt% was added to the alumina suspension with a volume ratio of 3:1, 7:1, and 13:1 to obtain 15, 30 and 45%, respectively, of the volume of solids constituted by PS spheres. After that, the final suspension (Al_2O_3 + PS spheres) was dispersed 5 min longer with the sonotrode in the same parameters as noted before.

Alumina samples (15×15 mm^2) were produced by stacking and laminating 4 tapes of Al_2O_3. Processing of tapes and lamination procedures were already described in a previous study[166]. The coating was produced pouring less than 1 μL of suspension over the substrate, after spreading it with the pipette tip to ensure more coverage and let to dry at room temperature for 12 h. Residual water and organics were removed in a pre-sintering step at 550 °C for 1h, using a heating rate of 0.3 °C/min. Then, samples were heated up at a rate of 5 °C/min and sintered in air at 1350 °C for 2h.

The morphology of samples was analyzed by scanning electron microscopy (Supra VP 55, Zeiss, Germany). An image analysis software (Lince 2.4.2e, Ceramics

Group, TU Darmstadt, Germany) was used to measure the pore size (at least 40 measures per sample), and the grain size applying the line-intercept method (at least 200 measures per sample). Different thermal analysis was performed together with thermogravimetry in a simultaneous thermal analyzer (TGA/DSC 1, Mettler-Toledo GmbH, Germany) in PS spheres. The test was done in synthetic air (20% oxygen + 80% nitrogen) from room temperature to 550 °C, with a heating rate of 1 °C/min. After a dwell of 1h, the sample was heated to 800 °C with a heating rate of 5 °C/min.

6.2.2 Development and characterization of laminates with porous interlayers

The configuration with 45 vol% of porosity was chosen to be used as interlayers in laminates to achieve the highest porosity. Preliminary tests of lamination showed bad adhesion between the porous layer and a non-covered substrate. To give the system a better interface adhesion, 10 wt% referred to the solids content of binder (Mowilith LDM 6138, Celanese, USA) was added to the slurry and mixed with the sonotrode for 3 min. A volume of 2 µL of the binder-modified alumina-PS spheres slurry was deposited by drop casting on the laminated alumina substrates (4 stacked tapes per layer) with 15×50 mm^2. Eight drop-casted laminated substrates were overlapped and 1 non-coated substrate was placed over the stack to obtain 9 dense alumina layers and 8 porous interlayers after sintering. This configuration was intended to obtain a final thickness of around 3.5 mm. After warm-press lamination, the sintering step was performed as described in the section before.

The SEM was used to analyze the microstructure and fracture surfaces of samples. The density of monolithic sintered samples was measured using an analytical balance and applying the Archimedes method (ABT 100-5NM, Kern, Germany). A nanoindenter (G200, Agilent Technologies, USA) equipped with a Berkovich tip was used to measure the elastic modulus and hardness of monolithic sintered samples. At least 25 indentations were performed for each measurement by using the CSM technique[153]. Also, two Vickers indentation (Zwick 3212, ZwickRoell Testing Systems, Austria) was performed applying 0.5 kg during 10 s, at the dense layer and next to the interface with porous one. The main objective of this test is to make a pre-analysis of the crack propagation behavior through the porous layers, comparing with the crack propagation through the dense layer. For both Berkovich and Vickers indentation tests, a small grinded-polished sample was used composed of two dense layers and one porous layer produced in the preliminary lamination tests.

Fifteen as-sintered prismatic bars (3.5 × 3.0 × 25 mm^3) cut from the laminated samples were submitted to four-point bending tests using a universal test machine (Series 1605B, ATS, USA), with a loading speed of 1 mm/min and distance between outer and inner spans of 20 and 10 mm, respectively. R-Curve tests were performed using 2 prismatic notched bars (3.5 × 3.0 × 50 mm³) and the SEVNB stable crack growth method in a house-made device[116], as already described[166]. Outer (s_1) and inner (s_2) rollers were set with 40 and 20 mm, respectively. The values of force (F) and crack length (l) were continuously recorded at each loading cycle to determine fracture toughness (K_{IC}) according to equations 9 and 10[156]. The work of fracture (W_F) was is given by equation 13[167], where S_{LD} is the area under the load-displacement curve and l_0 is the initial crack length (notch length).

$$W_F = \frac{S_{LD}}{2b(h-l_0)} \tag{13}$$

6.3 Results and discussion

6.3.1 Development and characterization of porous layers

Figure 54 presents the micrograph of PS spheres used to produce the monodisperse porosity after sintering and its thermogravimetric analysis. A regular spherical shape is observed for PS particles. The degradation of PS spheres started at 265 °C and is finished at 500 °C, indicating that the same debinding curve performed in chapters before is suitable to be used for the laminates with porous interlayers (A-PS).

Figure 54 – The SEM micrograph of PS spheres used to form porosity in sintered laminates (on the left side) and thermogravimetric analyses of PS spheres (on the right side).

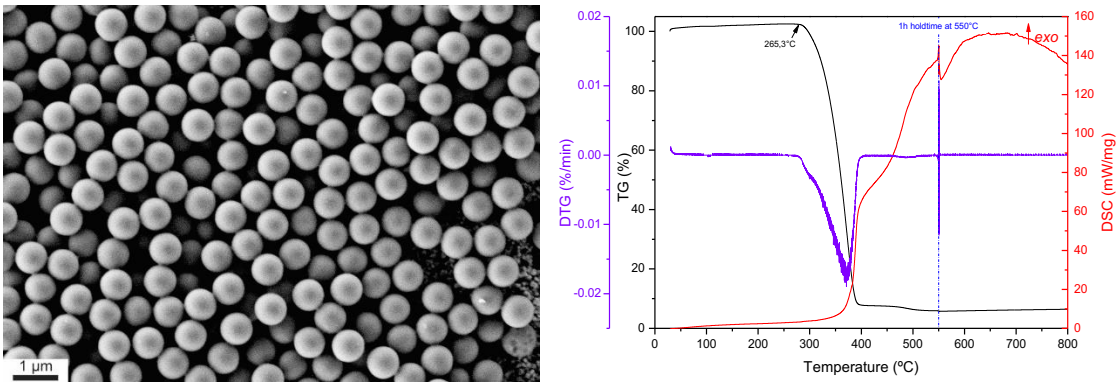

Figure 55 resented the transversal section and the free surface of samples. The thickness of alumina films ranged from 2 to 15 µm, with the artificial pores randomly distributed. Distribution of large and small grains was observed, with the last more

concentrated around pores. Pores walls presented rounded and linear shapes, with a tendency of being more rounded as the volume of added PS spheres increases.

Figure 55 – Micrographs of sintered substrates coated with the alumina and polystyrene spheres slurry containing 15, 30 and 45 vol% of PS. On the left side, the cross-section of a fractured sample. On the right side, the top surface view.

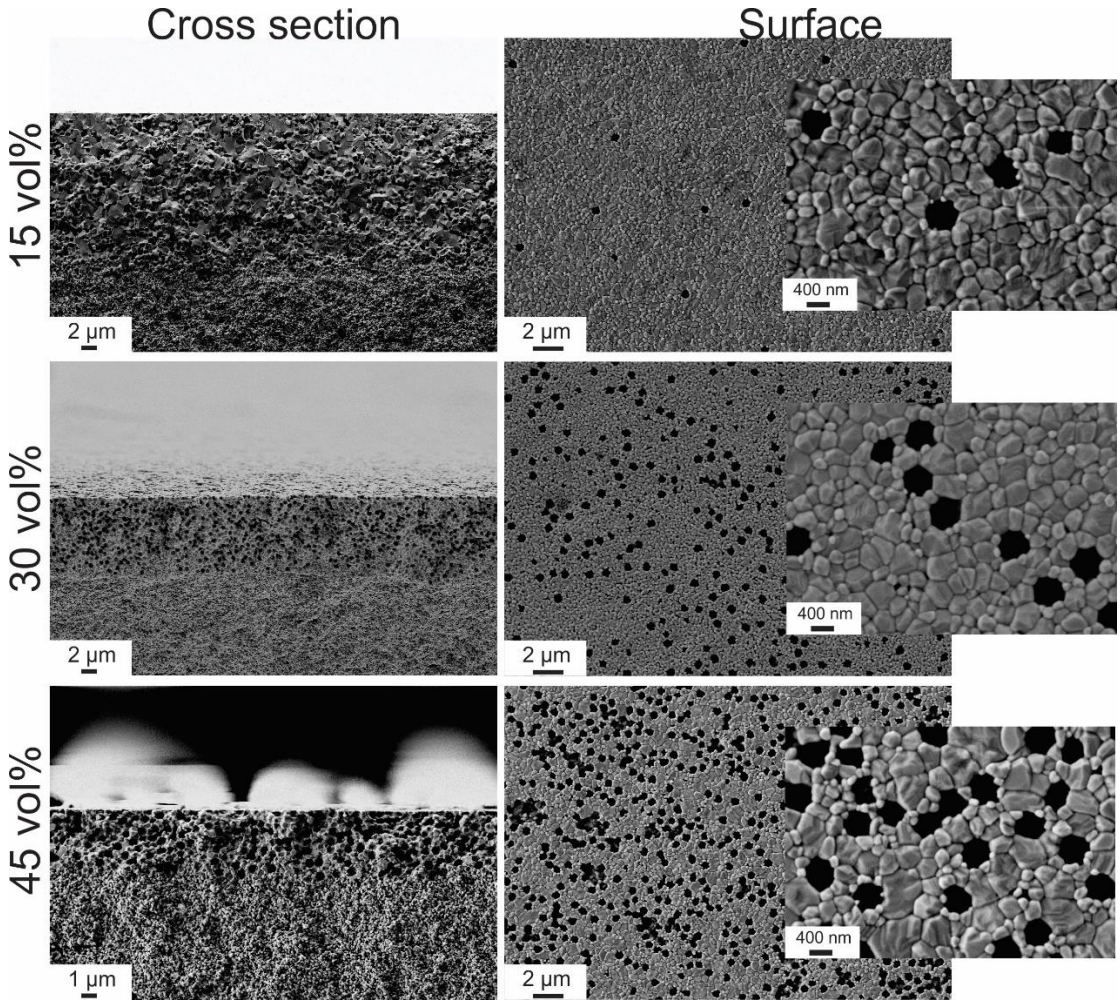

The histogram (Figure 56) presents the grain size distribution and the average grain size of sintered samples. The increase of volume fraction of pores tends to decrease the average grain size, due to the higher volume of voids that limits the grain boundaries movements and reduces the number of neighboring grains that feed the grain growth[168]. However, due to the high standard deviation of average grain size measurements, the presented values are not statistically different.

Figure 56 – Histogram of the grain size distribution for sintered samples.

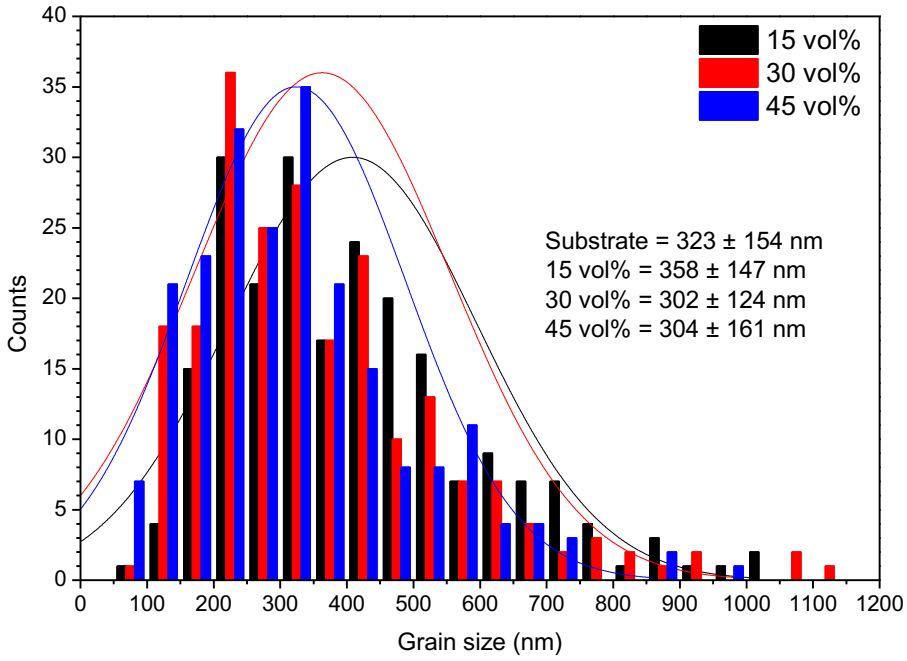

Compared to the surface ones, the measured average bulk pore size is higher for all samples, (Table 14). When the slurry was cast over the substrate, after drying, most PS spheres stay partially submerged. Thus, what was observed at the surface is not the maximum diameter of the pore, which would be observed with 50% of the diameter, and this is the reason for lower values compared to the bulk measurements[168]. When each group is analyzed separately, bulk and surface, there is no significate difference in the average pore size with increasing the volume of PS spheres, following the results presented by Pasquarelli *et al.*[168]. The measured average size of the surface and bulk pores reduced 46 and 30% of the initial size, respectively.

Table 14 – Average diameter of pores measured in the bulk part and at the top surface view.

Sample	Pore – surface (nm)	Pore – bulk (nm)
15 vol%	415 ± 68	538 ± 79
30 vol%	401 ± 52	537 ± 61
45 vol%	419 ± 40	517 ± 83

6.3.2 Development and characterization of laminates with porous interlayers

The alumina film with 45 vol% of PS spheres was chosen to be the interlayers of A-PS composites. The difference in using binder in the slurry composition of interlayers can be observed in Figure 57. When no binder is added, delamination and bad adhesion between layers was observed, instead of good adhesion observed when the binder is used.

A-PS samples presented a relative density of 89.7 ± 4.3%, which is not significative different from the density obtained for the reference monolithic material (90.3 ± 1.3%)[166].

Figure 57 – Lamination performed with interlayer without the binder (on the left side) and with the addition of binder in the composition of slurry (on the right side).

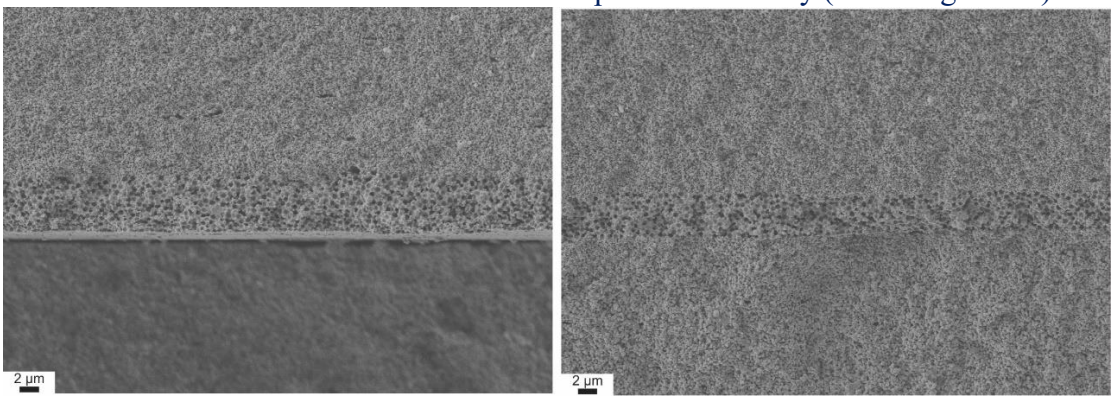

Results of nanoindentation presented for alumina dense layers an average Young's modulus and hardness of 354 ± 19 GPa and 18 ± 1 GPa, respectively. Porous interlayers presented an average Young's modulus and hardness of 119 ± 8 GPa and 5 ± 1 GPa, respectively. However, inaccuracies in measurements along with the porous interlayers typically occur due to tip interaction with pores. When the tip penetrates the pores, the load-displacement curve is shifted horizontally to the same load once the pore makes no resistance to penetration. This is demonstrated in Figure 58, where this effect is observed for a porous interlayer sample (marked with a dashed red square). The maximum load observed for dense and porous layers was around 850 and 300 mN, respectively.

Figure 58 – Two nanoindentations performed in both dense and porous interlayer showing the typical load-displacement curves obtained for each layer. The dashed red square highlights the region where the tip presented no resistance to penetrate the porous interlayer.

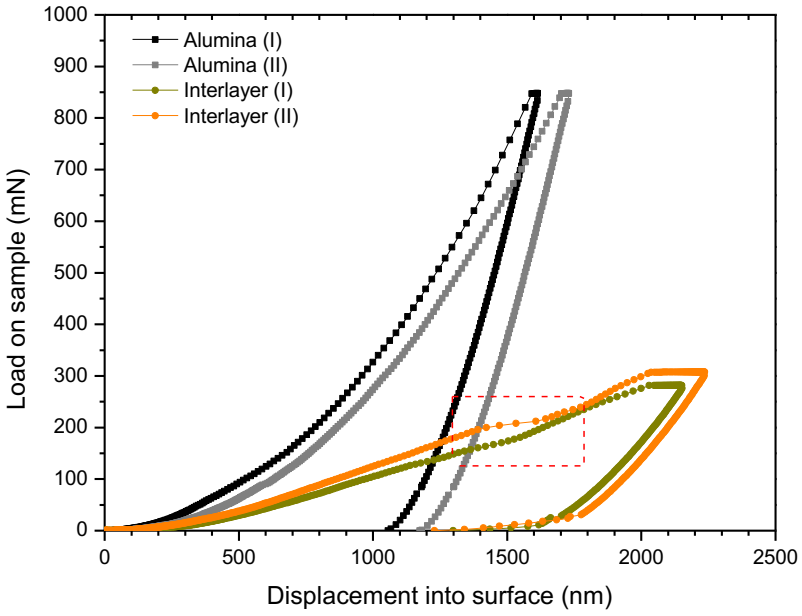

Figure 59 shows the Vickers indentations performed over the alumina dense layer, next to the interface. The measured crack size for the crack propagated through dense and porous layers was 35µm and 9 µm for the first indentation, and 38 µm and 9.5 µm for the second indentation, respectively. As a first impression, it is suggested that the porous layer avoided linear crack propagation, and absorbed the crack fracture energy. The crack seems to deviate and propagate inside the porous layer, not going on to the next dense layer. However, is important to emphasize, this is a local test to investigate the damage and cracks on the tested surface, i. e. not the crack behavior along all the cross section.

Figure 59 – Vickers indentation with 0.5 kg performed next to the interface. On the left side, the indentation, on the right side the crack going towards the interlayer.

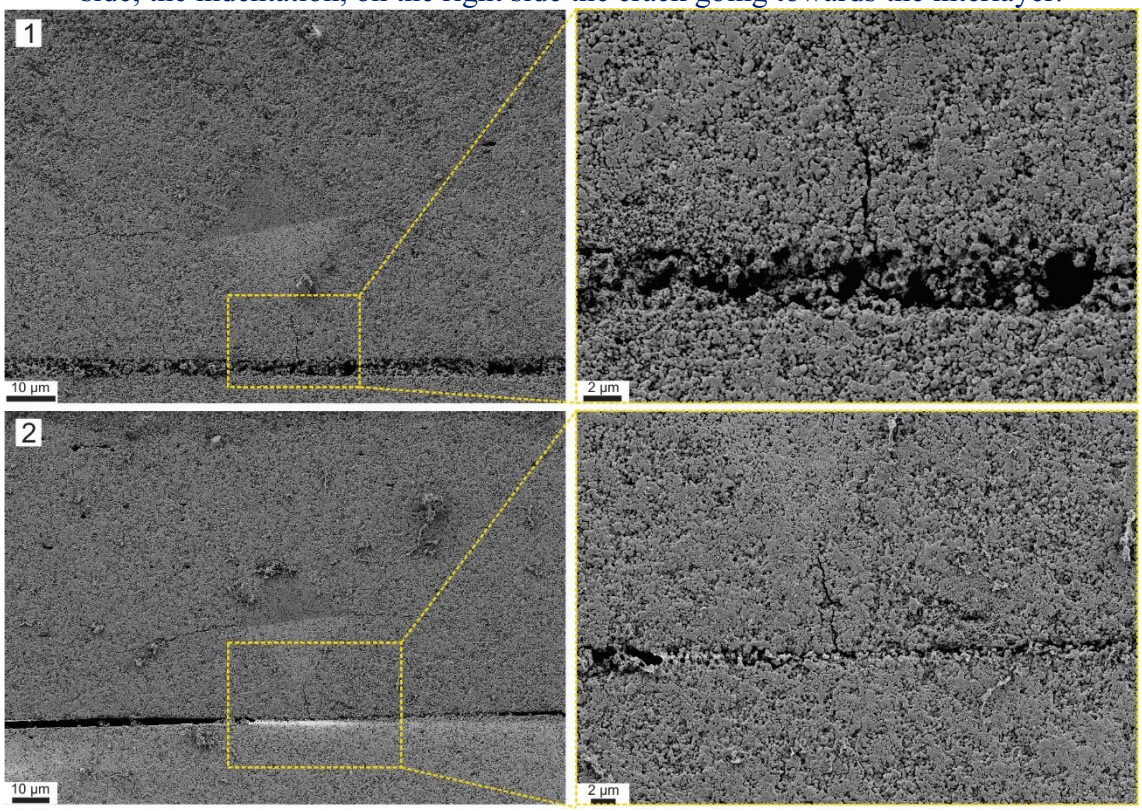

Flexural tests of A-PS (Figure 60) showed higher values of maximum strength, 278 ± 29 MPa, and mean strength, 292 MPa, compared to the alumina reference presented in Chapter 5 (258 ± 26 MPa and 270 MPa, respectively). These values are not significantly different when submitted to two-tailed *t*-tests with a 95% confidence interval, however, the p-value is equal to 0,0561, i. e. very near to consider them different. The Weibull modulus is slightly smaller (9.2) than the one for A1350 (9.9), which can be attributed to the presence of porous interlayers modifying the critical defect size.

Figure 60 – Flexural results (Weibull plot) of A-PS samples (orange points), together with the reference A1350 (black points, presented in Chapter 5) for comparison.

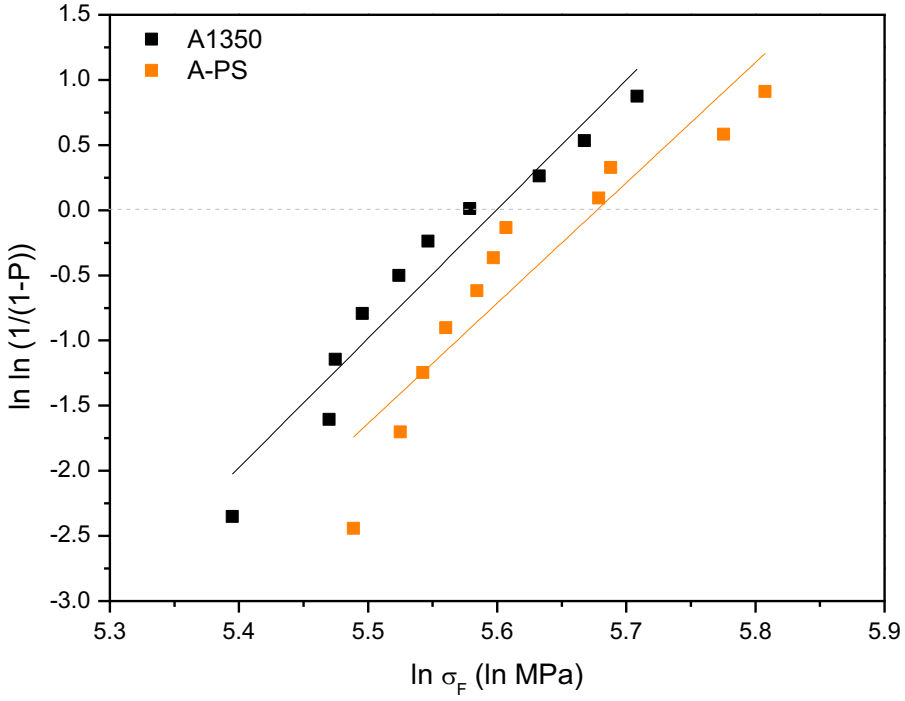

Load-displacement and fracture toughness-crack extension curves of A-PS samples are shown in Figure 61, together with the reference A1350 for comparison. While the reference presents a nearly constant decrease of force and increase of displacement during the test, A-PS presents some tortuosity in the curve caused by the crack propagation through porous layers, which directly reflects slight increases and decreases of K_{IC} during crack propagation. The average of fracture toughness and work of fracture observed in these materials are 1.7 ± 0.5 MPa·m$^{1/2}$ and 7.5 ± 0.3 Jm^{-2}, respectively, both similar to that observed for the reference (2.0 ± 0.1 MPa·m$^{1/2}$ and 7.3 ± 0.7 Jm^{-2}).

Figure 61 – Force-displacement curves (on the left side) and R-curves (on the right side) of A-PS samples. The black points are the results of A1350 reference.

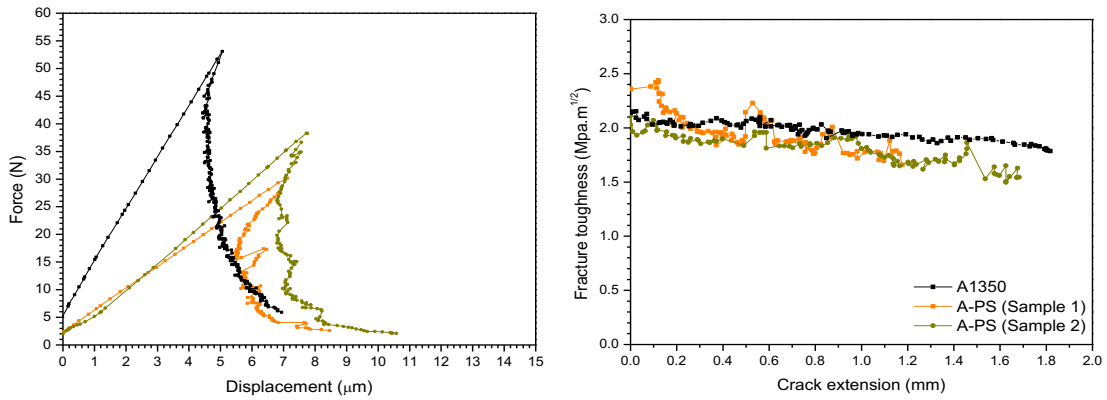

When the A-PS microstructure was analyzed by SEM (Figure 62), the presence of porous interlayers between dense alumina layers, was observed but not exhibiting well-

formed, rounded shaped pores as visible in the small scale tests (see Figure 58). It is most likely that the previously used lamination process to produce samples with the necessary size for flexural and R-curve tests altered the structure of porous interlayers, e.g. used pressure or temperature.

Figure 62 – SEM Micrographs at different magnifications of porous interlayers observed in A-PS laminates tested in flexural and R-curves tests.

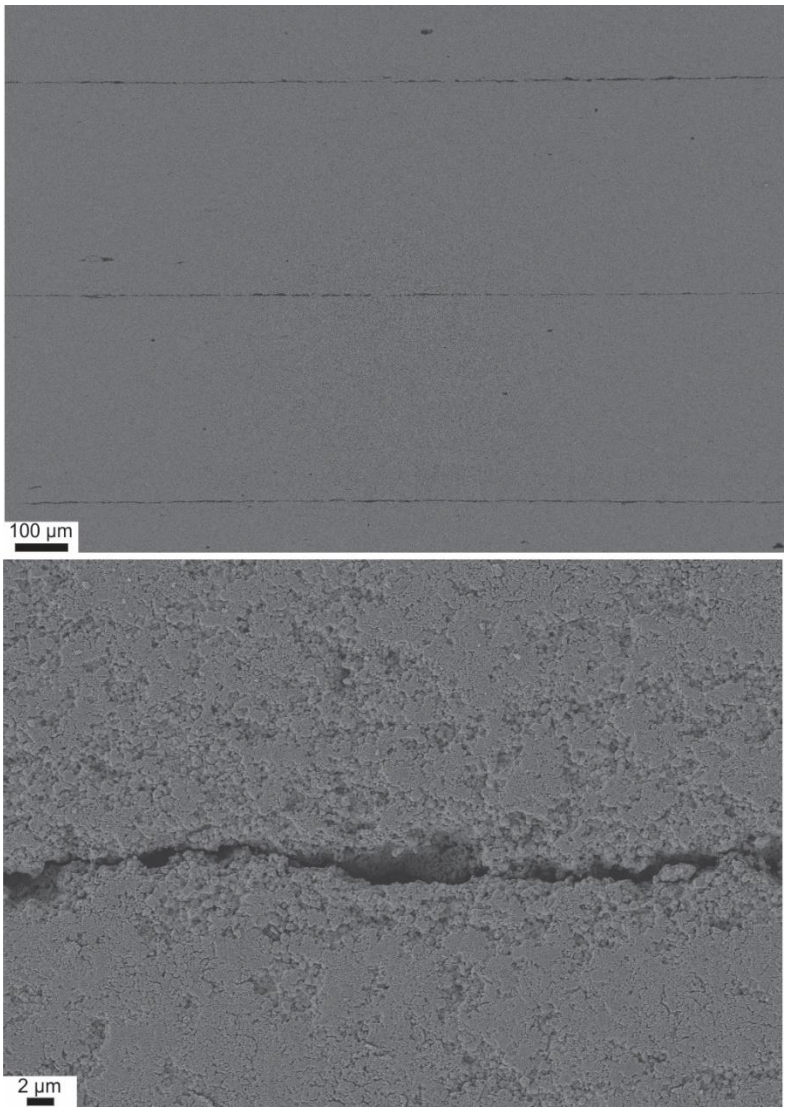

The micrographs of fractured surfaces showed no significant large-scale changes in the crack path (Figure 63, a). Still, although some samples presented flat fractured surfaces (Figure 63, b), others presented some roughness features due to modifications of the crack path (Figure 63, c and d), which may be linked to delamination zones. When interfacial zones are analyzed deeply, the formation of “steps” is observed, e. g. small deviations of the crack path (Figure 63, e) and crack branching (Figure 63, f).

Figure 63 – Micrographs of fractured surfaces of A-PS. Longitudinal sections showed no macro deviations of the crack path (a, OM); flat surface (b, SEM); fractured surfaces with roughness, not flat (c, SEM); detailed small deviations of the crack path when it propagates through porous layers (d, SEM); and crack branching (e, SEM).

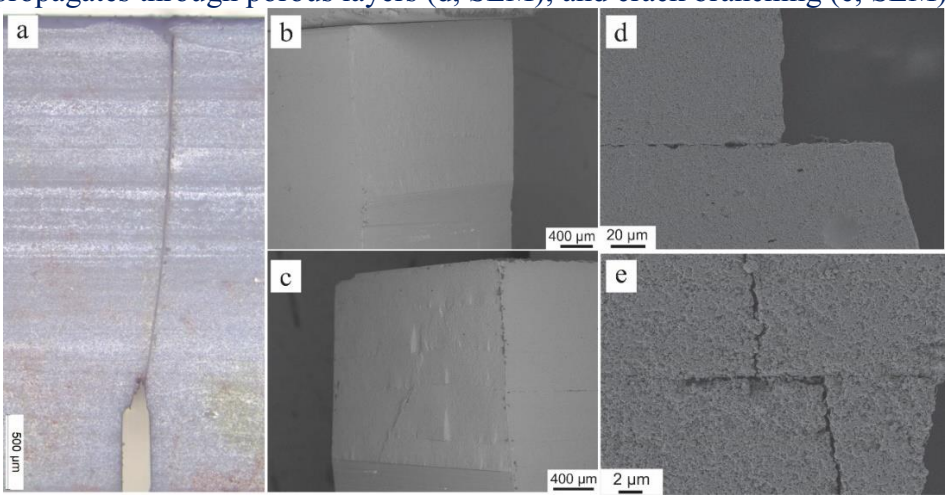

6.4. Conclusions

Alumina laminates with thick dense layers and thin porous interlayers were developed and sintered at 1350 °C. Large and small grains were observed in porous layers, with the last more concentrated around the modeled pores. The increase of the volume of pores demonstrated a tendency to reduce the average grain size. Nanoindentation results presented the expected decrease of elastic modulus and hardness in the porous layer, compared to the dense layer. However, measurement errors shall be taken into account because of tip penetration through voids. Vickers indentations done next to the interface indicated that crack propagation shall be stopped in the porous layer, and not continues in the next dense layer.

The strength of A-PS is statically the same as the monolithic reference. Small variations in load-displacement and R-curves were observed due to crack propagation through porous layers. No statistically significant differences were observed in the work of fracture and fracture toughness between A-PS and the reference. The lamination process of bigger samples, used for flexural and R-curve tests, did not maintain the modeled pores and layers' integrity as observed for the small sample (e.g. used in the nanoindentation test). However, still porous interlayers were observed between dense thick layers. Optical inspections of fractured surfaces did not reveal a macroscopic alteration of the crack path. Still, an enhanced roughness could be observed in the fractured surface due to the presence of porous layers. When analyzed in more detail, small deviations of the crack path are visible in porous layers.

Chapter 7 – Final remarks

7.1 Conclusions of the thesis

According to the results of this thesis, it can be concluded that the starting powders presented unimodal particle size distributions, with faceted irregular shapes. The identified crystalline phases were alpha, rutile, and MnO for alumina, titanium dioxide, and manganese oxide, respectively. Ceramic slurries presented pseudoplastic rheological behavior and were well deflocculated by the use of the dispersant. Pure and doped alumina defect-free tapes were successfully processed via tape casting. Thermal analyses showed complete organic removal at 525 °C. The use of dopants successfully reduced the starting sintering temperature, increased sintering rate, and enhanced sintering of alumina. After sintering, doped alumina crystalline phases were identified as alpha-alumina, rutile, and $MnTiO_3$.

Diffusion of dopants through the interface of pure and doped alumina created a visible light brownish region in pure alumina layers due to the migration of Mn and Ti from the doped Al_2O_3 layer. The thickness of this diffused region could be estimated optically and increases with increasing temperature. The presence of dopants modified the microstructure and, in general, increased the average grain size of alumina. It also increased the hardness, elastic modulus, and maximum load obtained by nanoindentation, presenting intermediate values higher than those of pure alumina layers and lower than the ones in the doped alumina layer. The increasing temperature also increased *H*, *E*, and maximum load. The interdiffusion profile of diffused zone was observed by values of *H*, *E*, and grain size.

In general, hardness and elastic modulus were directly proportional to the density/porosity of materials of this work. The mechanical strength of doped alumina sintered at 1200 °C was equivalent to the pure alumina sintered at 1350 °C. Composites with the thickness ratio of 4:1, DA-17L and AC-17L, presented no loss in strength compared to references. However, when the thickness ratio is 1:1 or higher, DA-11L and DA-3L, a decrease in strength was observed. Regarding the fracture toughness of materials, monolithic references presented nearly constant $K_{IC,}$ while laminates presented K_{IC} increasing and decreasing when crack propagated through the interfacial zones. This behavior was more pronounced with increasing weak layers' thickness. The higher the volume of weak material per sample, the lower the work of fracture of the entire sample.

The low calculated residual stresses shall be taken into account when analyzing mechanical behavior.

Modeled pores were used to produce porosity in thin porous alumina layers. Small grains were concentrated more around the modeled pores, compared to the large grains. The increase in the volume of pores showed a tendency of decreasing average grain size. The use of binder in the PS-alumina slurry improved layers' adhesion. Values of *H* and *E* of porous layers were lower than alumina dense layers, as expected. According to Vickers indentations, crack propagation may be retarded by the thin porous layers. Big samples manufactured for bending and fracture toughness tests did not maintain the modeled pores and well-formed porous layers as observed for small-scale samples. However, still porous interlayers were observed between dense alumina layers. The mechanical strength of the laminate with porous interlayers is statically the same as the monolithic reference. Small variations in load-displacement curves and R-curves were detected due to crack propagation through porous layers, although no difference in the work of fracture was observed. Although some small deviations in the crack path were noticed due to the presence of the weak interfaces, no macrodeflections occurred during fracture.

7.2 Suggestions for future works

For the continuation of this work, some suggestions are listed:

- Make an in-depth study of diffusion of dopants (Mn and Ti) in alumina, analyzing the mechanisms of diffusion, sintering temperatures, and different compositions. Also, explore the potential of producing a functionally graded material with a gradient of dopants, grain size, and mechanical properties.
- Go in the direction of processing nanolayered ceramics and study nanomechanics. Same materials or other ceramic oxides as ZrO_2 and MgO can be used. Small scales of the thickness (very thin layers) could be processed using, for example, atomic layer deposition. The focused ion beam technique can create the necessary morphology of samples to be tested in small scales. The mechanical behavior could be characterized in microscale and analyzed by using nanoindentation techniques together with SEM.
- Produce the laminates via fast firing to reduce sintering costs. This route of sintering could also be used to densify the suggested nanolayered ceramics.

References

1. Bansal NP, editor. Handbook of ceramic composites. Boston: Springer; 2006.
2. Harper C. Handbook of ceramics glasses, and diamonds. New York: McGraw-Hill Professional; 2001.
3. Reynaud P, Dalmaz A, Tallaron C, Rouby D, Fantozzi G. Apparent stiffening of ceramic-matrix composites induced by cyclic fatigue. *J Eur Ceram Soc*. 1998;18(13):1827–1833.
4. Volkmann E, Daniel Barros M, Tushtev K, *et al.* Influence of the matrix composition and the processing conditions on the grain size evolution of Nextel 610 fibers in ceramic matrix composites after heat treatment. *Adv Eng Mater*. 2015;17(5):610–614.
5. Jiménez-Melendo M, Clauss C, Domínguez-Rodríguez A, De Portu G, Roncari E, Pinasco P. High temperature plastic deformation of multilayered YTZP/ZTA composites obtained by tape casting. *Acta Mater*. 1998;46(11):3995–4004.
6. Sánchez-Herencia AJ, Gurauskis J, Baudín C. Processing of Al2O3/Y-TZP laminates from water-based cast tapes. *Compos Part B Eng*. 2006;37(6):499–508.
7. Riedel R, Chen I-W, editors. Ceramics science and technology, volume 2: properties. Weinheim: Wiley; 2011.
8. Reed JS. Principles of ceramics processing. 2nd ed. New York: Wiley; 1995.
9. Ashby MF, Jones DRH. Engineering materials 2, an introduction to microstructures, processing and design. 2nd ed. Woburn: Butterworth-Heinemann; 1998.
10. Black J, Hastings G. Handbook of biomaterial properties. 1st ed. London: Springer; 1998.
11. Acchar W, Segadães AM. Properties of sintered alumina reinforced with niobium carbide. *Int J Refract Met Hard Mater*. 2009;27(2):427–430.
12. Lehman RL. Overview of ceramic design and process engineering. *Eng Mater Handb*. 1991;4:29–37.
13. Olszyna AR, Marchlewski P, Kurzydłowski KJ. Sintering of high-density, high-purity alumina ceramics. *Ceram Int*. 1997;23(4):323–328.
14. Kothari NC. The effect of particle size on sintering kinetics in alumina powder. *J Nucl Mater*. 1965;17(1):43–53.
15. Fang ZZ, Wang H. Densification and grain growth during sintering of nanosized particles. *Int Mater Rev*. 2008;53(6):326–352.
16. Rao P, Iwasa M, Kondoh I. Properties of low-temperature-sintered high purity α-alumina ceramics. *J Mater Sci Lett*. 2000;19(7):543–545.
17. Yeh T, Sacks MD. Low-temperature sintering of aluminum oxide. *J Am Ceram Soc*. 1988;71(10):841–844.
18. Horn DS, Messing GL. Anisotropic grain growth in TiO2-doped alumina. *Mater Sci Eng A*. 1995;195(C):169–178.

19. Barry Carter C, Grant Norton M. Ceramic materials: science and engineering. New York: Springer; 2007.

20. Doremus RH. Diffusion in alumina. *J Appl Phys*. 2006;100(10).

21. Sathiyakumar M, Gnanam FD. Influence of additives on density, microstructure and mechanical properties of alumina. *J Mater Process Technol*. 2003;133(3):282–286.

22. Ohya Y, Hasegawa M, Nakagawa Z, Hamano K. Effects of some additives on microstructure and bending strength of aluminum titanate ceramics. *Int J High Technol Ceram*. 1987;3(1):88–89.

23. Moreira MC, Segadães AM. Phase equilibrium relationships in the system Al2O3-TiO2-MnO, relevant to the low-temperature sintering of alumina. *J Eur Ceram Soc*. 1996;16(10):1089–1098.

24. Xue LA, Chen I-W. Low-temperature sintering of alumina with liquid-forming additives. *J Am Ceram Soc*. 1991;74(8):2011–2013.

25. Winkler ER, Sarver JF, Cutler IB. Solid solution of titanium dioxide on aluminum oxide. *J Am Ceram Soc*. 1945;49(12):634–637.

26. Cutler IB, Bradshaw C, Christensen CJ, Hyatt EP. Sintering of alumina at temperatures of 1400ºC and below. *J Am Ceram Soc*. 1957;40(4):134–139.

27. Jones JT, Maitra PK, Cutler IB. Role of structural defects in the sintering of alumina and magnesia. *J Am Ceram Soc*. 1958;41(9):353–357.

28. Keski JR, Cutler IB. Initial sintering of MnxO-Al2O3. *J Am Ceram Soc*. 1968;51(8):440–444.

29. Bagley RD, Cutler IB, Johnson DL. Effect of TiO2 on initial sintering of Al2O3. *J Am Ceram Soc*. 1970;53(3):136–141.

30. Bennison SJ, Harmer MP. Effect of MgO solute on the kinetics of grain growth in Al2O3. *J Am Ceram Soc*. 1983;66(5):C-90-C-92.

31. Kostic E, Kiss SJ, Boskovic S. Sintering and microstructure development in the Al2O3-MnO-TiO2 system. *Powder Metall Int*. 1990;22(2):29–30.

32. Toy C, Demirci M, Onurlu S, Sadik Tasar M, Baykara T. A colloidal method for manganese oxide addition to alumina powder and investigation of properties. *J Mater Sci*. 1995;30(16):4183–4187.

33. Erkalfa H, Misirli Z, Baykara T. The effect of TiO2 and MnO2 on densification and microstructural development of alumina. *Ceram Int*. 1998;24(2):81–90.

34. Sathiyakumar M, Gnanam FD. Influence of MnO and TiO2 additives on density, microstructure and mechanical properties of Al2O3. *Ceram Int*. 2002;28:195–200.

35. Pelleg J. Diffusion in ceramics. Cham: Springer; 2016.

36. Mehrer H. Diffusion in solids. Berlin: Springer; 2007.

37. Kirkendall EO. Diffusion of zinc in alpha brass. *Trans Metall Soc AIME*. 1942;147:104–110.

38. Fielitz P, Borchardt G, Ganschow S, Bertram R. 26Al tracer diffusion in nominally undoped single crystalline α-Al2O3. *Defect Diffus Forum*. 2012;323–325:75–79.

39. Paladino AE, Kingery WD. Aluminum ion diffusion in aluminum oxide. *J Chem Phys*. 1962;37(5):957–962.

40. Fielitz P, Borchardt G, Ganschow S, Bertram R, Markwitz A. 26Al tracer diffusion in titanium doped single crystalline α-Al2O3. *Solid State Ionics*. 2008;179(11–12):373–379.

41. Snijkers F, de Wilde A, Mullens S, Luyten J. Aqueous tape casting of yttria stabilised zirconia using natural product binder. *J Eur Ceram Soc*. 2004;24(6):1107–1110.

42. Bitterlich B, Lutz C, Roosen A. Rheological characterization of water-based slurries for the tape casting process. *Ceram Int*. 2002;28(6):675–683.

43. Pontin MG, Lange FF, Sánchez-Herencia AJ, Moreno R. Effect of unfired tape porosity on surface film formation by dip coating. *J Am Ceram Soc*. 2005;88(10):2945–2948.

44. Rao MP, Rodel J, Lange FF. Residual stress induced R-curves in laminar ceramics that exhibit a threshold strength. *J Am Ceram Soc*. 2001;84:2722–2724.

45. Hotza D. Colagem de folhas cerâmicas. *Cerâmica*. 1997;43:159–166.

46. Riedel R, Chen I-W. Ceramics science and technology, volume 3: synthesis and processing. Weinheim: Wiley; 2011.

47. Hotza D, Greil P. Review: aqueous tape casting of ceramic powders. *Mater Sci Eng A*. 1995;202(1–2):206–217.

48. Nishihora RK, Rachadel PL, Quadri MGN, Hotza D. Manufacturing porous ceramic materials by tape casting—A review. *J Eur Ceram Soc*. 2018;38(4):988–1001.

49. Mistler RE, Twiname ER. Tape casting: theory and practice. Westerville: Am Ceram Soc; 2000.

50. Pugh RJ, Bergstrom L. Surface and colloid chemistry in advanced ceramics processing. Boca Raton: CRC Press; 1993.

51. Shaw DJ. Introduction to colloid and surface chemistry. 4th ed. Burlington: Butherworth-Heinemann; 1992.

52. Horri BA, Ranganathan P, Selomulya C, Wang H. A new empirical viscosity model for ceramic suspensions. *Chem Eng Sci*. 2011;66(12):2798–2806.

53. Moreno R. Reología de Suspensiones Cerámicas. Madrid: Consejo Superior de Investigaciones Científicas; 2005.

54. Ruys A. Processing, structure, and properties of alumina ceramics. *Alumina Ceram*. 2019;71–121.

55. Sánchez-Herencia AJ, Baudín C. Ceramic laminates with tailored residual stresses. *Bol la Soc Espanõla Cerámica y Vidr*. 2009;48(6):273–278.

56. Minatto FD, Milak P, De Noni a., Hotza D, Montedo ORK. Multilayered ceramic

composites – a review. *Adv Appl Ceram*. 2015;114(3):127–138.

57. Ashby MF. Book 2: material and process selection charts, CES EduPack. Cambridge: Cambridge University, 2010.

58. Weibull W. A statistical distribution function of wide applicability. *J Appl Mech*. 1951;18(3):293-297.

59. Griffith AA. The phenomena of rupture and flow in solids. *Philos Trans R Soc London Ser A, Contain Pap a Math or Phys Character*. 1921;221:163–198.

60. Irwin GR. Analysis of stresses and strains near the end of cracking traversing a plate. *J Appl Mech*. 1957;24:361–364.

61. Rao MP, Sánchez-Herencia AJ, Beltz GE, McMeeking RM, Lange FF. Laminar ceramics that exhibit a threshold strength. *Science (80-)*. 1999;286(5437):102–105.

62. Ast J, Ghidelli M, Durst K, Göken M, Sebastiani M, Korsunsky AM. A review of experimental approaches to fracture toughness evaluation at the micro-scale. *Mater Des*. 2019;173.

63. Barsoum MW. Fundamentals of ceramics. 2nd ed. London: Institute of Physics Publishing Ltd; 2003.

64. Chartier T, Merle D, Besson JL. Laminar ceramic composites. *J Eur Ceram Soc*. 1995;15(2):101–107.

65. Leguillon D, Martin E, Ševeček O, Bermejo R. Application of the coupled stress-energy criterion to predict the fracture behaviour of layered ceramics designed with internal compressive stresses. *Eur J Mech - A/Solids*. 2015;54:94–104.

66. Kerans RJ, Hay RS. Interface Design for oxidation-resistant ceramic composites. *J Am Ceram Soc*. 2002;85:2599–2632.

67. Armani CJ, Ruggles-Wrenn MB, Fair GE, Hay RS. Creep of Nextel^{tm} 610 fiber at 1100 °C in air and in steam. *Int J Appl Ceram Technol*. 2013;10(2):276–284.

68. Chawla KK. Ceramic matrix composites. 2nd ed. New York: Springer; 2003.

69. Kar KK, editor. Composite materials: processing, applications, characterizations. Berlin: Springer; 2017.

70. Chang Y, Bermejo R, Ševeček O, Messing GL. Design of alumina-zirconia composites with spatially tailored strength and toughness. *J Eur Ceram Soc*. 2015;35(2):631–640.

71. Krenkel W, editor. Ceramic matrix composites: fiber reinforced ceramics and their applications. Weinheim: Wiley; 2008.

72. Clegg WJ, Kendall K, Alford NM, Button TW, Birchall JD. A simple way to make tough ceramics. *Nature*. 1990;347(6292):455–457.

73. Clegg WJ. The fabrication and failure of laminar ceramic composites. *Acta Metall Mater*. 1992;40(11):3085–3093.

74. Karambelas G, Santhanam S, Wing ZN. Strombus gigas inspired biomimetic ceramic composites via SHELL - sequential hierarchical engineered layer

lamination. *Ceram Int*. 2013;39(2):1315–1325.

75. Wang C, Huang Y, Zan Q, Zou L, Cai S. Control of composition and structure in laminated silicon nitride/boron nitride composites. *J Am Ceram Soc*. 2002;85(10):2457–2461.

76. Kovar D, Thouless MD, Halloran JW. Crack deflection and propagation in layered silicon nitride/boron nitride ceramics. *J Am Ceram Soc*. 2005;81(4):1004–1112.

77. Ma J, Wang H, Weng L, Tan GEB. Effect of porous interlayers on crack deflection in ceramic laminates. *J Eur Ceram Soc*. 2004;24(5):825–831.

78. Bueno S, Baudín C. Design and processing of a ceramic laminate with high toughness and strong interfaces. *Compos Part A Appl Sci Manuf*. 2009;40(2):137–143.

79. Ferrari B, Bartret A, Baudín C. Sandwich materials formed by thick alumina tapes and thin-layered alumina–aluminium titanate structures shaped by EPD. *J Eur Ceram Soc*. 2009;29(6):1083–1092.

80. Bueno S, Moreno R, Baudín C. Design and processing of Al2O3–Al2TiO5 layered structures. *J Eur Ceram Soc*. 2005;25(6):847–856.

81. He M, Hutchinson JW. Kinking of a crack out of an interface. *J Appl Mech*. 1989;56(2):270–278.

82. Kendall K. Transition between cohesive and interfacial failure in a laminate. *Proc R Soc Lond A Math Phys Sci*. 1975;344(1637):287–302.

83. Blanks KS, Kristoffersson A, Carlström E, Clegg WJ. Crack deflection in ceramic laminates using porous interlayers. *J Eur Ceram Soc*. 1998;18(13):1945–1951.

84. Mammoli AA, Graham AL, Reimanis IE, Tullock DL. The effect of flaws on the propagation of cracks at bi-materials interfaces. *Acta Metall Mater*. 1995;43(3):1149–1156.

85. Lee W, Howard SJ, Clegg WJ. Growth of interface defects and its effect on crack deflection and toughening criteria. *Acta Mater*. 1996;44(10):3905–3922.

86. Davis JB, Kristoffersson A, Carlström E, Clegg WJ. Fabrication and crack deflection in ceramic laminates with porous interlayers. *J Am Ceram Soc*. 2000;83(10):2369–2374.

87. Clegg WJ. Design of ceramic laminates for structural applications. *Mater Sci Technol*. 1998;14(6):483–495.

88. Bermejo R, Torres Y, Sánchez-Herencia AJ, Baudín C, Anglada M, Llanes L. Residual stresses, strength and toughness of laminates with different layer thickness ratios. *Acta Mater*. 2006;54(18):4745–4757.

89. Grigoriev ON, Karoteev A V., Maiboroda EN, *et al.* Structure, nonlinear stress-strain state and strength of ceramic multilayered composites. *Compos Part B Eng*. 2006;37(6):530–541.

90. Lugovy M, Orlovskaya N, Slyunyayev V, Gogotsi G, Kübler J, Sánchez-Herencia AJ. Crack bifurcation features in laminar specimens with fixed total thickness. *Compos Sci Technol*. 2002;62(6):819–830.

91. Bermejo R, Torres Y, Baudín C, *et al.* Threshold strength evaluation on an Al2O3–ZrO2 multilayered system. *J Eur Ceram Soc*. 2007;27(2–3):1443–1448.

92. Bermejo R, Torres Y, Sánchez-Herencia AJ, Baudín C, Anglada M, Llanes L. Fracture behaviour of an Al2O3-ZrO2 multi-layered ceramic with residual stresses due to phase transformations. *Fatigue Fract Eng Mater Struct*. 2006;29(1):71–78.

93. Marshall DB, Ratto JJ, Lange FF. Enhanced fracture toughness in layered microcomposites of Ce-ZrO2 and Al2O3. *J Am Ceram Soc*. 1991;74(12):2979–2987.

94. Sánchez-Herencia AJ, Moya JS, Tomsia AP. Microstructural design in Alumina-Alumina/Zirconia Layered Compistes. *Scr Mater*. 1998;38(1):1–5.

95. Moon RJ, Bowman KP, Trumble KP, Rödel J. Fracture resistance curve behavior of multilayered alumina-zirconia composites produced by centrifugation. *Acta Mater*. 2001;49(6):995–1003.

96. Sglavo VM, Paternoster M, Bertoldi M. Tailored residual stresses in high reliability alumina-mullite ceramic laminates. *J Am Ceram Soc*. 2005;88(10):2826–2832.

97. Green DJ, Cai PZ, Messing GL. Residual stresses in alumina-zirconia laminates. *J Eur Ceram Soc*. 1999;19(13–14):2511–2517.

98. Sglavo VM, De Genua F, Molinari A, Casari F. Alumina/silicon carbide laminated composites by spark plasma sintering. *J Am Ceram Soc*. 2009;92(11):2693–2697.

99. Ševeček O, Bermejo R, Kotoul M. Prediction of the crack bifurcation in layered ceramics with high residual stresses. *Eng Fract Mech*. 2013;108:120–138.

100. Ševeček O, Kotoul M, Leguillon D, Martin E, Bermejo R. Modelling of edge crack formation and propagation in ceramic laminates using the stress-energy coupled criterion. *Eng Fract Mech*. 2016;167:45–55.

101. Bermejo R, Sánchez-Herencia AJ, Llanes L, Baudín C. High-temperature mechanical behaviour of flaw tolerant alumina-zirconia multilayered ceramics. *Acta Mater*. 2007;55(14):4891–4901.

102. Tarlazzi A, Roncari E, Pinasco P, Guicciardi S, Melandri C, de Portu G. Tribological behaviour of Al2O3/ZrO2-ZrO2 laminated composites. *Wear*. 2000;244(1–2):29–40.

103. Cai PZ, Green DJ, Messing GL. Mechanical characterization of Al2O3/ZrO2 hybrid laminates. *J Eur Ceram Soc*. 1998;18(14):2025–2034.

104. Hbaieb K, McMeeking RM, Lange FF. Crack bifurcation in laminar ceramics having large compressive stress. *Int J Solids Struct*. 2007;44(10):3328–3343.

105. Náhlík L, Sestáková L, Hutar P, Bermejo R. Prediction of crack propagation in layered ceramics with strong interfaces. *Eng Fract Mech*. 2010;77(11):2192–2199.

106. Swab JJ, Tice J, Wereszczak AA, Kraft RH. Fracture toughness of advanced structural ceramics: Applying ASTM C1421. *J Am Ceram Soc*. 2015;98(2):607–615.

107. Kotoul M, Sevecek O, Vyslouzil T. Crack growth in ceramic laminates with strong

interfaces and large compressive residual stresses. *Theor Appl Fract Mech*. 2012;61(1):40–50.

108. Lube T, Pascual J, Chalvet F, de Portu G. Effective fracture toughness in Al2O3-Al2O3/ZrO2 laminates. *J Eur Ceram Soc*. 2007;27(2007):1449–1453.

109. Gurauskis J, Sánchez-Herencia AJ, Baudín C. Alumina–zirconia layered ceramics fabricated by stacking water processed green ceramic tapes. *J Eur Ceram Soc*. 2007;27(2–3):1389–1394.

110. Moon RJ, Hoffman M, Hilden J, Bowman K. Weight function analysis on the R-curve behavior of multilayered alumina-zirconia composites. 2002;11:1505–1511.

111. Moon RJ, Bowman K, Trumble K, Rödel J. Comparison of r-curves from Single-Edge V-Notched-Beam (SEVNB) and Surface-Crack-in-Flexure (SCF) fracture-toughness test methods on multilayered alumina-zirconia composites. *J Am Ceram Soc*. 2000;83(2):445–447.

112. Fett T. Stress intensity factors and weight functions for special crack problems, FZKA 6025. Karlsruhe: Forschungszentrum Karlsruhe;1998.

113. Fett T, Munz D. Influence of crack-surface interactions on stress intensity factor in ceramics. *J Mater Sci Lett*. 1990;9(12):1403–1406.

114. Fett T, Munz D. Determination of fracture toughness at high temperatures after subcritical crack extension. *J Am Ceram Soc*. 1992;75(11):3133–3136.

115. Jelitto H, Hackbarth F, Özcoban H, Schneider GA. Automated control of stable crack growth for R-curve measurements in brittle materials. *Exp Mech*. 2013;53(2):163–170.

116. Jelitto H, Felten F, Häusler C, Kessler H, Balke H, Schneider GA. Measurement of energy release rates for cracks in PZT under electromechanical loads. *J Eur Ceram Soc*. 2005;25(12):2817–2820.

117. Fünfschilling S, Fett T, Oberacker R, *et al.* R curves from compliance and optical crack-length measurements. *J Am Ceram Soc*. 2010;93(9):2814–2821.

118. Özcoban H, Jelitto H, Schneider GA. Influence of finite notch root radius and optically determined crack length on the measured fracture toughness of brittle materials. *J Eur Ceram Soc*. 2010;30(7):1579–1583.

119. Fett T, Fünfschilling S, Hoffmann MJ, Oberacker R, Jelitto H, Schneider GA. R-curve determination for the initial stage of crack extension in Si3N4. *J Am Ceram Soc*. 2008;91(11):3638–3642.

120. Özcoban H, Fett T, Schneider GA. Computer-controlled stable crack growth as a reliable and fast method to determine subcritical crack growth. *J Test Eval*. 2012;40(2):238–242.

121. Sōmiya S, editor. Handbook of advanced ceramics: materials, applications, processing, and properties. London: Academic Press; 2013.

122. Jabbari M, Bulatova R, Tok AIY, Bahl CRH, Mitsoulis E, Hattel JH. Ceramic tape casting: A review of current methods and trends with emphasis on rheological behaviour and flow analysis. *Mater Sci Eng B Solid-State Mater Adv Technol*. 2016;212:39–61.

123. Hotza D, Nishihora RK, Machado RAF, Geffroy P, Chartier T, Bernard S. Tape casting of preceramic polymers toward advanced ceramics: A review. *Int J Ceram Eng Sci*. 2019;1(1):21–41.

124. Chartier T, Rouxel T. Tape-cast alumina-zirconia laminates: processing and mechanical properties. *J Eur Ceram Soc*. 1997;17(2–3):299–308.

125. Greenwood R, Roncari E, Galassi C. Preparation of concentrated aqueous alumina suspensions for tape casting. *J Eur Ceram Soc*. 1997;17(12):1393–1401.

126. Albano MP, Genova LA, Garrido LB, Plucknett K. Processing of porous yttria-stabilized zirconia by tape-casting. *Ceram Int*. 2008;34(8):1983–1988.

127. Moreno V, Hotza D, Greil P, Travitzky N. Dense YSZ Laminates Obtained by Aqueous Tape Casting and Calendering. *Adv Eng Mater*. 2013;15(10):1014-1018.

128. Rahaman MN. Ceramic processing and sintering. 2nd ed. Boca Raton: CRC Press; 2003.

129. Chartier T, Bruneau A. Aqueous tape casting of alumina substrates. *J Eur Ceram Soc*. 1993;12(4):243–247.

130. Gutiérrez CA, Moreno R. Influence of slip preparation and casting conditions on aqueous tape casting of Al2O3. *Mater Res Bull*. 2001;36(11):2059–2072.

131. Pagnoux C, Chartier T, de F. Granja M, Doreau F, Ferreira JM, Baumard JF. Aqueous suspensions for tape-casting based on acrylic binders. *J Eur Ceram Soc*. 1998;18(3):241–247.

132. Erkalfa H, Misirli Z, Baykara T. Densification of alumina at 1250 °C with MnO2 and TiO2 additives. *Ceram Int*. 1995;21(5):345–348.

133. Daniel Barros M, Rachadel PL, Fredel MC, Janßen R, Hotza D. Mechanical behaviour of zirconia-toughened alumina laminates with or without Y-PSZ intermediate layers. *J Ceram Sci Technol*. 2018;09(1):69–78.

134. Kosmulski M. Surface charging and points of zero charge. 1st ed. Boca Raton: CRC Press; 2009.

135. Gutiérrez CA, Moreno R. Preventing ageing on Al2O3 casting slips dispersed with polyelectrolytes. *J Mater Sci*. 2000;35:5867–5872.

136. Singh BP, Menchavez R, Takai C, Fuji M, Takahashi M. Stability of dispersions of colloidal alumina particles in aqueous suspensions. *J Colloid Interface Sci*. 2005;291(1):181–186.

137. Albano MP, Garrido LB, Plucknett K, Genova LA. Influence of starch content and sintering temperature on the microstructure of porous yttria-stabilized zirconia tapes. *J Mater Sci*. 2009;44(10):2581–2589.

138. Kang YB, Lee HG. Experimental study of phase equilibria in the MnO-"TiO2"-"Ti2O3" system. *ISIJ Int*. 2005;45(11):1543–1551.

139. McKee Jr. WD, Aleshin E. Aluminum oxide-titanium oxide solid solution. *J Am Ceram Soc*. 1963;46(1):54–58.

140. Heuer AH. Oxygen and aluminum diffusion in α-Al2O3: How much do we really

understand? *J Eur Ceram Soc*. 2008;28:1495–1507.

141. Lagerlöf KPD, Mitchell TE, Heuer AH. Lattice diffusion kinetics in undoped and impurity-doped sapphire (α-Al2O3): a dislocation loop annealing study. *J Am Ceram Soc*. 1989;72(11):2159–2171.

142. Bor B, Giuntini D, Domènech B, Swain M V., Schneider GA. Nanoindentation-based study of the mechanical behavior of bulk supercrystalline ceramic-organic nanocomposites. *J Eur Ceram Soc*. 2019;39(10):3247–3256.

143. Chlup Z, Hadraba H, Slabáková L, Drdlík D, Dlouhý I. Fracture behaviour of alumina and zirconia thin layered laminate. *J Eur Ceram Soc*. 2012;32(9):2057–2061.

144. Bermejo R, Danzer R. High failure resistance layered ceramics using crack bifurcation and interface delamination as reinforcement mechanisms. *Eng Fract Mech*. 2010;77(11):2126–2135.

145. de Portu G, Micele L, Pezzotti G. Laminated ceramic structures from oxide systems. *Compos Part B Eng*. 2006;37:556–567.

146. Blaese D, Benitez T, Daniel Barros M, *et al.* R-curve behavior and flexural strength of zirconia-toughened alumina and partially stabilized zirconia composite laminates. *Ceram Int*. 2018;44(12):13463–13468.

147. Kübler J, Blugan G, Jelitto H, Schneider GA, Dobedoe R. Structural micro-layered ceramics with surfaces under tension and compression with increasing apparent fracture toughness. *Key Eng Mater*. 2007;336–338:2564–2568.

148. Pontin MG, Lange FF. Effects of porosity on the threshold strength of laminar ceramics. *J Am Ceram Soc*. 2005;88(2):376–382.

149. Sørensen BF, Horsewell A. Crack growth along interfaces in porous ceramic layers. *J Am Ceram Soc*. 2004;84(9):2051–2059.

150. Sglavo VM, Bellettati N. Ceramic laminates with improved mechanical reliability by tailoring the porosity of the constituting layers. *J Eur Ceram Soc*. 2017;37(4):1643–1650.

151. Bueno S, Baudín C. Layered materials with high strength and flaw tolerance based on alumina and aluminium titanate. *J Eur Ceram Soc*. 2007;27(2–3):1455–1462.

152. Casellas D, Ràfols I, Llanes L, Anglada M. Fracture toughness of zirconia-alumina composites. *Int J Refract Met Hard Mater*. 1999;17(1):11–20.

153. Oliver WC, Pharr GM. Measurement of hardness and elastic modulus by instrumented indentation: Advances in understanding and refinements to methodology. *J Mater Res*. 2004;19(01):3–20.

154. Jelitto H, Felten F, Swain M V., Balke H, Schneider GA. Measurement of the total energy release rate for cracks in PZT under combined mechanical and electrical loading. *J Appl Mech Trans ASME*. 2007;74(6):1197–1211.

155. Fett T, Diegele E. Indirect measurements of compliance in four-point-bending tests. *J Test Eval*. 1988;16(5):487–488.

156. Munz D, Fett T. Ceramics: mechanical properties, failure behaviour, materials

selection. *Springer Sci Bus Media*. 1999;36.

157. Wachtman JB, Cannon WR, Matthewson MJ. Mechanical properties of ceramics. New York: Wiley; 2009.

158. Seidel J, Claussen N, Rödel J. Reliability of alumina ceramics: effect of grain size. *J Eur Ceram Soc*. 1995;15(5):395–404.

159. Neumann M, Gehre P, Kübler J, *et al.* Stable crack propagation in free standing thermal sprayed Al2O3 and Al2O3-ZrO2-TiO2 coatings. *Ceram Int*. 2019;45(7):8761–8766.

160. Tomaszewski H, Boniecki M, Weglarz H. Effect of grain size on R-curve behaviour of alumina ceramics. *J Eur Ceram Soc*. 2000;20(14–15):2569–2574.

161. Mussler B, Swain M V., Claussen N. Dependence of fracture toughness of alumina on grain size and test technique. *J Am Ceram Soc*. 1982;65(11):566–572.

162. Chantikul P, Bennison SJ, Lawn BR. Role of grain size in the strength and R-curve properties of alumina. *J Am Ceram Soc*. 1990;73(8):2419–2427.

163. He M, Hutchinson JW. Crack deflection at an interface between dissimilar elastic materials. *Int J Solids Struct*. 1989;25(9):1053–1067.

164. Sarikaya A, Dogan F. Effect of various pore formers on the microstructural development of tape-cast porous ceramics. *Ceram Int*. 2013;39(1):403–413.

165. Leguillon D, Tariolle S, Martin E, Chartier T, Besson JL. Prediction of crack deflection in porous/dense ceramic laminates. *J Eur Ceram Soc*. 2006;26(3):343–349.

166. Daniel Barros M, Jelitto H, Hotza D, Janßen R. Microstructure and mechanical behavior of TiO2-MnO doped-alumina/alumina laminates. *J Am Ceram Soc*. 2021;104(02):1047–1057.

167. Livanov K, Jelitto H, Bar-On B, Schulte K, Schneider GA, Wagner DH. Tough alumina/polymer layered composites with high ceramic content. *J Am Ceram Soc*. 2015;98(4):1285–1291.

168. Pasquarelli RM, do Rosário JJ, Rath L, Schneider GA, Janßen R. High temperature behavior of monodisperse porosity in alumina films. *J Eur Ceram Soc*. 2015;35(14):3917–3926.